Dissertation

submitted to the

Combined Faculties of the Natural Sciences and Mathematics

of the Ruperto-Carola-University of Heidelberg, Germany

for the degree of

Doctor of Natural Sciences

Put forward by

Dipl.-Phys. Annina Luck

born in: Langenfeld

Oral examination: 16. November 2016

Nuclear spin dominated relaxation of atomic tunneling systems in glasses

Referees: Prof. Dr. Christian Enss
Prof. Dr. Heinz Horner

Kernspindominierte Relaxation atomarer Tunnelsysteme in Gläsern

Die im Rahmen dieser Arbeit durchgeführten Messungen haben einen nicht phononischen Relaxationskanal in Gläsern bei sehr tiefen Temperaturen offenbart, der durch elektrische Kernquadrupolmomente hervorgerufen wird. Dielektrische Messungen der Multikomponentengläser N-KZFS11 und HY-1, welche die Isotope ^{181}Ta beziehungsweise ^{165}Ho mit sehr großen elektrischen Kernquadrupolmomenten enthalten, zeigen eine zusätzliche Relaxationsrate im Kilohertzbereich in diesen Gläsern. Diese ist für Temperaturen oberhalb der Kernquadrupolaufspaltung der relevanten Isotope konstant. Die Ergebnisse werden mit Messungen an Herasil und N-BK7 verglichen, welche keine großen Kernquadrupolmomente enthalten. Mittels dreier Messaufbauten zur Messung der komplexen dielektrischen Funktion wurden Messungen über annähernd acht Größenordnungen in der Frequenz zwischen 60 Hz und 1 GHz bis hinunter zu Temperaturen von 7,5 mK durchgeführt. Die Messungen erlauben eine detaillierte Untersuchung der in dieser Arbeit entdeckten Effekte und haben zur Entwicklung eines neuen vereinfachten Modells der Auswirkung von Kernquadrupolmomenten auf das Tieftemperaturverhalten von Gläsern geführt. Die Daten werden mit auf diesem Modell basierenden numerischen Berechnungen verglichen.

Nuclear spin dominated relaxation of atomic tunneling systems in glasses

The measurements performed in this thesis have revealed a non phononic relaxation channel for atomic tunneling systems in glasses at very low temperatures due to the presence of nuclear electric quadrupoles. Dielectric measurements on the multicomponent glasses N-KZFS11 and HY-1, containing ^{181}Ta and ^{165}Ho, respectively, that both carry very large nuclear electric quadrupole moments, show a relaxation rate in the kilohertz range, that is constant for temperatures exceeding the nuclear quadrupole splitting of the relevant isotopes. The results are compared to measurements performed on the glasses Herasil and N-BK7 that both contain no large nuclear quadrupole moments. Using three different setups to measure the complex dielectric function, the measurements cover almost eight orders of magnitude in frequency from 60 Hz to 1 GHz and temperatures down to 7.5 mK. This has allowed us a detailed study of the novel effects observed within this thesis and has led to a simplified model explaining the effects of nuclear electric quadrupoles on the behavior of glasses at low temperatures. Numeric calculations based on this model are compared to the measured data.

Contents

1. Introduction

Früher waren Gläser einfacher.
Siegfried Hunklinger

One of the great joys of being an experimental physicist lies in the finding of new and unexpected rules governing the behavior of our environment. It is then an equal joy to find the exception to the rule and thereby come to a new understanding of the underlying principles, maybe not only cause of the exception, but also of other, previously not understood, findings.

One example for such an unexpected rule is the low temperature behavior of glasses. Measurements of the thermal properties of very different glassy materials showed a striking similarity [Zel71], that was later also found in other observables. The behavior is not only very similar in different glassy materials, but also differs strongly from the low temperature behavior of crystalline materials.
The reason for this lies in the fundamental difference found in the long range order – or lack thereof – of the atoms in the material's structure in the crystalline and amorphous state of matter. While crystals posses a well-ordered lattice that leads to a long range order, amorphous materials like silicate based glasses or many polymers, show only short range order. Small variation in the lattice constants of these materials, the length and orientation of the bonds between atoms, lead to a loss of long range order.
Many materials can enter this metastable state, when a liquid melt is cooled rapidly below the so called *glass transition temperature* T_g, which prevents an ordered lattice from forming. The most prominent group of amorphous materials is that of multicomponent glasses based on silicate and borate oxides, that can contain a large variety of other oxides, allowing for a wide spread in the materials' properties like density, refraction index, color or even electric conductivity.

The disorder in amorphous solids allows for the existence of localized low energy excitations that become apparent at low temperatures. As other excitations, such as phonons, die out towards lowest temperatures, the localized low energy excitations dominate the properties of glasses. A phenomenological description, that models the excitations as tunneling particles in two-level systems with a wide distribution of parameters, was given by Anderson et al. [And72] and Phillips [Phi72] in the so called *Standard Tunneling Model*. It considers only the disorder present in any amor-

phous material and thus leads to the prediction of a *universal behavior of glasses* at low temperatures, that has been a cornerstone of low temperature glass physics ever since.
In its simplicity, the standard tunneling model is able to describe many properties of glasses like the specific heat [Ste76, Zel71, Las75], thermal conductivity [Cah88, Zel71] or the dielectric function [Fro77, vR98, Luc11, Ens89, Rog97b, Str98, Woh01a] and elastic susceptibility [Rau95, Cla94, Cla00] at low temperatures. Measurements conducted on a large variety of different materials have, over the years, confirmed the universal behavior and generally show a very good agreement with the model. Deviations have also been observed, especially in low frequency dielectric and elastic measurements, but are again of a universal nature. They have been attributed to a restricted distribution of two-level systems [Ens89, Bec90, Dou80] and to their interaction at lowest temperatures [Bur95, Ens97].
We give an introduction to the structural properties of glasses, their low temperature behavior and the standard tunneling model in chapter two of this thesis, along with the most prominent extensions of the model. Numeric simulations performed within this thesis help discussing the effects caused by these modified versions of the standard tunneling model in more detail.

Probably the most puzzling effect not predicted by the standard tunneling model but measured in dielectric glasses is the sensitivity of many multicomponent glasses to small magnetic fields. It can be observed both in measurements of the dielectric function [Str98, Str00, Woh01b, Hau02, Pol09] and two pulse polarization echoes [Lud02, Lud03]. After several different possible explanations were discussed [Ket99, Str00, Wür02], isotope specific echo experiments on glycerol revealed nuclear electric quadrupoles to be the cause of the magnetic field dependence [Nag04, Bar13]. Subsequently, detailed models predicting effects of nuclear electric quadrupoles on both echoes [Wür02, Baz08, Bar13] and the dielectric susceptibility [Bur06a, Bur06b, Bur06c] were developed.
In chapter three of this thesis, we give a brief overview over the measurements leading to the discovery of the influence of nuclear electric quadrupoles on dielectric glasses at low temperatures. This is followed by an introduction to nuclear quadrupole resonance and by a more detailed look at the predictions made for the dielectric function.

Despite the success of the quadrupole model in explaining the dielectric echo experiments, a conclusive understanding for the low frequency dielectric susceptibility is still missing. Within this thesis, we aim to examine the influence of very large nuclear electric quadrupoles on the dielectric function of glasses at low temperatures. A possible influence of the nuclear moments should then be most pronounced and

be more prominent in the measured data as compared to glasses that contain no or only small nuclear quadrupole moments.
The possible temperature and frequency range of dielectric measurements most affected by the effects due to nuclear electric quadrupoles is very broad. We have therefore used three different measurement setups in ^{3}He/^{4}He dilution refrigerators, allowing for measurements down to 7.5 mK and between 60 Hz and 1 GHz. All three setups can measure both the real part and the loss tangent of the complex dielectric function, leading to a data set that allows a very detailed study of the low temperature dielectric properties of the measured glasses.
The measurement setups are described in chapter four, along with overview over the four different samples examined within this thesis. We have chosen the quartz glass Herasil and the multicomponent glass N-BK7, that have previously been measured in many experiments, as a comparison to the the glasses N-KZFS11 and HY-1, that have not previously been studied systematically at low temperatures. While the first two glasses contain no large nuclear electric quadrupoles, we find about one percent of ^{181}Ta in N-KZFS1 and similar amounts of ^{165}Ho in HY-1. The latter isotope not only possesses a large nuclear quadrupole moment, but also a magnetic moment due to its electronic properties.

The results obtained in the measurements of the four samples are presented in chapter five. Here, the focus lies on the low temperature dielectric properties of N-KZFS11 and HY-1 in the low frequency domain. The results are compared to the measurements of the other two glasses and to numeric simulations of the standard tunneling model including appropriate modifications. Additionally, we compare the low frequency dielectric measurements of HY-1 to elastic measurements performed on the sample in the same frequency range.
As previous studies have also concluded, the measurements of Herasil and N-BK7 can be well described qualitatively by the standard tunneling model when including slight variations in the distribution function of the tunneling parameters. The data of N-KZFS11 and HY-1, however, shows a strongly increased specific heat and a formerly unknown relaxation process due to the presence of large nuclear quadrupoles. This relaxation rate dominates both the dielectric and elastic behavior of the two glasses at low frequencies and low temperatures.
As we will show, this novel relaxation is fundamentally different from the relaxation via thermal phonons. The latter process has been believed to be the only possible relaxation channel for tunneling two-level systems in dielectric glasses. We develop a simple model for the new nuclear quadrupole related relaxation channel and show that the qualitative understanding of the data can thereby be greatly improved. From this picture we can also draw the conclusion that the magnetic field dependence of the dielectric properties of glasses, which do not prominently show the influence of

nuclear quadrupoles in their temperature dependence, is also caused by the nuclear quadrupole relaxation.

Finally, in section 5.8 of this thesis, we show that the nuclear quadrupole enabled relaxation depends sensitively on the driving field, an observation that is not yet fully understood and will certainly prompt further investigations.

2. Theoretical Background

This chapter will give an overview over the relevant theoretical background for the measurements performed in the course of this thesis. After an introduction to the structural properties of glasses, a description of the standard tunneling model, that has been developed to describe low temperature properties of glasses will be given. The main focus will be on prediction of the dielectric properties, as these are the focus of this thesis.
Over the years, a broad range of additions and modification of the standard tunneling model have been proposed. A brief overview over different of these attempts is given, with a more detailed discussion of effects caused by nuclear quadrupole moments.

2.1 Structural properties of glasses

First attempts to describe glasses as extended disordered networks of oxides were made by Zachariasen in [Zac32]. In this work it is stated, that in glass networks, various oxygen polyhedra, connected at their corners, should be formed. In the case of SiO_2, the network is built up of tetrahedra with the Si^{2+}cation in the center and four oxygen anions at the corners. A schematic drawing of a two dimensional cut through SiO_2 both in its crystalline and amorphous modification is show in figure 2.1.

One oxygen atom of each tetrahedron lies above or below the plain of the sketch. Similar tetrahedra as in the crystal are present in the amorphous modification, but they are deformed in the disordered network and their relative orientation can vary within rather large limits. While there are only rings of six silicon atoms in the crystal, the ring size varies in the amorphous solid. Sizes between the values of four and eight are most common in vitreous SiO_2 [Koh05].
According to the theory of Zachariasen, order for a stable three dimensional network to form, the glass forming oxides AO_n must fulfill several requirements: Each oxygen atom can only be linked to at most two atoms A, the polyhedra that are formed may not contain too oxygen atoms and they must be connected only at their corners. This leads, for example, to the conclusion, that oxides of the composition AO_2 and A_2O_5, being able to form tetrahedra and octahedra, should generally be good glass formers.

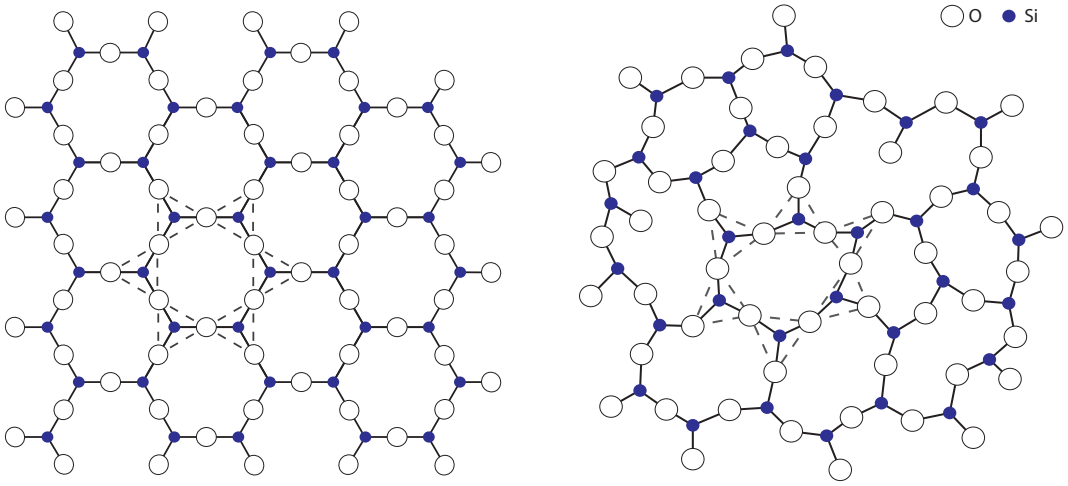

Figure 2.1: Schematic two dimensional drawings of SiO_2in its crystalline (left) and amorphous (right) modification. The dashed triangles indicate an exemplary ring of six SiO_4 tetrahedra. Scheme derived from [Zac32]

Since not every oxide of appropriate stoichiometry is indeed a good glass former, it is necessary to take other properties into account. An extension of the network theory, as formulated by Dietzel and described in [Vog92], considers the radius of the cations r_A and the field strength F at the place of the oxygen atoms surrounding the cation. With a being the distance A−O given in pm (which can be estimated as $a \approx r_A + r_O$, with r_O the radius of the O^{2-} anion) given in Å and Z the valence of the cation in units of the elementary charge, we find

$$F = \frac{Z}{a^2} \, . \tag{2.1}$$

The value of a can vary slightly with the coordination number CN, that is, the number of oxygen ions surrounding the cation, but remains stable enough to be able to draw conclusions, even if the coordination number varies or is unknown. Table 2.1 gives an overview over both cations commonly present in glasses and additional cations of relevance to this thesis. The cations fall into three groups:
The *Glass* or *Network formers* with a large field strength $F > 1.3$ are able to form stable networks by themselves. The rings of polyhedra that they form are generally small, making the resulting glasses rather hard and the temperature of the glass transition T_g high.
In contrast to this, *Network modifiers* are comparably large ions with low field strengths $F \approx 0.1 - 0.4$. They themselves do not form networks, but are built into the rings of the networks of glass formers where they can effectively behave like almost free ions, as shown schematically in figure 2.2.
Through their large size, they hinder stable A−O bonds from forming, creating larger rings of SiO_2 tetrahedra and dangling bonds of non bridging oxygen atoms [Ovi98].

Element	Valence of ion Z	Ionic radius r [pm]	Coord. number CN	Ionic distance in oxides a [pm]	Field strength at O^{2-} ion Z/a^2	
K	1	133	8	277	0.13	
Na	1	98	6	230	0.19	Network
Ba	2	143	8	286	0.24	modifiers
Pb	2	132	8	274	0.27	Z/a^2
Ca	2	106	8	248	0.33	$\approx 0.1 - 0.4$
Fe	2	83	6	215	0.43	
Mg	2	78	4	210	0.45	
Ho	3	89	6	231	0.56	
Zr	4	87	8	228	0.77	Intermediate
Fe	3	67	6	199	0.76	oxides
			4	188	0.85	Z/a^2
Al	3	57	6	189	0.84	$\approx 0.5 - 1.0$
			4	177	0.96	
Ti	4	64	6	196	1.04	
Ta	5	64	6	206	1.18	
B	3	20	4	150	1.34	Glass formers
Si	4	39	4	160	1.57	Z/a^2
P	5	34	4	155	2.08	> 1.3

Table 2.1: List of Cations commonly used in glasses and their field strengths according to Dietzel. Data taken from [Vog92, Che78, Sha76]

The most common examples for network modifiers are alkaline metals like Na, as shown in the schematic drawing, and K. Their addition to network formers softens the resulting glasses, lowers T_g and through their rather large mobility raises the electrical conductivity of the glass.

The third group of cations is that of the *Intermediate oxides*. Depending on the composition of the glass, they can both break up bonds or strengthen the network. They can not, however, form a glass on their own. A well known example is Al^{3+}, that is present in a large range of multicomponent glasses where the aluminum ions form O−Al−O bridges in the network.

The three classes of cations give a good indication, as to whether a glass will form from their oxides. The reality of glass formation is, however, far more complex. Most compositions of oxides only become vitreous when the mixing ratio is within certain limits. As properties of both holmium and tantalum containing glasses have been

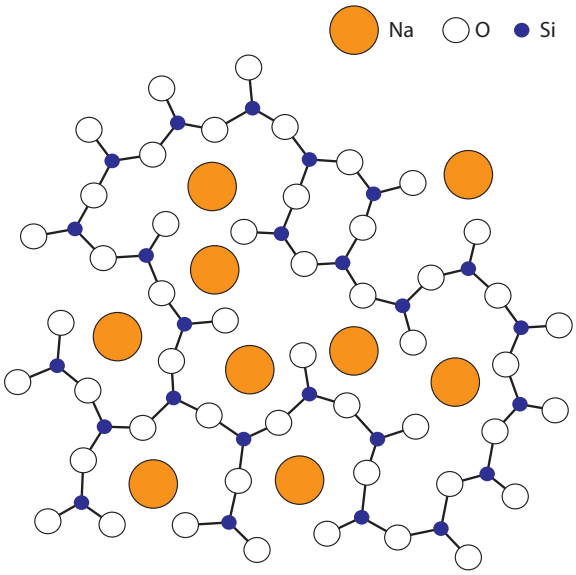

Figure 2.2: Schematic two dimensional drawing of a typical multicomponent glass. The large Na^+ions have broken up the SiO_2 network, thus softening the glass. Scheme derived from [Vog92]

investigated in this thesis, we can take a closer look at their roles in glass forming: The Ta^{5+} ion is rather large but also has a high valence, placing it right at the edge between glass formers and intermediate oxides. While first attempts to examine the role of Ta_2O_5 in multicomponent glasses were performed in [Sun40], it was only shown much later in [Ver94] and [Con06] how the oxide acts within glasses. The ions form a negatively charged $[TaO_6]^-$ octahedron that greatly strengthens the connectivity of the network. The structure needs, however a positively charged ion like K^+ or Na^+ to counteract its charge and then allows for a rather large band of glass forming mixtures.

The role of rare earth ions in glasses has been studied less extensively, and then mostly in borate glasses [Pis05, Cul99] or phosphate glasses [Eli12, Mar03]. According to the studies, its large ionic radius and intermediate valence make Ho_2O_3 a rather weak intermediate oxide. The measurements of [Cul99] place it in the role of a network modifier. This assumption is supported by the fact that the glass HY-1, whose dielectric properties have been measured in this thesis, is commonly used to calibrate lasers due to its sharp and stable absorption lines. The absorption spectrum moves only slightly due to the glass matrix when compared to that of Ho_2O_3 in solution [Wei85, All07]. As different cations of an element that is strongly bound in the glass matrix would experience a great variety of chemical bonding lengths and angles in their environment, its energy levels would shift and broaden, which is not observed in the case of holmium. This indicates that the holmium ions are most probably not bound within the matrix but rather in the intermediate spaces.

2.2 Low temperature properties of glasses

The main focus of this thesis is on the dielectric properties of glasses at low temperatures. We will therefore give a short introduction to low temperature thermal properties of glasses and set them in comparison to those of crystalline solids, before turning to the standard tunneling model, developed to explain the discrepancies described below.

The specific heat of crystalline dielectrics at low temperatures is very successfully described by the Debye model [Deb12], assuming a linear dispersion relation of phonons in isotropic materials. Due to their density of states

$$D(\omega)_{\text{phon}}\mathrm{d}\omega = \frac{V\omega^2}{2\pi^2 v_s^3}\mathrm{d}\omega \tag{2.2}$$

that depends quadratically on the frequency ω of the phonons. Here, v_s is the velocity of sound and V the volume of a given sample. The resulting heat capacity derived from integrating the internal energy U over the density of states

$$C_{\text{phon}} = \frac{\partial U}{\partial T} = \frac{\partial}{\partial T}\int_0^{\hbar\omega_{\text{D}}} \hbar\omega D(\omega) f(\omega, T)\,\mathrm{d}\hbar\omega \propto T^3 \tag{2.3}$$

is cubic in temperature at low temperatures. Since the phonon wavelength becomes large at low temperatures, local structural differences in glasses should not influence the specific heat.

This is not the case, however, as is shown in figure 2.3. In the left part of the figure, we see a comparison between crystalline and amorphous SiO_2. While the crystalline material follows the T^3 dependence very well even at lowest temperatures, the amorphous SiO_2 shows an almost linear temperature dependence below one kelvin. This behavior is due to the disordered structure, as can be seen in the right part of the figure where the heat capacity of several very different amorphous materials is plotted. Their heat capacity below 1 K not only shows a linear temperature dependence, but is also within about one order of magnitude. This indicates an almost constant rather than quadratic density of low energy states $D(\omega)$ in all of these materials, that must originate from their local disorder rather than from phonons.

The thermal conductivity of dielectric materials is also governed by phonons and can be, assuming a free phonon gas, expressed as

$$\kappa = \frac{1}{3} C v_s l\ , \tag{2.4}$$

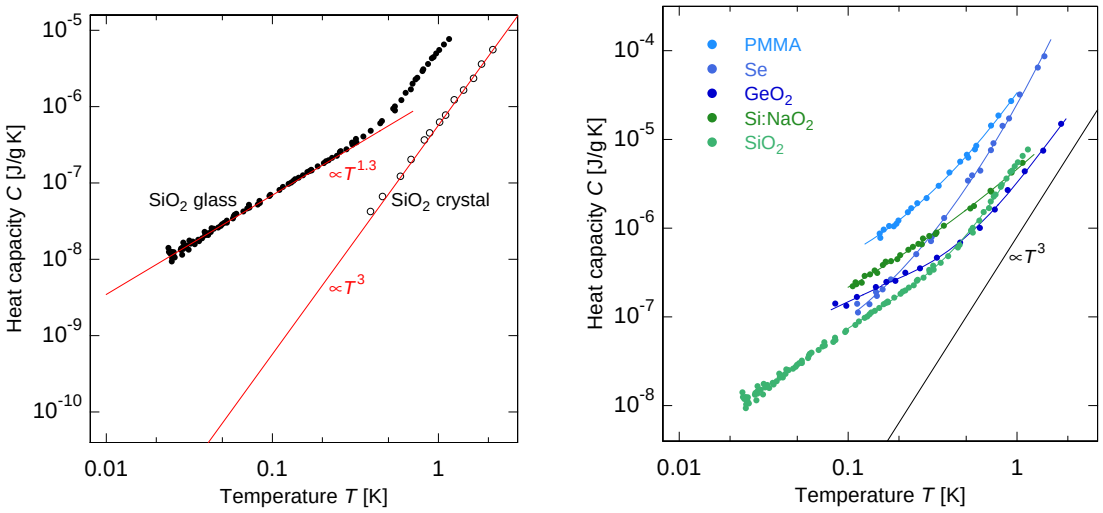

Figure 2.3: Heat capacity of amorphous and crystalline SiO_2 (left) and different amorphous solids (right) at low temperatures. Below one Kelvin, the amorphous solids show a linear temperature dependence, with the absolute values lying within one order of magnitude. The heat capacity of the crystalline SiO_2depends on T^3 noticeably smaller. [Ste76, Zel71, Las75]

where l is the phonon mean free path.
The left part of figure 2.4 shows a comparison between the thermal conductivity of crystalline and amorphous SiO_2 at low temperatures. The crystalline material has a large thermal conductivity with a T^3 dependence below a few kelvin, showing that the mean free path of phonons is long and constant in this temperature region. It is only limited by the sample dimensions and the few lattice defects of the crystal.

While the specific heat of the amorphous SiO_2 is larger that that of the corresponding crystal, the thermal conductivity is smaller by about two orders of magnitude. This indicates a much smaller and, as the temperature dependence is T^2, non constant mean free path of the phonons. Again, the effect must be due to low energy excitations caused by the local disorder, since different amorphous solids show very similar thermal conductivities as is shown in the right part of figure 2.4. The absolute values of the samples thermal conductivities below one kelvin are within one order of magnitude, which shows that the density of the additional excitations must be similar in all the materials.
As the thermal, and indeed many other, properties of amorphous solids are strikingly similar, one often speaks of the *universality of glasses* at low temperatures.
The findings described here led to the development of the standard tunneling model by both Anderson et al. [And72] and Phillips [Phi72]. It offers a simple, phenomenological approach to the description of low temperature properties of amorphous solids and will be introduced in the next sections.

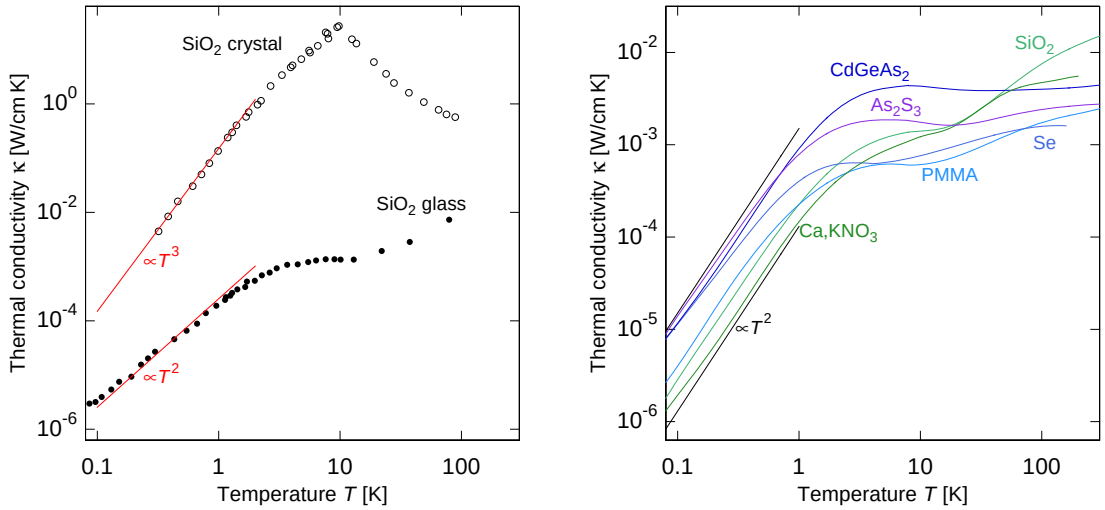

Figure 2.4: Thermal conductivity of amorphous and crystalline SiO_2 (left) and of different amorphous solids (right) at low temperatures. The thermal conductivities of the amorphous solids below one kelvin lie within one order of magnitude and show a T^2 rather than a T^3 dependence like the crystalline SiO_2[Cah88, Zel71].

2.3 The Standard Tunneling Model

Due to the disorder in amorphous solids, atoms or groups of atoms can take up different, energetically almost equivalent, positions. A schematic drawing of several possible realizations of such position changes in amorphous SiO_2 is shown in figure 2.5. The movements can be both rotational or translational in nature and can be modeled by double well potentials

The standard tunneling model is valid at temperatures, where thermally activated processes causing transitions between the two states are no longer important, but where the particles tunnel quantum mechanically through the barriers separating the states. At such low temperatures, we can generally assume that only the lowest energy level in both energy wells will contribute, as excited levels will be energetically too far removed.

Considering the fact, that the binding energies in amorphous solids are, although distributed due to the variations in the disordered structure, of the same order of magnitude as in their crystalline counterparts, we can assume the zero point energy of the two wells $\hbar\Omega/2$, defined by the binding energy of the tunneling particle to its surroundings, to be of the order of half the Debye temperature. For structural glasses, that are treated in this thesis, this would lead to an energy corresponding to about 150 K to 250 K [And59, Zel71]. The assumption of a two-level system at temperatures below 10 K is thus a good approximation.

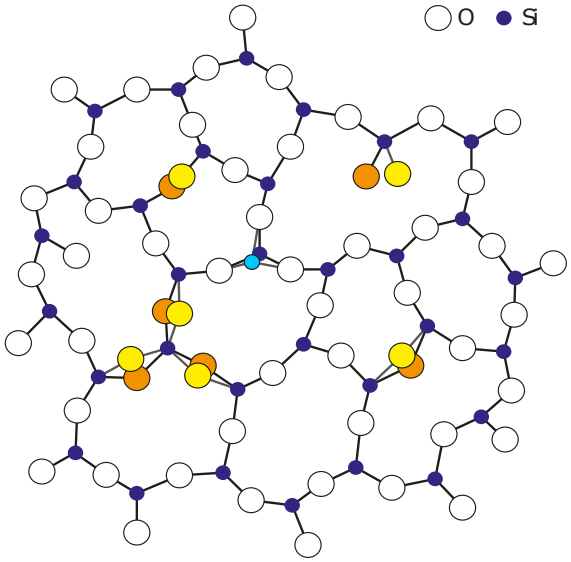

Figure 2.5: Schematic drawing of amorphous SiO_2 at low temperatures. Several possible tunneling systems are indicated with their two possible positions indicated in orange and yellow (oxygen) or dark and light blue (silicon) respectively.

2.3.1 Two-level systems

The standard tunneling model assumes the two almost degenerate states described above to be double well potentials consisting of two identical harmonic potentials that are separated by a distance d in configuration space and possessing a variable asymmetry energy Δ

$$V(x) = \begin{Bmatrix} \xi(x + d/2)^2 + \Delta/2 & \text{for } x < -\Delta/2\xi d \\ \xi(x - d/2)^2 - \Delta/2 & \text{otherwise} \end{Bmatrix} + O(x^4) \tag{2.5}$$

with ξ the steepness of the potential wells. A small correction of order $O(x^4)$ or higher creates a double well out of the two harmonic potentials of the single well. The soft potential model, briefly introduced in 2.4.5, makes use of such higher order corrections to the potential, that become important towards higher temperatures above 10 K. At lower temperatures, the soft potential model is identical to the standard tunneling model, the quadratic contribution will therefore be neglected for all calculations within the framework of the standard tunneling model that is valid at lowest temperatures.

A schematic picture of a double well potential as used in the standard tunneling model is shown in figure 2.6. The particle of effective mass m and dipole moment p can tunnel between the wells, even if its energy is not sufficient to overcome the energetic barrier of height V between the two wells, thus coupling the wave functions of the harmonic potentials.
Within the framework of the standard tunneling model, the concept of two-level (tunneling) systems is purely phenomenological. Thus, the double well in configura-

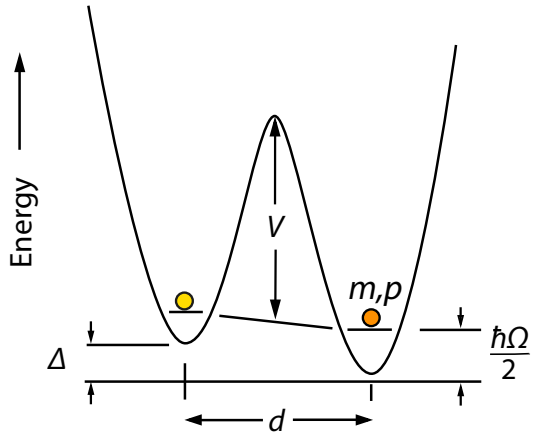

Figure 2.6: Schematic picture of a double well potential with asymmetry energy Δ and separation d of the harmonic potentials containing a particle of mass m and potentially a dipole moment p.

tion space can be connected via a translational movement, a well defined rotation, as found in glycerol [Bar13], or a superposition of rotational and translational motions. Specific heat measurements of amorphous, orientationally disorderd and of crystalline ethanol at low temperatures have revealed, that the density of tunneling states in the orientational and the structurally amorphous glass is the same [Tal02], showing that the exact type of tunneling systems may be unimportant for physical properties of glasses. At the same time, the molecular weight of organic glass former strongly influences tunneling rates in spectroscopic measurements [Ere11], and the contribution of tunneling systems to the specific heat of ultrastable glasses of indomethacin can both be completely suppressed [PC14] and recovered by heating the glass and cooling it back down. This indicates that interactions of tunneling systems with their surroundings and each other may play a crucial role.

Here, we will remain within the framework of the standard tunneling model, and therefore keep the phenomenological description of two-level systems without specifying them further. In order to calculate energy eigenstates of a given two-level system, we need to solve the time independent Schrödinger equation

$$H\psi(x) = E\psi(x) \tag{2.6}$$

with the well known Hamilton operator

$$H = -\frac{\hbar^2}{2m}\frac{\mathrm{d}^2}{\mathrm{d}x^2} + V(x)\,. \tag{2.7}$$

We now assume the total wave function of the double well potential to be a linear superposition of the two wave functions $\psi_1(x)$ and $\psi_2(x)$ of the two harmonic

potentials of the single wells

$$\psi_1(x) = \left(\frac{4\lambda}{\pi d^2}\right)^{1/4} \mathrm{e}^{-\frac{\lambda}{2}\left(\frac{2x}{d}+1\right)^2} \quad \text{and} \quad \psi_2(x) = \left(\frac{4\lambda}{\pi d^2}\right)^{1/4} \mathrm{e}^{-\frac{\lambda}{2}\left(\frac{2x}{d}-1\right)^2} . \tag{2.8}$$

Here

$$\lambda := \frac{\xi d^2}{2\hbar\Omega} = \frac{l}{4\hbar}\sqrt{2mV} \tag{2.9}$$

is the so called tunneling parameter of the system, as calculated by the WKB method, and

$$\Omega = \sqrt{2\frac{\xi}{m}} \tag{2.10}$$

is the eigenfrequency of the wells.

The superposition of the single well wave functions

$$\psi(x) = c_1\psi_1(x) + c_2\psi_2(x) \tag{2.11}$$

is justified in the case of weak overlap, that is a large λ, with c_1 and c_2 appropriate coefficients.

The eigenfunctions of the double well potential are then a symmetric and asymmetric superposition of the single well potentials, specifying c_1 and c_2 to

$$\psi_+(x) = \psi_1(x)\cos(\varphi) + \psi_2(x)\sin\varphi \tag{2.12a}$$
$$\psi_-(x) = -\psi_1(x)\sin(\varphi) + \psi_2(x)\cos\varphi . \tag{2.12b}$$

The mixing angle φ of the two eigenfunctions can be calculated by solving the Schrödinger equation of the system. When turning to the matrix notation of the system, we can derive the matrix elements via the eigenequation

$$c_i\left(H_{ji} - ED_{ji}\right) = 0 \tag{2.13}$$

which gives us the matrix elements

$$H_{ji} = \langle\psi_j| H |\psi_i\rangle \tag{2.14}$$

and the overlap of the wave functions

$$D_{ji} = \langle\psi_j|\psi_i\rangle \tag{2.15}$$

which in turn computes to

$$D_{11} = D_{22} = 1 \qquad \text{and} \qquad D_{12} = D_{21} = \mathrm{e}^{-\lambda} \,. \tag{2.16}$$

This leads to the diagonal elements

$$H_{11} = \frac{\hbar\Omega}{2} + \frac{\Delta}{2} \qquad \text{and} \qquad H_{22} = \frac{\hbar\Omega}{2} - \frac{\Delta}{2} \tag{2.17}$$

and the off diagonal elements

$$H_{12} = H_{21} = -\frac{\hbar\Omega}{2}\,\mathrm{e}^{-\lambda} := -\frac{\Delta_0}{2} \tag{2.18}$$

of the matrix, where the newly defined Δ_0 is the so called tunneling splitting, the energy splitting created by coupling the two eigenfuctions of the single wells. With equations (2.16) to (2.18) we can calculate the energy values

$$E_{\pm} = \frac{\hbar\Omega}{2} \pm \frac{1}{2}\sqrt{\Delta^2 + \Delta_0(\lambda)^2} \tag{2.19}$$

of the system and their difference

$$E = \sqrt{\Delta^2 + \Delta_0^2} \,. \tag{2.20}$$

For further calculations, it is very useful to return to the matrix representation of the Schrödinger equation, which in the base of the eigenfunctions of the single wells in coordinate space and not including $\hbar\Omega$ (since it will cancel out in all further calculations), just gives

$$H_0 = \frac{1}{2}\begin{pmatrix} \Delta & -\Delta_0 \\ -\Delta_0 & -\Delta \end{pmatrix} \,. \tag{2.21}$$

As we are mostly interested in energies, we will transform equation (2.21) into its energy eigenstate via a rotation by

$$R = \begin{pmatrix} \cos(\varphi) & -\sin(\varphi) \\ \sin(\varphi) & \cos(\varphi) \end{pmatrix} \tag{2.22}$$

with $\tan(2\varphi) = \Delta_0/\Delta$, the same φ as in (2.12). This then simply yields

$$\tilde{H}_0 = \frac{1}{2}\begin{pmatrix} E & 0 \\ 0 & -E \end{pmatrix} \tag{2.23}$$

Until now, we have not yet considered a perturbation of the two-level system from its equilibrium. In general, the Hamiltonian of any perturbation in coordinate space, where the perturbation is applied, can be written as

$$H_{\mathrm{pert}} = \frac{1}{2}\begin{pmatrix} \delta\Delta & \delta\Delta_0 \\ \delta\Delta_0 & -\delta\Delta \end{pmatrix} \tag{2.24}$$

The change in Δ_0, however, is usually neglected, because weak perturbations, as assumed here, will directly affect the asymmetry energy Δ while a change the overlap of the wave functions characterized by the tunneling splitting Δ_0 is exponentially suppressed [Phi87].
An intuitive picture of a weak perturbation is the movement of the surrounding atomic configuration of the two wells. Such a rearrangement can easily change the energetic landscape enough to modify the asymmetry between two wells. The tunneling splitting, however, is most easily accessible via their distance d, which hardly changed by small rearrangements in the surroundings of the double well potential.
The general perturbation then, if transformed into the energy eigenframe of the system, gives us

$$\tilde{H}_{\text{pert}} = \frac{1}{2E}\begin{pmatrix} \Delta & \Delta_0 \\ \Delta_0 & -\Delta \end{pmatrix} \cdot \delta\Delta. \tag{2.25}$$

and thereby directly delivers an expression for the perturbation of the energy eigenvalue E:

$$\delta E = \frac{1}{2}\frac{\Delta}{E}\delta\Delta \tag{2.26}$$

The cause for the change in the asymmetry energy $\delta\Delta$ can, for example, be due to a distortion of the two-level systems environment in acoustic measurements or, as in the case of this thesis, due to electric fields.
When looking again at the energy levels, they should be changed due to the applied strain by

$$E = \sqrt{\Delta_0^2 + (\Delta + \delta\Delta)^2}\,. \tag{2.27}$$

The change in the asymmetry energy should thus lead to a hyperbolic dependence of the change in the two-level system's energy splitting on external strain. This has indeed been observed both with elastic strain [Gra12, Lis15] and electric fields [Sar16].

2.3.2 Interaction of two-level systems with electric fields

In section 2.3.1, we considered a very general perturbation of the two-level system. As this thesis concerns the dielectric properties of glasses via electric fields, we can specify the perturbation (2.26) to $\delta\Delta = 2\boldsymbol{p}\boldsymbol{F}$ which leads to a change in energy of

$$\delta E = \boldsymbol{p}\boldsymbol{F}\frac{\Delta}{E}\,. \tag{2.28}$$

Here, $\boldsymbol{p}$ is the dipole moment of the two-level system and $\boldsymbol{F}$ the electric field applied. We will not consider static electric fields here but only sinusoidal ac electric fields:

$$\boldsymbol{F}(t) = \boldsymbol{F}_0 \cdot \mathrm{e}^{\mathrm{i}\omega t} \tag{2.29}$$

Since the electric field is then time dependent, we need to solve the time dependency of the two-level system, in order to find its response to the field. Like any two-level system, it can be treated completely analogous to a particle of spin $\boldsymbol{S} = 1/2$ in a magnetic field $\boldsymbol{B}$. We can therefore use the Bloch equations developed in [Blo46] in order to find the response of the tunneling system to ac electric fields. This was first calculated in [Hun76], we will here closely follow the notation of [Car94, Esq98]. Using the notation of magnetic fields and remaining in the energy frame, we immediately find the analogon

$$\begin{aligned}\tilde{H} = \tilde{H}_0 + \tilde{H}_{\text{pert}} &= \frac{1}{2}\begin{pmatrix} E & 0 \\ 0 & -E \end{pmatrix} + \frac{1}{E}\begin{pmatrix} \Delta & \Delta_0 \\ \Delta_0 & -\Delta \end{pmatrix} \cdot \boldsymbol{pF} \\ &= S^z E + \frac{1}{E}(\Delta S^z - \Delta_0 S^x) \cdot \boldsymbol{pF} \\ &:= S^z E + \hat{\boldsymbol{p}}\boldsymbol{F} \\ &:= \gamma \boldsymbol{S}\boldsymbol{B}_0 + \gamma \boldsymbol{S}\boldsymbol{B}_1\end{aligned} \tag{2.30}$$

In order to express the spin in a matrix form, we have made use of the Pauli matrices

$$S^x = \frac{1}{2}\begin{pmatrix} 0 & 1 \\ 1 & 0 \end{pmatrix} \tag{2.31a}$$

$$S^y = \frac{1}{2}\begin{pmatrix} 0 & -\mathrm{i} \\ \mathrm{i} & 0 \end{pmatrix} \tag{2.31b}$$

$$S^z = \frac{1}{2}\begin{pmatrix} 1 & 0 \\ 0 & -1 \end{pmatrix} . \tag{2.31c}$$

and introduced the spin operator of the dipole moment

$$\hat{\boldsymbol{p}} = (\Delta S^z + \Delta_0 S^x)\boldsymbol{p} . \tag{2.32}$$

The analogon directly gives us the two equivalents $-\hbar\gamma \boldsymbol{B}_0 = (0, 0, E)$ for the static energy splitting and $-\hbar\gamma \boldsymbol{B}_1 = (\Delta_0/E, 0, \Delta/E)\boldsymbol{pF}\cos(\omega t)$ for the time dependent perturbation, where γ is the gyromagnetic ratio. In the case of spin $1/2$ particles in magnetic fields, the static field causes a level splitting, thus creating a two-level system. In the case of two-level systems in amorphous solids no static electric field is needed, since the level splitting comes directly from the potential landscapes in which the atoms move.

We will, until the end of this section, use the spin and B-field notation, rather than the polarization and E-field, as it is more common in literature and then translate the obtained results at the end of the section.

In the case of a spin $1/2$ particle in a magnetic field, the static component is usually chosen to point along the z-axis, the spin being aligned along the field and in

thermal equilibrium. The perturbation, which in this case has components in z and x direction, will destroy thermal equilibrium in the system, to which it will return with a characteristic relaxation time τ_1.

Ignoring the relaxational terms, we simply find

$$\frac{\mathrm{d}\boldsymbol{S}}{\mathrm{d}t} = \gamma \boldsymbol{S} \times \boldsymbol{B} \tag{2.33}$$

for the time dependence of a spin in a magnetic field, where the spin is freely precessing around the axis defined by the magnetic field. It is practical to transform the system into a frame rotating with the frequency ω of the ac-field around the z-axis:

$$\frac{\mathrm{d}\boldsymbol{S}}{\mathrm{d}t} = \boldsymbol{S} \times [(\omega_0 - \omega)\boldsymbol{z} + \omega_1 \boldsymbol{x}'] \tag{2.34}$$

Here, $\omega_0 = \gamma|\boldsymbol{B}_0|$ and $\omega_1 = \gamma|\boldsymbol{B}_1|$ and $\boldsymbol{x}'$ is the new x-axis of the rotating frame.

In a realistic environment, we will find both longitudinal relaxation processes returning the spin to its original alignment along the z-axis with the time constant τ_1,and processes destroying phase coherence with the time constant τ_2 of transverse relaxation. These will be discussed in more detail in chapter 2.3.4 but introduced to the calculations here. Note, that $\tau_2 < \tau_1$ in order for the total spin to be preserved.

If we consider both relaxation and phase decoherence, we find

$$\frac{\mathrm{d}S^x}{\mathrm{d}t} - \gamma(S^y B_z - S^z B_y) + \frac{1}{\tau_2} S^x = 0 \tag{2.35a}$$

$$\frac{\mathrm{d}S^y}{\mathrm{d}t} - \gamma(S^z B_x - S^x B_z) + \frac{1}{\tau_2} S^y = 0 \tag{2.35b}$$

$$\frac{\mathrm{d}S^z}{\mathrm{d}t} - \gamma(S^x B_y - S^y B_x) + \frac{1}{\tau_1}(S^z - \langle S^z \rangle) = 0 \tag{2.35c}$$

with $\langle S^z \rangle$ the expectation value of S^z which is given by the thermal equilibrium value $\langle S^z \rangle = 1/2 \tanh(\gamma \hbar B_z(t)/2k_\mathrm{B}T)$.
If we only consider the case of small perturbations by the ac field, as is the case in the linear regime, we can linearize the Bloch equations around the unperturbed solution and only keep first order terms of $\boldsymbol{B}_1$. This means expanding $\langle S^z \rangle$ in a Taylor series

$$\begin{aligned} \langle S^z \rangle (\boldsymbol{B}) &= \langle S^z \rangle_0 + \left. \frac{\partial \langle S^z \rangle}{\partial B + \boldsymbol{SB}} \right|_{B=0} \boldsymbol{SB} \\ &= -\frac{1}{2} \tanh\left(\frac{\gamma \hbar B_z}{2k_\mathrm{B}T}\right) - \operatorname{sech}^2\left(\frac{\gamma \hbar B_z}{2k_\mathrm{B}T}\right) \frac{\boldsymbol{SB}}{2k_\mathrm{B}T} \end{aligned} \tag{2.36}$$

and finding solutions for the Bloch equations of the form $S(t) = S_0(t) + S_1(t)$.

The resulting differential equations for S_0^z and the components of $\mathbf{S}_1$ are as follows:

$$\frac{\mathrm{d}S_0^z}{\mathrm{d}t} + \frac{1}{\tau_1}(S_0^z(t) - S_0^z(\infty)) = 0 \tag{2.37a}$$

$$\frac{\mathrm{d}S_1^x}{\mathrm{d}t} - \omega_0 S_1^y + \frac{1}{\tau_2} S_1^x = 0 \tag{2.37b}$$

$$\frac{\mathrm{d}S_1^y}{\mathrm{d}t} - \omega_0 S_1^x + \frac{1}{\tau_2} S_1^y - 2\gamma B_1^x S_0^z(t) = 0 \tag{2.37c}$$

$$\frac{\mathrm{d}S_1^z}{\mathrm{d}t} + \frac{1}{\tau_1}\left(S_1^z + \frac{\hbar}{4k_\mathrm{B}T}\operatorname{sech}^2\left(\frac{E}{2k_\mathrm{B}T}\right)\gamma B_1^z\right) = 0 \tag{2.37d}$$

Until now, the differential equations for S^x and S^y are still coupled, making them hard to solve. In order to decouple them, we introduce $S^\pm = S_1^x \pm \mathrm{i}S_1^y$

$$\frac{\mathrm{d}S^+(t)}{\mathrm{d}t} + \mathrm{i}\left(\omega_0 - \frac{\mathrm{i}}{\tau_2}\right) S^+(t) - \mathrm{i}2\gamma B_1^x S_0^z(t) = 0 \tag{2.38}$$

and the complex conjugate for S^-. We can now solve the differential equations (2.37a), (2.37d) and(2.38), the detailed solutions can be found in [Esq98]. Having solved the equations, we can turn back to the dipole in an electric field and calculate the dielectric susceptibility[1] $\chi = \chi' + \mathrm{i}\chi''$, defined by $\chi = \mathrm{d}p_\parallel/\mathrm{d}F_\mathrm{ac}$. We only need to consider the average component of the dipole moment parallel to the ac electric field, which we find using equation (2.32)

$$p_\parallel = -\langle\hat{\boldsymbol{p}}\rangle\cos\theta = -p\cos\theta\left(\frac{2\Delta S_1^z(t)}{E} + \frac{\Delta_0(S^+S^-)}{E}\right) \tag{2.39}$$

where we have to use the solutions to the time dependent spin components.

We can then break the dielectric susceptibility down into the following components, according to their dependence on τ_1 and τ_2 and being in phase and out of phase with the electric field, as well as their time dependence:

$$\chi'_\mathrm{rel} = \frac{p_0^2\cos^2(\theta)}{k_\mathrm{B}T}\left(\frac{\Delta}{E}\right)^2\operatorname{sech}^2\left(\frac{E}{2k_\mathrm{B}T}\right)\frac{1}{1+\omega^2\tau_1^2} \tag{2.40}$$

$$\chi''_\mathrm{rel} = \frac{p_0^2\cos^2(\theta)}{k_\mathrm{B}T}\left(\frac{\Delta}{E}\right)^2\operatorname{sech}^2\left(\frac{E}{2k_\mathrm{B}T}\right)\frac{\omega\tau_1}{1+\omega^2\tau_1^2} \tag{2.41}$$

$$\begin{aligned}\chi'_\mathrm{res} = {}& \frac{p_0^2\cos^2(\theta)}{\hbar}\left(\frac{\Delta_0}{E}\right)^2\tanh\left(\frac{E}{2k_\mathrm{B}T}\right)\\ & \times\left(\frac{(\omega-\omega_0)\tau_2^2}{1+(\omega-\omega_0)^2\tau_2^2} - \frac{(\omega+\omega_0)\tau_2^2}{1+(\omega+\omega_0)^2\tau_2^2}\right)\end{aligned} \tag{2.42}$$

[1] In order to avoid confusion, we will use the susceptibility χ when treating single tunneling systems and the dielectric function ε when treating the total signal created by summing over all tunneling systems of the sample.

$$\chi''_{\text{res}} = \frac{p_0^2 \cos^2(\theta)}{\hbar} \left(\frac{\Delta_0}{E}\right)^2 \tanh\left(\frac{E}{2k_{\text{B}}T}\right) \times \left(\frac{\tau_2}{1+(\omega-\omega_0)^2\tau_2^2} - \frac{\tau_2}{1+(\omega+\omega_0)^2\tau_2^2}\right) \tag{2.43}$$

$$\chi'_{\text{time}} = \frac{2p_0^2 \cos^2(\theta)}{\hbar} \left(\frac{\Delta_0}{E}\right)^2 \left(a + \frac{1}{2}\tanh\left(\frac{E}{2k_{\text{B}}T}\right)\right) \mathrm{e}^{-t/\tau_1} \times \left(\frac{(\omega-\omega_0)\tau_{12}^2}{1+(\omega-\omega_0)^2\tau_{12}^2} - \frac{(\omega+\omega_0)\tau_{12}^2}{1+(\omega+\omega_0)^2\tau_{12}^2}\right) \tag{2.44}$$

$$\chi''_{\text{time}} = \frac{2p_0^2 \cos^2(\theta)}{\hbar} \left(\frac{\Delta_0}{E}\right)^2 \left(a + \frac{1}{2}\tanh\left(\frac{E}{2k_{\text{B}}T}\right)\right) \mathrm{e}^{-t/\tau_1} \times \left(\frac{\tau_{12}}{1+(\omega-\omega_0)^2\tau_{12}^2} - \frac{\tau_{12}}{1+(\omega+\omega_0)^2\tau_{12}^2}\right) \tag{2.45}$$

Note, that (2.44) and (2.45) contain $\tau_{12}^{-1} = \tau_1^{-1} - \tau_2^{-1}$ and the starting value $a = S_0^z(0)$ of the spin in z direction and that their contribution decays exponentially with e^{-t/τ_1}, so that they become unimportant for equilibrium measurements as performed in the course of this thesis and were only included for the sake of completeness.

The different contribution to the dielectric susceptibility listed above all scale with

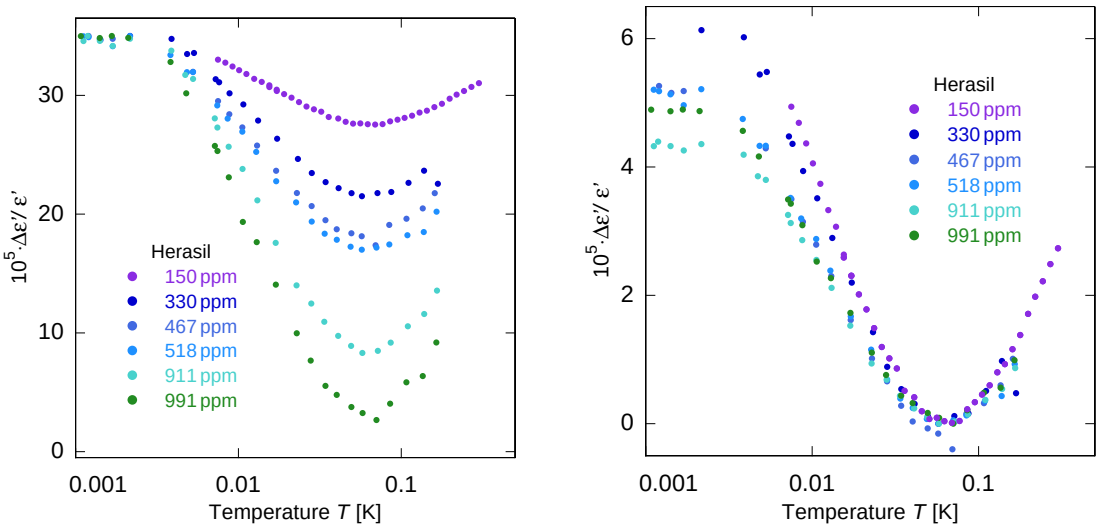

Figure 2.7: Real part of the dielectric signal measured on vitreous silica with varying hydroxyl ion concentrations (left) and scaled proportional to the ion concentration (right). Data from [vR98], 150 ppm data from[Luc11].

the square of the dipole moment p_0 involved in the tunneling motion. The total dielectric signal of a glass will therefore be governed by the tunneling systems with the largest dipole moments.
An example for this effect is shown in figure 2.7, where the signal in vitreous silica with varied concentrations of hydroxyl ions [vR98] and [Luc11] is shown as measured, and scaled with the hydroxyl ion concentration. It is clearly shown, that the signal only depends on the ionic concentration over a large temperature range. The contribution of the silicate matrix is not visible, as the tunneling systems' dipole moments are far smaller than those of the ions.

2.3.3 Distribution of the parameters

So far, we have only considered an isolated two-level system and its dynamics. In an amorphous solid, however, we find many two-level systems with a broad range of parameters due to the inherent disorder of the amorphous state. This distribution enters into all macroscopic properties of the material, such as its heat capacity, thermal conductivity, acoustic and dielectric properties.
The standard tunneling model simply assumes a flat distribution in the independent parameters Δ and λ

$$P(\Delta, \lambda)\,\mathrm{d}\Delta\mathrm{d}\lambda = P_0\,\mathrm{d}\Delta\mathrm{d}\lambda \tag{2.46}$$

where P_0 is an experimentally determined constant. Using (2.9) and (2.18) we can use a Jacobi transformation to obtain a distribution function of the parameters Δ_0 and E, that are more useful for later integrations:

$$P(\Delta_0, E)\,\mathrm{d}\Delta_0\mathrm{d}E = P_0 \frac{E}{\Delta_0\sqrt{E^2 - \Delta_0^2}}\,\mathrm{d}\Delta_0\mathrm{d}E \tag{2.47}$$

The distribution as a function of the parameter Δ_0/E is shown in figure 2.8. It diverges both at large tunneling splittings $\Delta_0 = E$ and at very small ones $\Delta_0 = 0$. While the first divergence can be integrated, we need to introduce a minimal tunneling splitting $\Delta_{0,\mathrm{min}}$, in order to make the latter integrable. A non-integrable distribution function would not be physically sensible, since there is only a finite amount of tunneling systems in a given sample. The minimal tunneling splitting can be chosen arbitrarily small[2], and in this case does not influence the outcome of a macroscopic property obtained by integration over all tunneling systems. The minimal splitting corresponds to a maximum in energy barriers separating two wells still considered as a double well potential and not as two isolated wells.

[2] A practical choice is to use a $\Delta_{0,\mathrm{min}} \approx 1/1000 \cdot T_\mathrm{m}$, where T_m is the lowest temperature measured in experiment.

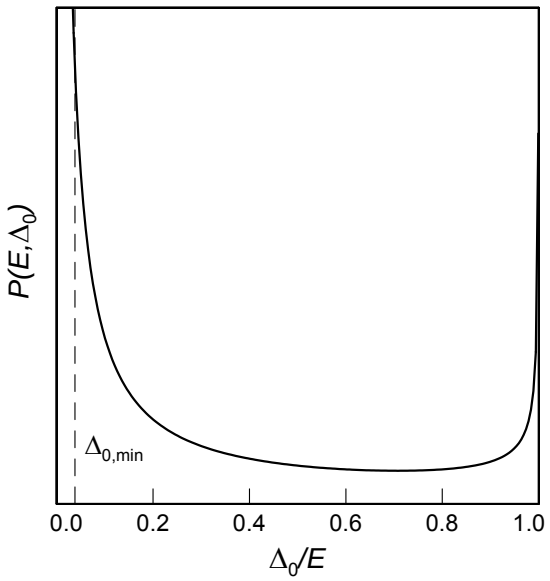

Figure 2.8: Distribution of two-level systems as a function of the parameter Δ_0/E. The minimal tunneling splitting $\Delta_{0,\mathrm{min}}$ is needed to make the singularity at $\Delta_0 = 0$ integrable.

Note, that the distribution of parameters applies to all tunneling systems present in the sample. Via dielectric measurements as conducted in this thesis, we can, however, only access those with a sizable dipole moment $\boldsymbol{p}$, which couples to externally applied electric fields. While this is only a subset of all tunneling systems, it is generally assumed that it will also show a broad distribution in its parameters. We can thus use the distribution function (2.47) but with an effective P_0 which will be potentially smaller from the one that would be found when making analogous acoustic measurements.

2.3.4 Interactions of two-level systems with their environment

The equations for the dielectric functions (2.40) to (2.43) describe to different types, namely relaxational and resonant, of interaction of the tunneling systems with their environment [Pic74]. For both types of interaction we will first consider a single two-level system and then consider the effect of different frequencies and temperatures on the whole ensemble by summing up over the distribution given by equation (2.47).

Relaxational interaction

The first type of interaction, as described in (2.40) and (2.41) is that of a Debye relaxation [Deb13]. Its frequency dependence is shown in figure 2.9 using the example of a complex dielectric function $\varepsilon = \varepsilon' + \mathrm{i}\varepsilon''$. The relevant time constant for relaxational interaction is that of the longitudinal relaxation time τ_1. Given a constant relaxation time τ_1 and beginning at low frequencies, the system can at low frequencies completely follow the change of the energy energy splitting caused by

the electric field, leading to a maximum of the signal of ε' in phase with the electric field. In this regime of low frequencies, the system does not show any loss, that would show as a signal phase shifted 90° in respect to the electric field and thus in ε''. At higher frequencies, the system starts to lag in its response to the field, and at $\omega\tau_1 = 1$ has a maximum both in the loss and in the change of signal in phase. At highest frequencies, the system does not follow the electric field at all any more and is effectively static. This then means, that there is neither a loss, nor a signal in phase.

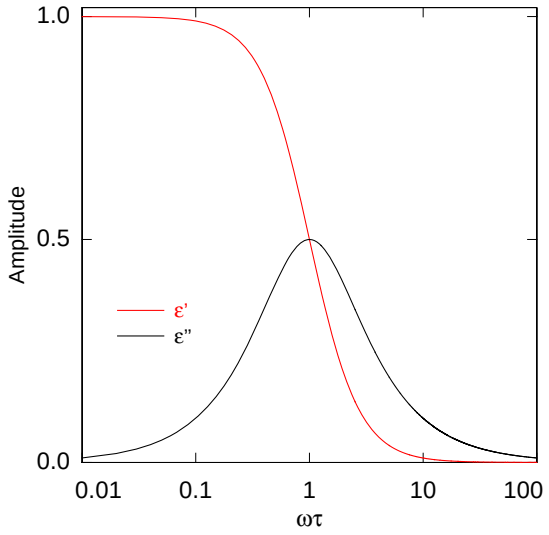

Figure 2.9: Real part ε' (black) and loss ε'' (red) of a Debye like relaxation as described in (2.40) and (2.41) as a function of $\omega\tau_1$.

Relaxation by thermal phonons The only relaxation mechanism considered to be present in dielectric glasses at lowest temperatures is due to interaction of the two-level systems with phonons. An applied electric field causes a change the energy splitting E of the tunneling systems, as shown schematically in 2.10. This drives the occupation out of thermal equilibrium determined by $\tanh(E/2k_\mathrm{B}T)$, so the tunneling system will effectively relax back into thermal equilibrium by absorbing or emitting a thermal phonon. At temperatures below about one kelvin, the number of phonon has dropped significantly, so that only interactions with single phonons need to be taken into account. Above this temperature the number of phonons is getting large enough that we also have to include two phonon processes, calculated in more detail in [Dou80]. As before, we will assume an isotropic medium and only the variation of Δ with the electric field. We will also neglect the tensorial character of the electric field and only assume a mean field for the calculations.
The longitudinal and two transversal phonon branches are considered by including different couplings γ_i of the phonons to the strain induced by the electric field on

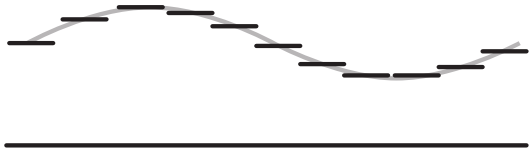

Figure 2.10: Schematic picture of a two-level system being modified by an oscillating electric field. The energy splitting is constantly shifted, causing the system to relax back to the current thermal equilibrium.

two-level systems containing dipole moments.

For each possible transition, the transition probability is calculated using Fermi's golden rule, which for the one phonon process gives us

$$W_{12} = \frac{2\pi}{\hbar} |\left\langle \Psi_2 | \tilde{H} | \Psi_1 \right\rangle|^2 D(E) f(E) \delta(\hbar\omega = E) \tag{2.48}$$

where $f(E)$ is the Bose-Einstein distribution and $D(E)$ is the density of states of the phonons in the Debye model, which is given by

$$D(E) = \frac{E^2}{2\pi^2 \hbar^3 v_\alpha^3}. \tag{2.49}$$

The velocity of sound v_α is different for longitudinal and transversal phonons. The relaxation rate can now be obtained by adding the transition rate of absorption and emission: $\tau^{-1} = W_{12} + W_{21}$ [Jäc72]. For the one phonon process we obtain

$$\tau_{1\mathrm{ph}}^{-1} = K_1 \left(\frac{\Delta_0}{E}\right)^2 E^3 \coth\left(\frac{E}{2k_\mathrm{B}T}\right) = \left(\frac{\gamma_l^2}{v_l^5} + 2\frac{\gamma_l^2}{v_l^5}\right) \left(\frac{\Delta_0}{E}\right)^2 \left(\frac{E^3}{2\pi\rho\hbar^4}\right) \coth\left(\frac{E}{2k_\mathrm{B}T}\right) \tag{2.50}$$

where ρ is the density of the sample and the indices l and t correspond to the longitudinal and transversal phonon branches respectively. The coupling constant K_1 determines the strength of the one phonon relaxation via the coupling constant $\gamma \approx 0.2 - 1\,\mathrm{eV}$ [Hun76] between phonons and tunneling systems and the sound velocity, and thereby the relaxation rates $\tau_{1\mathrm{ph}}^{-1}$.
In principle, one can thus calculate the strength of the one phonon interaction from material properties. These are, however, not always known and thus K_1 is used as a free parameter in the numeric calculations performed throughout this thesis.
A similar calculation for the two phonon process, which is a first order Raman process, leads to [Dou80]

$$\tau_{2\mathrm{ph}}^{-1} = K_2 \left(\frac{\Delta_0}{E}\right)^2 T^7 F(x) \tag{2.51}$$

Here, the coupling constant for this process given by

$$K_2 = \frac{k_\mathrm{B}^7}{\pi^3 2\rho^2\hbar^7} \sum \frac{\delta_{\alpha,\sigma}^2}{v_\alpha^{10}} \tag{2.52}$$

where we again sum over the longitudinal and transversal phonon branches and $\delta \approx 100\,\mathrm{eV}$ [Dou80] is the second order coupling term, describing the coupling of two phonons and a tunneling system. It is much larger than γ, Finally, the function $F(x)$ where $x = E/2k_\mathrm{B}T$ is given by

$$F(x) = \frac{x}{70}(x^2+\pi^2)(x^4 - \pi^2x^2 + {}^{10}\!/_3\pi^4)\coth(x)\,. \tag{2.53}$$

The total relaxation rate τ_1^{-1} is always given by the sum of all rates, in this case the one phonon and the Raman process:

$$\tau_1^{-1} = \tau_{1\mathrm{ph}}^{-1} + \tau_{2\mathrm{ph}}^{-1}. \tag{2.54}$$

Total relaxational contribution By summing up the relaxational response of a single two-level system as given by equations (2.40) and (2.41) over the distribution of all two-level systems (2.47) and using the total relaxation rate (2.54) for τ_1^{-1} one obtains the total relaxational contribution to the dielectric function

$$\begin{aligned}\frac{\delta\varepsilon'_\mathrm{rel}}{\varepsilon'} &= \frac{1}{3\varepsilon_0\varepsilon_\mathrm{r}} \int_{\Delta_{0,\min}}^{E_\mathrm{max}} \mathrm{d}E \int_{\Delta_{0,\min}}^{E} \mathrm{d}\Delta_0\, \chi'_{rel}\, P(E,\Delta_0) \\ &= \frac{2}{3\varepsilon_0\varepsilon_\mathrm{r}} \frac{p_0^2 P_0}{k_\mathrm{B}T} \int_{\Delta_{0,\min}}^{E_\mathrm{max}} \mathrm{d}E \int_{\Delta_{0,\min}}^{E} \mathrm{d}\Delta_0 \left(1 - \frac{\Delta_0^2}{E^2}\right) \mathrm{sech}^2\left(\frac{E}{2k_\mathrm{B}T}\right) \frac{1}{1+\omega^2\tau_1^2} \frac{E}{\Delta_0\sqrt{E^2-\Delta_0^2}}\end{aligned} \tag{2.55}$$

$$\begin{aligned}\frac{\varepsilon''_\mathrm{rel}}{\varepsilon'} &= \frac{1}{3\varepsilon_0\varepsilon_\mathrm{r}} \int_{\Delta_{0,\min}}^{E_\mathrm{max}} \mathrm{d}E \int_{\Delta_{0,\min}}^{E} \mathrm{d}\Delta_0\, \chi''_{rel}\, P(E,\Delta_0) \\ &= \frac{2}{3\varepsilon_0\varepsilon_\mathrm{r}} \frac{p_0^2 P_0}{k_\mathrm{B}T} \int_{\Delta_{0,\min}}^{E_\mathrm{max}} \mathrm{d}E \int_{\Delta_{0,\min}}^{E} \mathrm{d}\Delta_0 \left(1 - \frac{\Delta_0^2}{E^2}\right) \mathrm{sech}^2\left(\frac{E}{2k_\mathrm{B}T}\right) \frac{\omega\tau_1}{1+\omega^2\tau_1^2} \frac{E}{\Delta_0\sqrt{E^2-\Delta_0^2}}\end{aligned} \tag{2.56}$$

Additionally, we have used the relation $\varepsilon' = \varepsilon_0\varepsilon_\mathrm{r}$ and averaged over all possible angles between the dipole moments and the electric field. This gives us the factor $\int_{-1}^{1}\cos^2\theta\mathrm{d}\theta = 2/3$.
As is traditionally the case the equations give the relative change of the real part

of the dielectric function $\delta\varepsilon'/\varepsilon'$ rather than its absolute value. This allows for a rearrangement of the curves by adding appropriate constants. The loss tangent $\varepsilon''/\varepsilon' = \tan(\delta)$ is given as an absolute value here, but only its change can be measured with enough precision in many measurements.

Equations (2.55) and (2.56) have been used to perform numeric calculations of

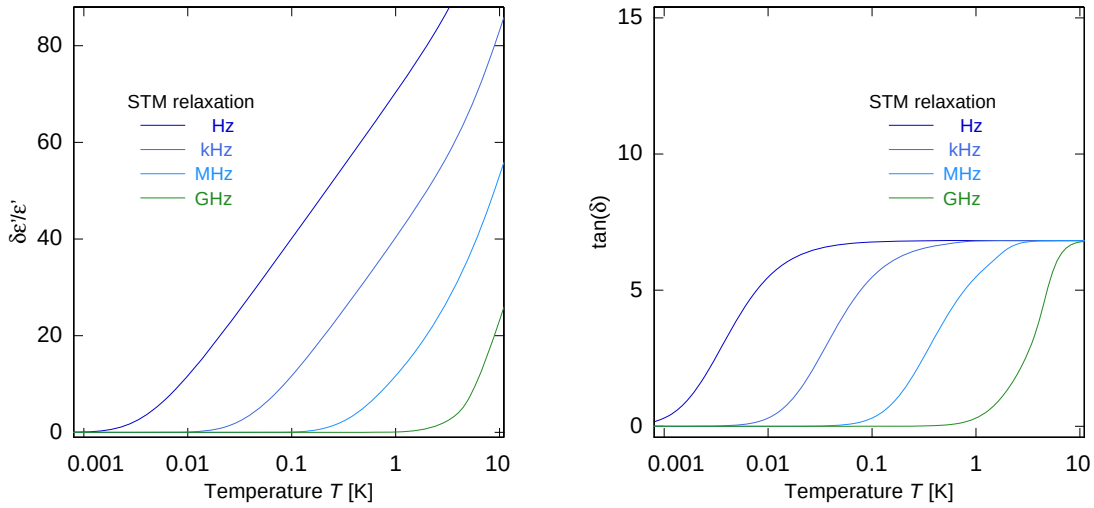

Figure 2.11: Numerically calculated change of the real part of the dielectric function $\delta\varepsilon'_{rel}/\varepsilon'$ (left) and loss tangent $\tan(\delta)$ (right) due to relaxation as a function of temperature between 1 mK and 10 K for frequencies between 1 Hz and 1 GHz. Parameters were chosen similar to those found in experiments.

the temperature and frequency dependence of the signal, using the parameters specified in (2.60). As measurements were performed with set frequencies $\nu = \omega/2\pi$, we will use ν when treating calculations for different frequencies, while keeping ω when treating relaxational interactions, as relevant regimes are characterized by $\omega\tau$.
The results of numeric calculations are shown in 2.11, where the left part of the figure shows the change of the real part of the dielectric function $\delta\varepsilon'/\varepsilon'$ due to relaxation as a function of temperature and for frequencies from 1 Hz to 1 GHz. At lowest temperatures, there is no contribution to the dielectric function for any frequency. The relaxation times τ_1 are so long in this temperature regime, that $\omega\tau_1 \gg 1$ for all two-level systems, leading to no contribution to the real part of the dielectric function. Due to the fact that we change ω and that τ_1 is strongly temperature dependent, the position of $\omega\tau_1 = 1$ is different for changing frequencies. The onset of the relaxational contribution to $\delta\varepsilon'/\varepsilon'$ lies at lowest temperatures for the lowest frequencies and then shifts with $T^{1/3}$. This is due to the fact, that the single phonon rate (2.50) is effectively proportional to E^3 and dominant phonons with $E \approx k_B T$ contribute strongest to the signal. For temperatures above the onset temperature, we see a rise in the signal that is logarithmic with temperature as more and more

two-level systems contribute.
The onset of the two phonon process can be seen by a steepening of the slope of $\delta\varepsilon'/\varepsilon'$. Its position shifts with $T^{1/7}$ due to the temperature dependence of the two phonon relaxation process (2.51). For the highest frequency depicted here, the onset of the relaxational contribution is at temperatures high enough, that the two phonon process determines its position. The shape of the onset is also distorted when compared to that of a one phonon process, as seen at low frequencies.

The dielectric loss tangent $\tan(\delta)$ due to relaxation is shown in the right part of figure 2.11 as a function of temperature for different frequencies. It is zero at lowest temperatures for all frequencies and, similar to the real part, starts rising at temperatures where $\omega\tau_1$ approaches unity at each frequency. The rise is directly proportional to the energy dependence of the dominant relaxational process and thus shows a T^3 behavior at low frequencies and T^7 at higher ones. We can even see the crossover in the 1 MHz curve, where the slope changes as the two phonon process becomes dominant. Finally, the loss tangent goes over into frequency independent plateau region where $\tan(\delta)$ is constant at high temperatures.

Resonant interaction

The equations (2.42) and (2.43) show the behavior of a resonant interaction, as depicted in figure 2.12. When considering resonant interaction, one usually concentrates on frequencies close to the resonant frequency $\omega = E/\hbar \approx \omega_0$. Here,the systems shows a large contribution to the loss ε'' because the system can very effectively absorb energy, as is shown in the figure. The contribution to real part of the signal ε' is also large, but changes signs at $\omega = \omega_0$.
Since a large part of the measurements in this thesis were performed at low frequencies, where $\hbar\omega \ll k_\mathrm{B}T = E$, it is also necessary to look at resonant interaction far off resonance. For $\omega \ll \omega_0$, we do no longer find a contribution to the loss of the system. However, even down to lowest frequencies where $\omega/\omega_0 \approx 0$, there is a significant contribution to the real part of the signal. The width of the resonance is characterized by the inverse time constant τ_2^{-1} rather than τ_1^{-1} that governs the relaxational processes.
In the picture of the spin in a magnetic field a spin that is tipped out of its equilibrium position can precess freely with its Larmor frequency. Thus, if the two-level system is not disturbed from the outside, it will keep on precessing forever. This leads to $\tau_2 \to \infty$ and an infinitely sharp resonance. However, since in a glass any two-level system is surrounded by other two-level systems which can change their state at any given time influencing their environment, the energy splitting of the

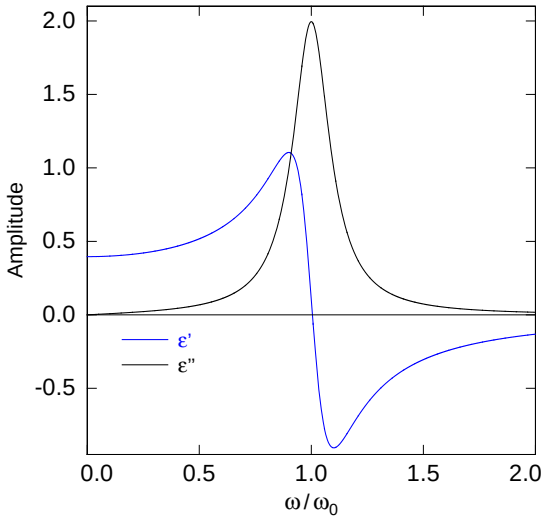

Figure 2.12: Real part ε' (blue) and loss ε'' (black) of a resonant interaction as described in (2.42) and (2.43) as a function of the reduced frequency ω/ω_0.

system can change over time. This causes the system to dephase with the finite time constant τ_2.
Let us consider a situation, where the spin has been completely tipped from the z-direction of the undisturbed system into the xy-plane. The dephasing leads to a reduction of the expectation value of the total spin in the xy-plane of the Bloch sphere, while at the same time relaxation causes the expectation value to increase in the z-direction. In order for conservation of the total spin or polarization to hold, we therefore find $\tau_2 \leq \tau_1$. Measurements in N-BK7 have found values of τ_2 about one to two orders of magnitude smaller than τ_1 [Fic12].

Having considered the resonant interaction of single tunneling systems, we can again sum up over all systems in the sample. This leads to:

$$\begin{aligned}\frac{\delta\varepsilon'_{\mathrm{res}}}{\varepsilon'} &= \frac{2}{3\varepsilon_0\varepsilon_{\mathrm{r}}}\int_{\Delta_{0,\min}}^{E_{\max}} \mathrm{d}E \int_{\Delta_{0,\min}}^{E} \mathrm{d}\Delta_0 \chi'_{res}\, P(E,\Delta_0) \\ &= \frac{-2}{3\varepsilon_0\varepsilon_{\mathrm{r}}}\frac{p_0^2 P_0}{\hbar}\int_{\Delta_{0,\min}}^{E_{\max}} \mathrm{d}E \int_{\Delta_{0,\min}}^{E} \mathrm{d}\Delta_0 \left(\frac{\Delta_0^2}{E^2}\right)\tanh\left(\frac{E}{2k_{\mathrm{B}}T}\right) \\ &\times \left(\frac{(\omega-\omega_0)\tau_2^2}{1+(\omega-\omega_0)^2\tau_2^2} - \frac{(\omega+\omega_0)\tau_2^2}{1+(\omega+\omega_0)^2\tau_2^2}\right)\frac{E}{\Delta_0\sqrt{E^2-\Delta_0^2}}\end{aligned} \tag{2.57}$$

$$\begin{aligned}\frac{\varepsilon''_{\mathrm{res}}}{\varepsilon'} &= \frac{2}{3\varepsilon_0\varepsilon_{\mathrm{r}}}\int_{\Delta_{0,\min}}^{E_{\max}} \mathrm{d}E \int_{\Delta_{0,\min}}^{E} \mathrm{d}\Delta_0 \chi''_{res}\, P(E,\Delta_0) \\ &= \frac{-2}{3\varepsilon_0\varepsilon_{\mathrm{r}}}\frac{p_0^2 P_0}{\hbar}\int_{\Delta_{0,\min}}^{E_{\max}} \mathrm{d}E \int_{\Delta_{0,\min}}^{E} \mathrm{d}\Delta_0 \left(\frac{\Delta_0^2}{E^2}\right)\tanh\left(\frac{E}{2k_{\mathrm{B}}T}\right) \\ &\times \left(\frac{\tau_2}{1+(\omega-\omega_0)^2\tau_2^2} - \frac{\tau_2}{1+(\omega+\omega_0)^2\tau_2^2}\right)\frac{E}{\Delta_0\sqrt{E^2-\Delta_0^2}}\end{aligned} \tag{2.58}$$

The temperature dependence of $\delta\varepsilon'/\varepsilon'$ and $\tan(\delta)$ caused by resonant processes at frequencies ranging from 1 Hz to the GHz regime are shown in figure 2.13. The

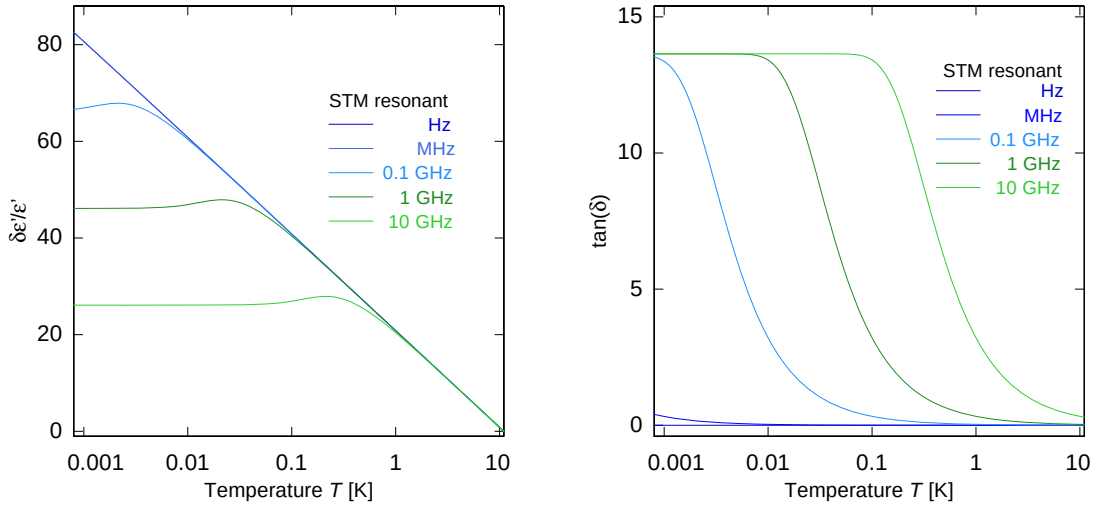

Figure 2.13: Numerically calculated change of the real part of the dielectric function $\delta\varepsilon'_{res}/\varepsilon'$ (left) and loss tangent $\tan(\delta)$ (right) due to resonant processes as a function of temperature between 1 mK and 10 K for frequencies between 1 Hz and the GHz range. Parameters were chosen similar to those found in experiments.

change of the real part of the signal $\delta\varepsilon'/\varepsilon'$ with temperature shows a common logarithmic decline with temperature for frequencies up to about 1 MHz in the relevant temperature range. The decline is caused by the thermal population of the higher one of the two energy levels, leading to a decrease of $\tanh(E/2k_{\mathrm{B}}T)$ towards higher temperatures.

Additionally, we see a branching off of the signal for frequencies in the GHz-regime, where towards low temperatures the signal first shows a maximum and then levels off towards a constant value. This is due to the rise of the resonant signal close to the resonant frequency and the change of sign at $\hbar\omega = k_{\mathrm{B}}T = \hbar\omega_0$.

The loss tangent $\tan(\delta)$ caused by resonant processes is only non-zero when the measurement frequency approaches the resonant frequency at any given temperature. As

ω_0 is at least in the MHz-regime for all relevant temperatures, we only find a resonant contribution to the loss at low temperatures. As shown in the right part of figure 2.13, this contribution increases drastically towards high frequencies. The curves in the GHz regime also show a plateau at lowest temperatures, which again begins at temperatures where the measurement frequency is equal to the resonance frequency of the thermal tunneling systems $\hbar\omega = k_\mathrm{B}T = \hbar\omega_0$.

2.3.5 The dielectric function in the standard tunneling model

The total signal of dielectric measurements is the sum of the relaxational and resonant contributions as treated in sections 2.3.4 and 2.3.4. As an example, figure 2.14 shows the resonant and relaxational contribution, as well as the total signal, of the change of the real part and the loss tangent of the dielectric function. Its contri-

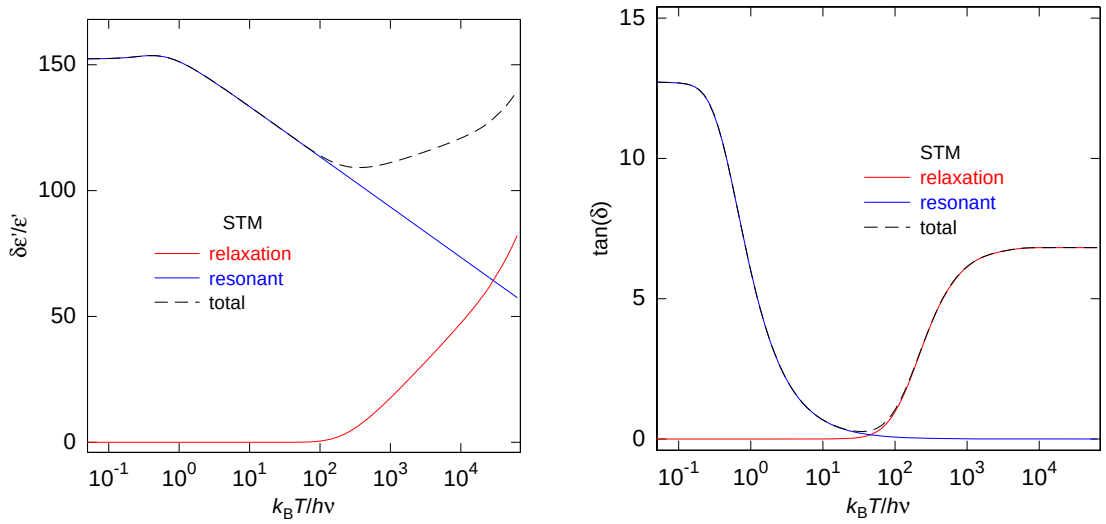

Figure 2.14: Relaxational (red) and resonant (blue) contribution to the total signal $\delta\varepsilon'/\varepsilon'$ (left) and $\tan(\delta)$ (right) as a function of reduced temperature $k_\mathrm{B}T/h\nu$.

bution to both $\delta\varepsilon'/\varepsilon'$ and $\tan(\delta)$ is only significant at high temperatures, while the resonant contribution to the loss tangent $\tan(\delta)$ is negligible at high temperatures. It can therefore be split rather easily into a high temperature region, where only relaxational process contribute and a low temperature region that only shows resonant processes. The real part also has this purely resonant low temperature region and a high temperature region, where both resonant and relaxational processes contribute to the signal. The crossover temperature, defined by the minimum in $\delta\varepsilon'/\varepsilon'$ created by the sum of relaxational and resonant processes, depends on the measurement frequency used in the experiment and allows us to focus on different regions by varying the frequency.

Such a variation of the measurement frequency is shown in figure 2.15, where we see the total change of the dielectric function as a function of temperature for frequencies ranging 1 kHz to 1 GHz. In this figure we can very clearly see how the different

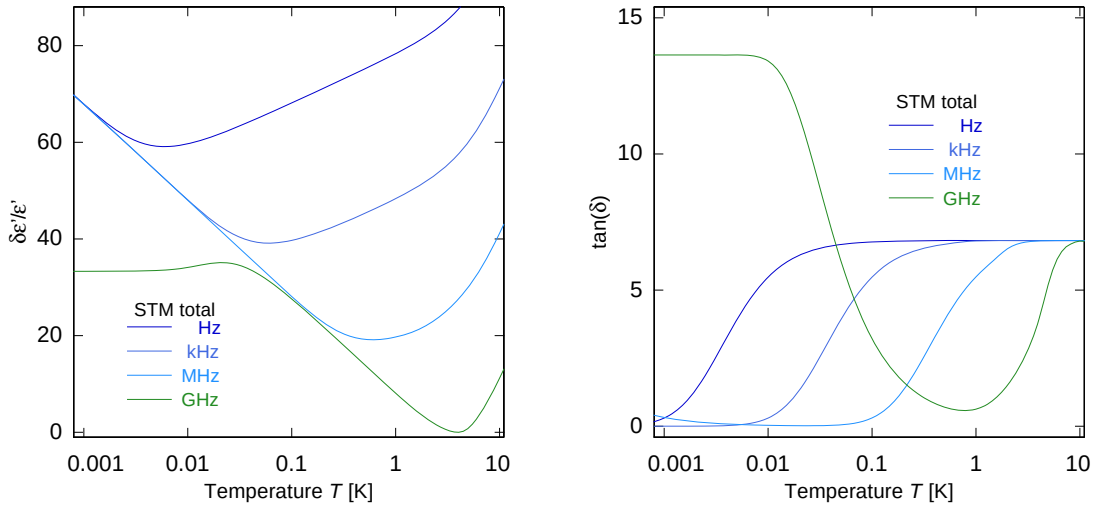

Figure 2.15: Numerically calculated change of the total real part of the dielectric function $\delta\varepsilon'/\varepsilon'$ (left) and loss tangent $\tan(\delta)$ (right) as a function of temperature between 1 mK and 10 K for frequencies between 1 Hz and 1 GHz. Parameters were chosen similar to those found in experiments, as given in (2.60).

frequencies lead to a shift of the crossover temperature and thus to a better insight into either the relaxational or the resonant regime.

As noted before, the temperature of the minimum in $\delta\varepsilon'/\varepsilon'$ is defined by the point where the relaxational and resonant contribution to are equal. In the low frequency regime, where the crossover happens well within the one phonon dominated relaxation, we find

$$T_{\min} = 1.30 \sqrt[3]{\frac{2\pi\nu}{K_1 k_B^3}}. \tag{2.59}$$

As the temperature of the minima is easy to measure and intuitive to treat, we will use $T_{\min}(1\,\mathrm{kHz})$ rather than K_1 when discussing the strength of one phonon relaxation. At high frequencies, where the minimum is shifted into the temperature range of multi phonon relaxation, the minimum shifts with $T_{\min} \propto \nu^{1/7}$ and is visibly deformed with respect to lower frequencies. The onset of the multi phonon process as a steepening of the high temperature slopes for lower frequencies is again nicely visible. Since only the minimum of the 1 GHz curve is well within this regime and measurements at such high frequencies are less common than those at low frequencies, we will use K_2 rather than $T_{\min}(1\,\mathrm{GHz})$ as a parameter in the numeric calculations.

All numeric calculations performed in this thesis, if not specified differently, were performed with

$$T_{\min}(1\,\mathrm{kHz}) = 60\,\mathrm{mK} \qquad \text{and} \qquad K_2 = 25\,. \tag{2.60}$$

In order to discuss the curves, it is useful to determine the values of the slopes due to resonant and relaxational processes in both the one phonon and two phonon regime, that amount to

$$\delta\varepsilon'/\varepsilon'_{\mathrm{res}} = -\frac{2}{3}C_{\mathrm{d}} \ln\left(\frac{T}{T*}\right) \tag{2.61a}$$

$$\delta\varepsilon'/\varepsilon'_{\mathrm{rel}} = C_{\mathrm{d}} \ln\left(\frac{T}{T*}\right) \tag{2.61b}$$

$$\delta\varepsilon'/\varepsilon'_{\mathrm{rel}} = \frac{7}{3}C_{\mathrm{d}} \ln\left(\frac{T}{T*}\right) \tag{2.61c}$$

leading to slope ratios of $\delta\varepsilon'/\varepsilon'_{\mathrm{res}} : (\delta\varepsilon'/\varepsilon'_{\mathrm{res}} + \delta\varepsilon'/\varepsilon'_{\mathrm{rel}}) = -2 : 1$ and $-2 : 5$ respectively. The parameter $C_{\mathrm{d}} = \frac{p_0^2 P_0}{\varepsilon_0 \varepsilon_{\mathrm{r}}}$ is a material specific quantity, that already appeared in the equations (2.55) to (2.58). Again, as the density of two-level systems P_0 and the dominant dipole moment p_0 are not usually known, C_{d} is treated as a free parameter in the calculations and fits.

The frequency dependence of the total loss tangent $\tan(\delta)$ is shown in the right part of figure 2.15, where it is plotted for frequencies ranging from 1 Hz to 1 GHz. The high temperature part of the curves is again governed by relaxational processes. We see the common plateau at highest temperatures, as well as the $\nu^{1/3}$dependence of temperature where the slope has its turning point in the one phonon regime.
As there is hardly any overlap between the relaxational and the resonant regime in the loss tangent, we only see an effect in the 1 GHz curve, that does not go down to zero before rising again. The different height of the low and high temperature plateau is nicely visible now.
Similar calculations as for the real part lead to the values for the two plateaus and the rise of the loss tangent in the one phonon regime

$$\tan(\delta)_{\mathrm{res}} = \frac{\pi}{3}C_{\mathrm{d}} \tag{2.62a}$$

$$\tan(\delta)_{\mathrm{rel}} = \frac{\pi}{6}C_{\mathrm{d}} \tag{2.62b}$$

$$\tan(\delta)_{\mathrm{rel}} = \frac{\pi^4 k_{\mathrm{B}}^3}{36 K_1 \omega} C_{\mathrm{d}}\, T^3 \tag{2.62c}$$

Thus, the slopes in $\delta\varepsilon'/\varepsilon'$ and the plateaus and the rise in $\tan(\delta)$ allow cross-checking the validity of the standard tunneling model, especially the relative contributions of

resonant and relaxational mechanisms to the total signal. Additionally, measurements at different frequencies complement each other in the processes they are sensitive to and, by tracking the crossover temperature $T_{\min}$, permit a far more exact tracking of the one- and multi phonon dominated temperature regions than measurements at just one given frequency.
Broadband measurements of the dielectric properties of glasses over a temperature range from several millikelvin to about ten kelvin, as were performed in this thesis, therefore allow us to check both the interactions present in glasses and the distribution of the two-level systems and thereby the validity of the standard tunneling model [Leg13].

2.4 Extensions of the standard tunneling model

The standard tunneling model, as described above, describes many low temperature properties of amorphous solids very well. Especially for the dielectric properties however, it fails to accurately describe many details of the data.
Perhaps the most prominent shortcoming of the standard tunneling model lies in the description of the slope ratio in $\delta\varepsilon'/\varepsilon'$. It is, without the influence of multi phonon relaxation, predicted to be $-2:1$, but measured to be about $-1:1$ in very different glasses like vitreous silica [Fro77, vR98, Luc11], the multicomponent glass N-BK7 [Ens89, Rog97b] or in the multicomponent glass Albasi [Str98, Woh01a]. Similar observations were also made in elastic measurements [Rau95, Cla94, Cla00]. Also, the

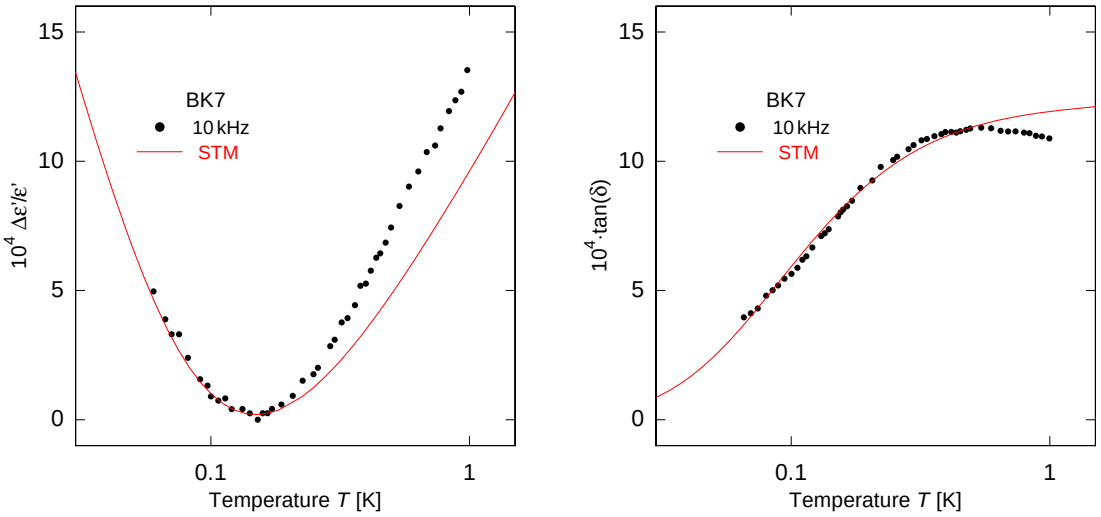

Figure 2.16: Change of the real part of the dielectric function $\delta\varepsilon'/\varepsilon'$ (left) and the loss tangent $\tan(\delta)$ (right) as a function of temperature at a frequency of 10 kHz and numeric calculations of the standard tunneling model. After [Ens89].

plateau in the dielectric loss tangent $\tan(\delta)$ is not flat but slopes off slightly towards higher temperatures. An example for a low frequency dielectric measurement on N-BK7 performed at 10 kHz is shown in figure 2.16. Both the slope ratio of $-1:1$ in the real part and the non-constant plateau of the loss tangent are clearly visible. At the same time, the standard tunneling model, that was adjusted to fit at the low temperature slope of the real part, describes the temperature dependence of the loss data well below the plateau regions.
Over the years, multiple extensions and modifications of the standard tunneling model have been proposed in order to accord for these differences. Most of the modifications can be grouped into two different approaches, that, while varying in their exact form, share a common influence on the predictions made by the standard tunneling model: The extended models either modify the distribution function by diminishing the density of states in a given parameter region [Bur95, Wür02, Bur06c, Bur14] or consider additional relaxational processes [Bur95, Tie92]. Sometimes, both modified distribution functions and additional relaxation processes are assumed at the same time.
The following section will give an overview over some of the most popular modifications of the standard tunneling model. As far as possible, these modifications were calculated numerically using equations (2.55) to (2.58) with appropriate changes to the parameter distribution and relaxation times.

2.4.1 Nonlinear excitation

Until now, we have only assumed linear responses of the system to the forces created by the dielectric field. This is only true if the electric fields strain is far smaller than the current temperature,

$$p_0 F \ll k_\mathrm{B} T\,, \tag{2.63}$$

whereas for larger external fields nonlinear effects are expected. As the above equation is harder and harder to fulfill when going towards lower temperatures with constant field strengths, this is where we expect nonlinear effects to show the strongest. While not changing the regime of linear response of the standard tunneling model, the consideration of nonlinear excitation will be very useful for the interpretation of the data and is therefore presented here.
In a model developed by Stockburger et al. [Sto95] for low frequency acoustic measurements as in [Esq92, Cla94], that was later applied to electric fields in [Rog97b], these nonlinear effects are calculated.
A larger strain, according to the model, causes a stronger resonant response of the system, increasing the low temperature slope of the real part of the dielectric function $\delta\varepsilon'/\varepsilon'$. As is shown in the left part of figure 2.17 the steepening of the curve also pushes the minimum towards higher temperatures. For intermediate strains we see

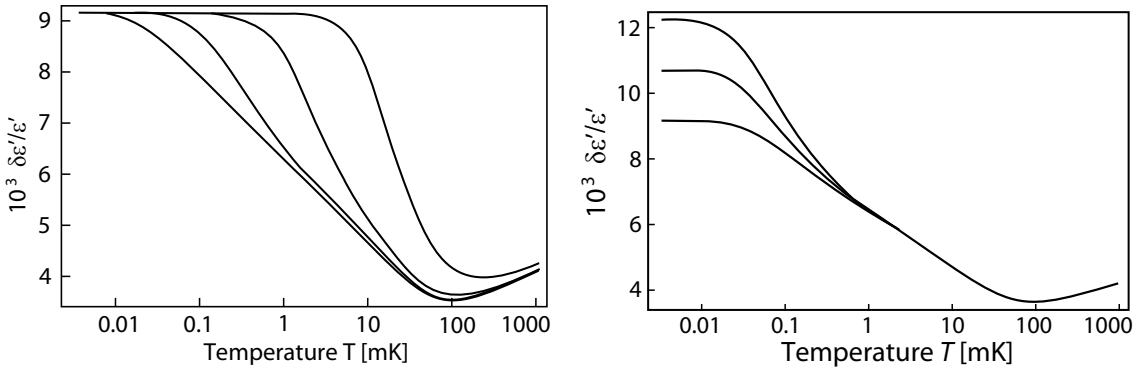

Figure 2.17: Change of the real part of the dielectric function $\delta\varepsilon'/\varepsilon'$ with drives of $p_0F/k_\mathrm{B} = 0.03$, 0.3, 3 and 30 mK (left) and the minimal tunneling splitting $\Delta_{0,\mathrm{min}}/k_\mathrm{B} = 10^{-4}$, 10^{-3} and 10^{-2} mK (right), both from bottom to top, as a function of temperature for a frequency of 500 Hz and N-BK7 material parameters. After [Rog97b].

a change of the slope beginning at temperatures of $p_0F = k_\mathrm{B}T$ and a further steepening towards lower temperatures. At the highest fields this happens in the vicinity of the minimum so that the slope is steep but constant. At lowest temperatures, the curve reaches a plateau that is determined by the minimal tunneling splitting $\Delta_{0,\mathrm{min}}$, as is shown in the right part of the figure.
The value of the plateau might help determine of the low temperature cutoff of the distribution function, that was treated in section 2.4.2.However, the values of $\Delta_{0,\mathrm{min}}$ shown here are much higher than expected in experiments and only serve to illustrate the effects of different minimal tunneling splittings.
Due to saturation effects, we expect a small decrease of the relaxational loss at low temperatures, but the effect is expected to be far smaller than that of strong fields on the real part of the dielectric function.

2.4.2 Cutoff of the distribution function

Restriction of the tunneling splitting Δ_0

The original flat distribution function of the standard tunneling model is given by equation (2.47). Instead of choosing an arbitrary small $\Delta_{0,\mathrm{min}}$, we can also use other types of cutoffs. Measurements of the specific heat of vitreous silica or the behavior of $\delta\varepsilon'/\varepsilon'$ in dielectric measurements towards lowest temperatures have led to the assumption of rather large $\Delta_{0,\mathrm{min}}$, lying within the range of several millikelvin [Str94, Las78, Mei96, Rog97b].
Instead of a simple cutoff at a fixed energy, we have chosen here a Gaussian gap in the distribution at lowest energies:

$$P(\Delta_0, E)\,\mathrm{d}\Delta_0\mathrm{d}E = P_\mathrm{STM}\,A\,\left(1 - a\,\exp\left(-\Delta_0^2/2(k_\mathrm{B}\delta T)^2\right)\right)\,\mathrm{d}\Delta_0\mathrm{d}E \qquad (2.64)$$

Here, a is the relative depth of the Gaussian ranging from 0 to 1 and δT the width of the curve, expressed as a temperature. In order to make the effect visible, a rather large δT =15 mK was chosen for the calculations. As for all following changes of the distribution function, the factor A allows for a normalization of the curves. The Gaussian gap allows a smoother decline of the distribution at smallest tunneling splitting and makes investigations on the influence of the gap's depth a possible.

The calculated curves for four different values of a and the original standard

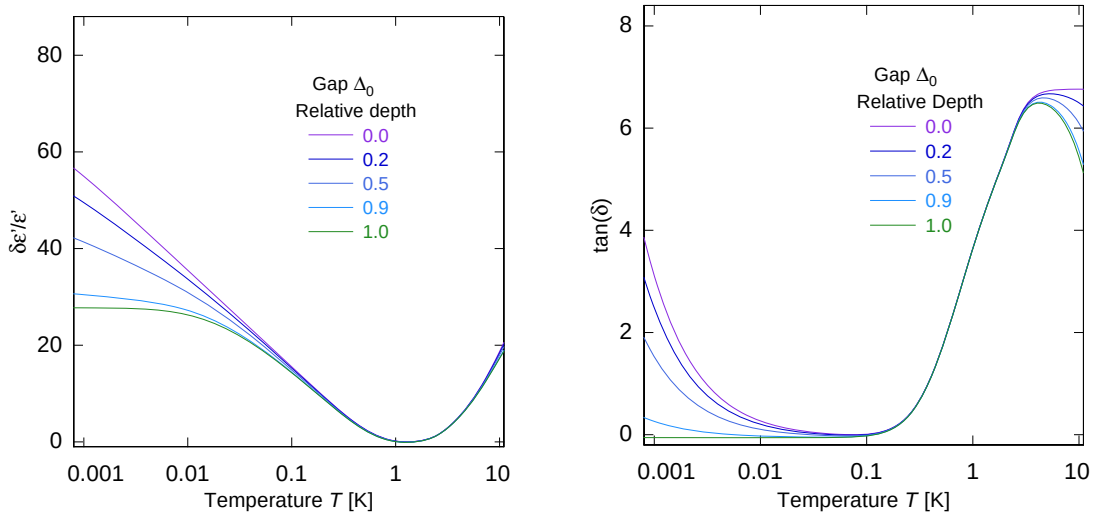

Figure 2.18: Change of the real part of the dielectric function $\delta\varepsilon'/\varepsilon'$ (left) and the loss tangent $\tan(\delta)$ (right) as a function of temperature at a frequency of 5 MHz and different values of the depth a of the modified distribution function as given by equation (2.73).

tunneling model distribution for comparison at a frequency of 5 MHz are plotted in figure 2.18.

The gap causes a decrease in the the low temperature slope of $\delta\varepsilon'/\varepsilon'$ towards lowest temperatures, instead of rising logarithmically. As the constant density of states is reflected by the constant rise of the low temperature branch of the curve, a gap in the density is visible immediately through such a decrease in the slope. The exact form of the gap shows in the temperature dependence of the slope, its depth in the slope at lowest temperatures. If the gap is not centered around zero, a plateau will form after which the signal will rise again.

The gap also affects the high temperature plateau in $\tan(\delta)$, which is not constant as in the flat distribution, but rises towards a maximum and then drops down again towards higher temperatures. The resonant contribution is also reduced, the effect of even a shallow gap with $a = 0.2$ being clearly visible, while the gap with $a = 1$ suppresses the signal completely.

The effect on measurements performed at different frequencies caused by a gap at smallest Δ_0 is shown in figure 2.19. A gap with $a = 0.5$ and the same width

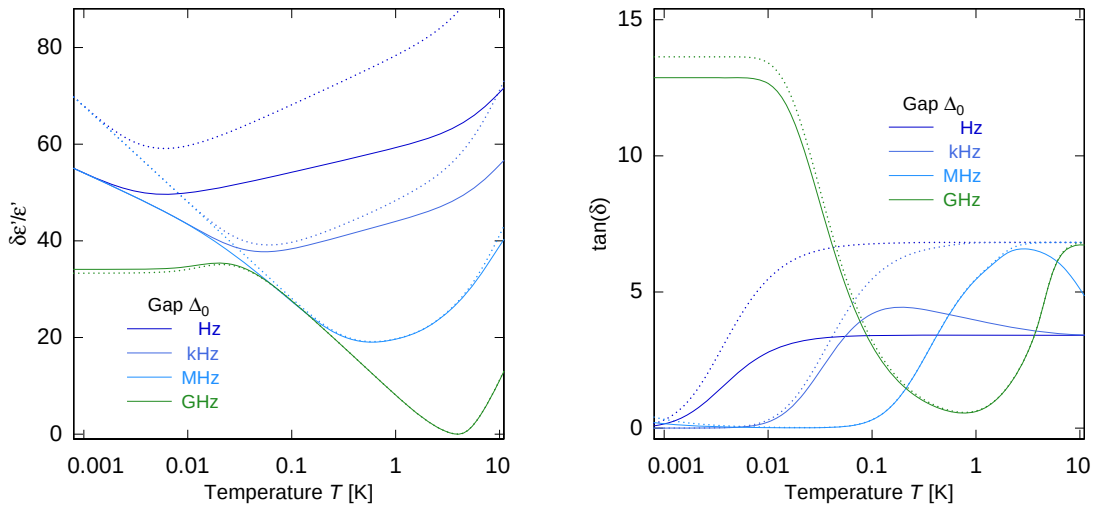

Figure 2.19: Change of the real part of the dielectric function $\delta\varepsilon'/\varepsilon'$ (left) and the loss tangent $\tan(\delta)$ (right) as a function of temperature for frequencies between 1 Hz and 1 GHz and with a modified distribution function as given by equation (2.64) with $a = 0.5$. Unmodified calculations of the standard tunneling model are shown as dotted lines.

δT =15 mK as before was chosen here.
In the real part $\delta\varepsilon'/\varepsilon'$, the effect of the gap has the same strength for all frequencies, causing the common resonant branch to flatten off. For low frequencies, this changes the slope ratio from $-2:1$ towards the smaller values observed in experiments. The plateau of the 1 GHz curve is, however, not affected.
The loss $\tan(\delta)$ shows a much larger frequency dependence on a gap in Δ_0. The plateau of the 1 GHz curve is slightly lowered and at lower frequencies the resonant loss is also strongly reduced, as expected. Most interesting, however, is the behavior of the relaxational part of the signal: At lowest frequencies, the curve rises as expected, but only reaches a plateau value of $a \cdot \pi/6\, A$, while the higher frequencies all go through a maximum and then drop down towards this lowered plateau value. The slope of this signal drop towards high temperatures and the height of the maximum is different for all values, destroying the common high temperature plateau region in $\tan(\delta)$.

Restriction of the tunneling parameter λ

As shown above, the restriction of the tunneling splitting either by a hard cutoff at $\Delta_{0,\min}$ or by a Gaussian function, leads to a steep temperature dependence of both the low temperature slope of $\delta\varepsilon'/\varepsilon'$ and the high temperature plateau region of $\tan(\delta)$. A less pronounced decline of the slopes can be achieved by not restricting Δ_0 directly, but rather the tunneling parameter λ.

A Gaussian distribution centered around zero has already been applied in [Ens89,

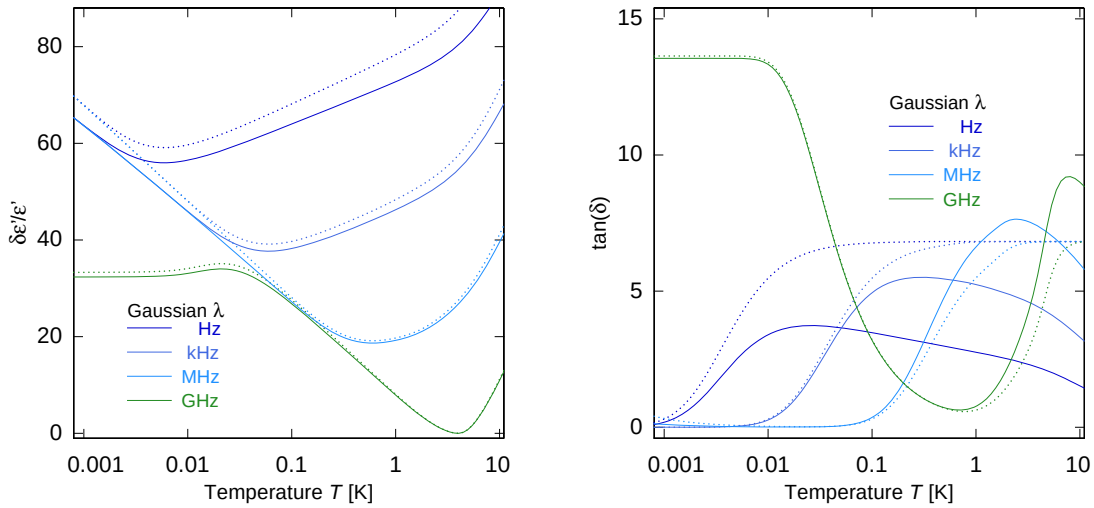

Figure 2.20: Change of the real part of the dielectric function $\delta\varepsilon'/\varepsilon'$ (left) and the loss tangent $\tan(\delta)$ (right) as a function of temperature for frequencies between 1 Hz and 1 GHz and with a modified distribution function as given by (2.65) with $\delta\lambda = 8$. Unmodified calculations of the standard tunneling model are shown as dotted lines.

Bec90], so a similar change of the distribution was chosen here:

$$P(\Delta_0, E)\,\mathrm{d}\Delta_0\mathrm{d}E = P_{\mathrm{STM}}\; A\; \exp\left(-\lambda(\Delta_0)^2/2(\delta\lambda)^2\right)\mathrm{d}\Delta_0\mathrm{d}E \tag{2.65}$$

The width of the Gaussian determined is by $\delta\lambda$. The smaller the chosen value, the steeper the cutoff, pushing the effects to lower temperatures and increasing their magnitude. For the numeric calculations shown in figure 2.20 a value of $\delta\lambda = 8$ was chosen.

The restriction of the distribution leads to a gradual flattening of the slope of $\delta\varepsilon'/\varepsilon'$ towards lowest temperatures, similar to that of the gap in Δ_0, changing the slope ratio from $-2:1$ closer to $-1:1$. The exact slope ratio depends on the width of the Gaussian chosen.

The bigger influence between a Gaussian distribution in λ and a direct cutoff in Δ_0 is seen in the loss tangent $\tan(\delta)$. The low temperature plateau is hardly affected here, while the high temperature plateau region is again temperature and frequency dependent.

As before, the smallest frequency reaches the lowest plateau value, but the highest frequencies reach maxima well above the former plateau value. We can even reach a factor of two between the maxima of the loss tangent of the lowest and highest frequencies, depending on the width of the Gaussian. The slope towards high temperatures is now linear in a semi logarithmic plot both in the one phonon and the two phonon regime, a crossover between the regimes is well visible via the change of the

slope at high temperatures. A linear decrease of the former plateau region towards higher temperatures in a semi logarithmic plot has been observed in measurements (see section 5.2), so a Gaussian distribution of the tunneling parameter can be seen as a good approximation of the distribution of two-level systems.

Variation of E and Δ

A slightly more flexible restriction of the distribution function has been given by Doussineau et al. [Dou80]. It allows for an individual variation of the three parameters Δ, Δ_0 and E:

$$P(\Delta_0, E)\,\mathrm{d}\Delta_0\mathrm{d}E = P_{\mathrm{STM}}\; A\,\frac{\Delta^{2\mu}E^{\,2\nu}}{\Delta_0^{2\gamma}}\,\mathrm{d}\Delta_0\mathrm{d}E \tag{2.66}$$

In principle, the new distribution can have any combination of the three parameters. If we, for example, set the three additional parameters to $\mu = \nu = \gamma = 0$, we recover the distribution given by the standard tunneling model.
As the distribution not only influences the dielectric function but also the thermal conductivity, we find $\kappa \propto T^{2-2(\mu+\nu-\gamma)} = T^{\,2}$ for many glasses, as was shown in section 2.2. We can therefore assume

$$\mu + \nu - \gamma = 0\;, \tag{2.67}$$

thereby fixing one parameter. Furthermore, results of β-alumina require $\gamma = 0$ [Dou80], a result which we will also use for the numeric calculations of dielectric glasses. We then find the more simple form

$$P(\Delta_0, E)\,\mathrm{d}\Delta_0\mathrm{d}E = P_{\mathrm{STM}}\; A\,\Delta^{2\mu}E^{-2\mu}\,\mathrm{d}\Delta_0\mathrm{d}E\;, \tag{2.68}$$

where μ is in this case assumed to be positive. The result of a calculation using $2\mu = 0.36$ is shown in figure 2.21. The low temperature branch of the real part of the dielectric function is again reduced by the new distribution function. While for the two former modifications the branch showed a flattening off towards lowest temperatures, no such bending is observed for the combined change of $\Delta^{2\mu}E^{-2\mu}$. The slope now shows a logarithmic rise, that is less steep than for the original flat distribution.
The changed slope ratio between the low and high temperature branch also shifts the minima of the curves slightly to lower temperatures, but does not change the principal $\nu^{1/3}$and $\nu^{1/7}$dependence of T_{min} in the one and two phonon regime.
The loss tangent is not changed but for the highest frequency. Here, where resonant loss has a large contribution to the total signal, we see its partial suppression by the modified distribution function. The relaxational contribution remains virtually

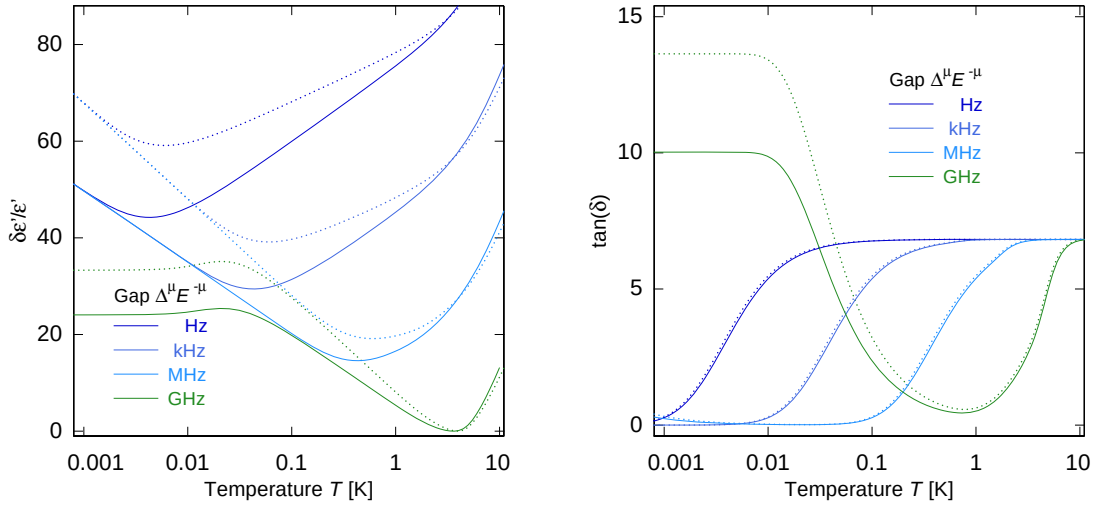

Figure 2.21: Change of the real part of the dielectric function $\delta\varepsilon'/\varepsilon'$ (left) and the loss tangent $\tan(\delta)$ (right) as a function of temperature for frequencies between 1 Hz and 1 GHz and with a modified distribution function as given by (2.68) with $2\mu = 0.36$. Unmodified calculations of the standard tunneling model are shown as dotted lines.

unchanged at all frequencies, the high temperature plateau region thus is still flat as with the unchanged distribution function.
While the modification of the distribution function by $\Delta^{2\mu}E^{-2\mu}$ is purely phenomenological, it allows for a very good fit of the predicted curves to the measured change of the real part of the dielectric function of glasses, that usually shows slope ratios closer to $-1 : 1$ than $-2 : 1$ in the one phonon regime. At the same time, the loss tangent remains unchanged in the high temperature plateau region, allowing for a good discrimination between this modification and other causes for the changed slope ratio that change the plateau region as well.

2.4.3 Long range interaction

The standard tunneling model assumes non-interacting tunneling systems down to lowest temperatures. There is, however, experimental evidence in microwave experiments that long range interactions between tunneling systems may set in at temperatures below 1 K [Arn75]. Recent experiments tracking single tunneling systems in the dielectrics of qubits, as described in [Gra12], have directly shown interaction [Lis15]. A theory for long range elastic and electric dipolar interaction leading to incoherent tunneling in crystals was investigated by [Wür95] and applied to glasses in [Ens97]. First considerations for a gap in the density of states due to long range interaction in semiconductors were made in [Efr75] and later translated to dielectric glasses. A very detailed theoretical description of such a long range electric dipole interaction

is given by [Bur95]. Its predictions on both a modified distribution function and an additional relaxation process will be given here.

Dipole gap in the distribution function

In the theory of long range dipole-dipole interaction, an additional contribution is added to the Hamiltonian (2.21), that couples two tunneling systems i and j

$$U = -\frac{1}{2} U_{ij} S_i^z S_j^z \ , \tag{2.69}$$

again using the Pauli matrices and a coupling constant U_{ij} that is set to be equal and isotropic for all two-level systems. The long range interaction then simply becomes

$$U_{ij} = \pm U_0 / R^3 \tag{2.70}$$

with R being the distance between tunneling systems and U_0 a constant defined by the type of long range interaction (usually strain or dipole mediated) considered.
The coupling of the two tunneling systems leads to an effective lowering of their total energy [Bar80]

$$E_{ij} = E_i + E_j - U_0 \tag{2.71}$$

and thereby to a decrease of low energy excitations and the formation of a pseudogap in the distribution function, called the *dipole gap*. The interaction is only significant, if the interaction strength is similar to or larger than the thermal energy of the sample:

$$U_0 > k_\mathrm{B} T \tag{2.72}$$

For a weak interaction, only the first order correction to the density of states needs to be taken into account. We then find instead of (2.47)

$$P(\Delta_0, E)\,\mathrm{d}\Delta_0 \mathrm{d}E = P_\mathrm{STM}\ A\ \left(1 - \frac{2\pi}{3} P_0 U_0 \log\left(\frac{W}{E + k_\mathrm{B}T}\right) \log\left(\frac{W}{\Delta_{0,\mathrm{min}}}\right)\right)\ \mathrm{d}\Delta_0 \mathrm{d}E \tag{2.73}$$

Here, W is the crossover energy between the tunneling regime and that of thermal excitations, usually found between 1 K and 10 K [Buc84], as we will discuss in section 2.4.5. It is set to 1 K for all calculations of this thesis. The limit of weak interactions is valid, as long as the correction much is smaller than the original value of the density of states. This original density of tunneling systems P_0 enters into the equation, as it sets the average distance between tunneling systems.
The nature of the long range interaction has not yet been specified. In any material, it can be mediated via strain that is applied, as is done in acoustic measurements. We then find

$$U_{0,\mathrm{a}} \propto C_\mathrm{a} = \frac{\gamma^2 P_0}{\rho v^2} \tag{2.74}$$

with γ being the coupling of tunneling systems to phonons and v the sound velocity, as in (2.50). The onset of the long range interaction is then linked to the onset of one phonon relaxation, however with a different dependence on the sound velocity v.
As most amorphous solids also contain electric dipoles, the dipole-dipole interaction must also be considered. In this case U_0 becomes

$$U_{0,\mathrm{d}} \propto C_\mathrm{d} = \frac{p_0^2 P_0}{\varepsilon_0 \varepsilon_\mathrm{r}} \tag{2.75}$$

and thus proportional to the square of the dipole moment p_0. The product $P_0 U_{0,\mathrm{d}}$ is then not only found in the modified density of states (2.73), but also as the prefactor in the measurement signals $\delta\varepsilon'/\varepsilon'$ and $\tan(\delta)$ as given in equations (2.55) to (2.58) [Nat98]. The same is true for the measurement signals in acoustic measurements, that are directly linked to $P_0 U_{0,\mathrm{a}}$.
By simply measuring the change of sound velocity $\delta v/v$ one can thus determine the strain mediated long range interaction $U_{0,\mathrm{a}}$. The dipole-dipole interaction strength $U_{0,\mathrm{d}}$ can only be determined up to a factor $f < 1$, as usually not every tunneling system possesses a dipole moment.
Knowing the usual values for $\delta\varepsilon'/\varepsilon'$ and $\tan(\delta)$, we immediately find, that $P_0 U_0$ should be in the range of $10^{-4} - 10^{-2}$. Figure 2.22 shows the calculated temperature dependence of dielectric measurements for different frequencies between 1 Hz and 1 GHz using a value of $C_\mathrm{d} = 1.51 \times 10^{-3}$, that was found for N-BK7 in [Nat98]. Again, all the other parameters were chosen the same as for the calculations of the standard tunneling model.

Due to the suppression of the contribution by tunneling systems with small energy splittings, the low temperature branch of $\delta\varepsilon'/\varepsilon'$ is less steep than that of the unmodified standard tunneling model and flattens of slightly towards lowest temperatures. The effect becomes more and more pronounced, as the gap in the distribution becomes larger with smaller temperatures. This modifies the slope ratio in the one phonon regime closer to a value of $-1:1$ rather than $-2:1$, as the high temperature branch is hardly affected by the gap at low temperatures. The effect is very similar to that of the already introduced restrictions in either Δ_0 or λ.
The loss tangent $\tan(\delta)$ also shows distinct differences to both the unaltered standard tunneling model and the previous modifications. The resonant contribution to the loss is reduced due to the gap in low energy tunneling systems, which is well visible in the 1 GHz curve. The most prominent difference though is the rise of the plateau region at higher temperatures. Rather than reaching a constant value, the loss rises logarithmically with temperature. It even surpasses the original plateau value. This rise of the plateau region is a feature shows again, that the high temperature plateau of the loss tangent allows for a good discrimination between different modifications

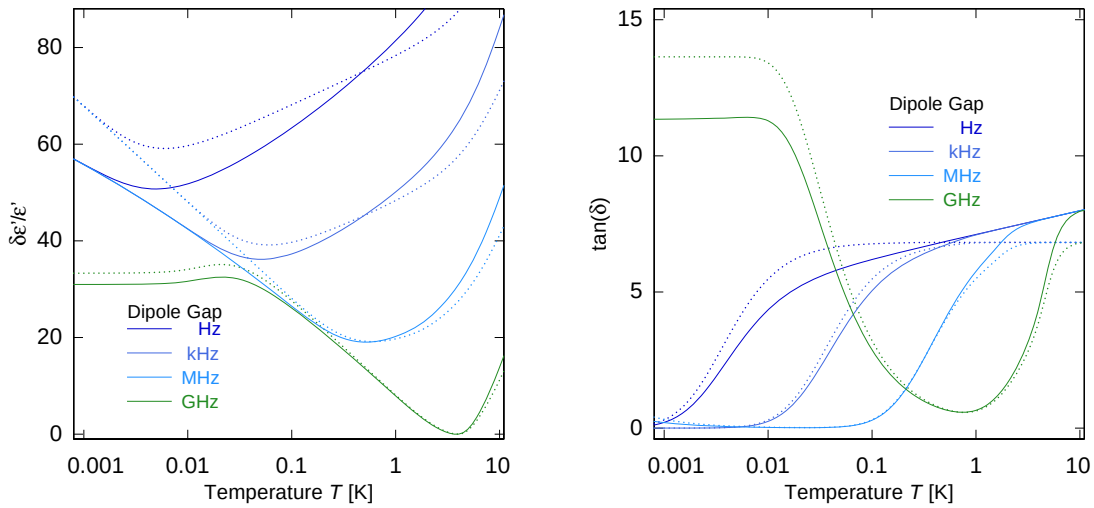

Figure 2.22: Change of the real part of the dielectric function $\delta\varepsilon'/\varepsilon'$ (left) and the loss tangent $\tan(\delta)$ (right) as a function of temperature for frequencies between 1 Hz and 1 GHz and with a modified distribution function due to long range interaction, as given by equation (2.73). Unmodified calculations of the standard tunneling model are shown as dotted lines.

of the standard tunneling model.
Another example of a modified distribution function leading to similar results is given in [Bur14], where a more simple, phenomenological modification of the distribution has been chosen:

$$P(\Delta_0, E)\,\mathrm{d}\Delta_0\mathrm{d}E = P_{\mathrm{STM}}\; A\; (1+\mu)\ln\left(\frac{\Delta_{0,\min}}{E_{\max}}\right)\left(\frac{\Delta}{E_{\max}}\right)^{\mu}\mathrm{d}\Delta_0\mathrm{d}E \tag{2.76}$$

Indeed, the modification is very similar to that of Doussineau et al. in equation (2.68) with $\nu = \gamma = 0$. In order to best fit the $1/f$ noise of a superconducting resonator, a value for the interaction strength of $\mu = 0.36$ was determined by the authors of the paper. Since we would like to compare this model to the dipole gap, we use a value of $\mu = 0.1$, as the effects of the two modifications are then far more comparable.

As shown in figure 2.23, we find that the phenomenological ansatz is indistinguishable from the dipole-dipole interaction model in its effect on the dielectric function. The very small differences between the calculations stem from choosing P_0U_0 and μ. The dipole model couples the interaction strength to the total signal, though, and also makes predictions about interaction driven relaxation, that will be discussed below. In this way a more extensive analysis of data can be performed using the dipole-dipole interaction model, while choosing the simple interaction model of (2.76) can give easily calculable fast results.

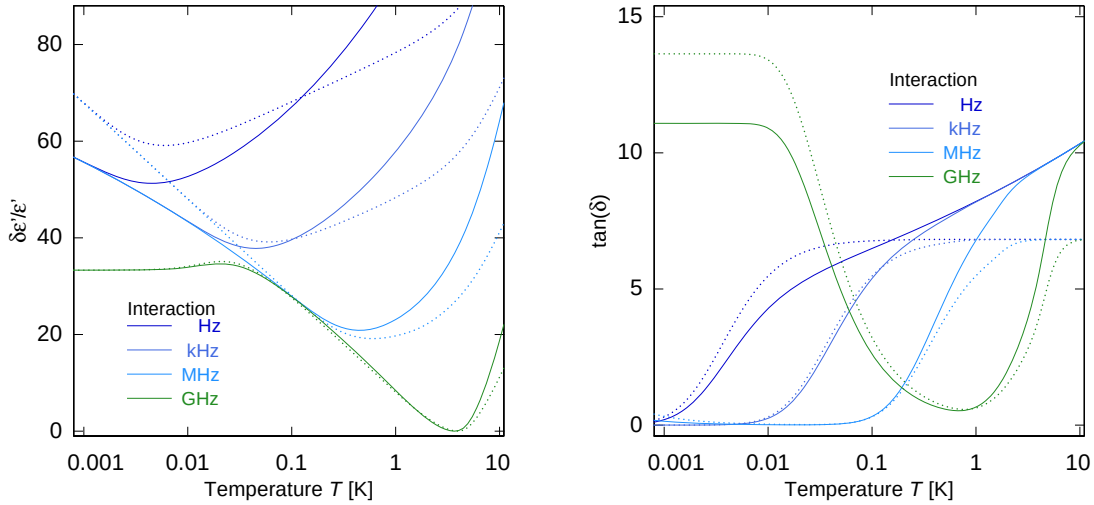

Figure 2.23: Change of the real part of the dielectric function $\delta\varepsilon'/\varepsilon'$ (left) and the loss tangent $\tan(\delta)$ (right) as a function of temperature for frequencies between 1 Hz and 1 GHz and with a modified distribution function due to long range interaction, as given by equation (2.76). Unmodified calculations of the standard tunneling model are shown as dotted lines.

Interaction driven relaxation

Two tunneling systems coupled by the long range interaction discussed above can effectively form a new two-level system. If one system is in its ground and the other in the excited state, they form a so called *flip flop state* [Bur95]. This state has a new effective asymmetry energy

$$\Delta_p = E_1 - E_2 \tag{2.77}$$

given by the difference of the level splittings in the two tunneling systems and a tunneling splitting

$$\Delta_{0p} = \frac{U_{12}\Delta_{01}\Delta_{02}}{2E_1E_2} \ . \tag{2.78}$$

The interaction strength U_{12} thus determines the properties of the paired tunneling systems. A stable pair can only form while none of the two interacting tunneling systems is subject to phononic relaxation which would destroy coherence. Interaction driven tunneling will thus become more important towards lowest temperatures where phononic relaxation dies out and the effective radius and lifetime of coherent pairs becomes larger. Combining this, one finds the interaction relaxation rate

$$\tau_{\mathrm{int}}^{-1} = 10\,\frac{k_{\mathrm{B}}T}{\hbar}\left(\frac{\Delta_0}{E}\right)^2 (P_0U_0)^3 \ . \tag{2.79}$$

The rate depends linearly on temperature and has a cubic dependence on the interaction P_0U_0. The strength of the long range interaction therefore strongly influences

the onset of the interaction driven regime. A similar calculation has been made for the case of long range elastic coupling leading to decoherence, yielding also a T-dependent relaxation rate [Wür95, Ens97, Bod06].

In figure 2.24, the influence of the interaction driven relaxation on the complex

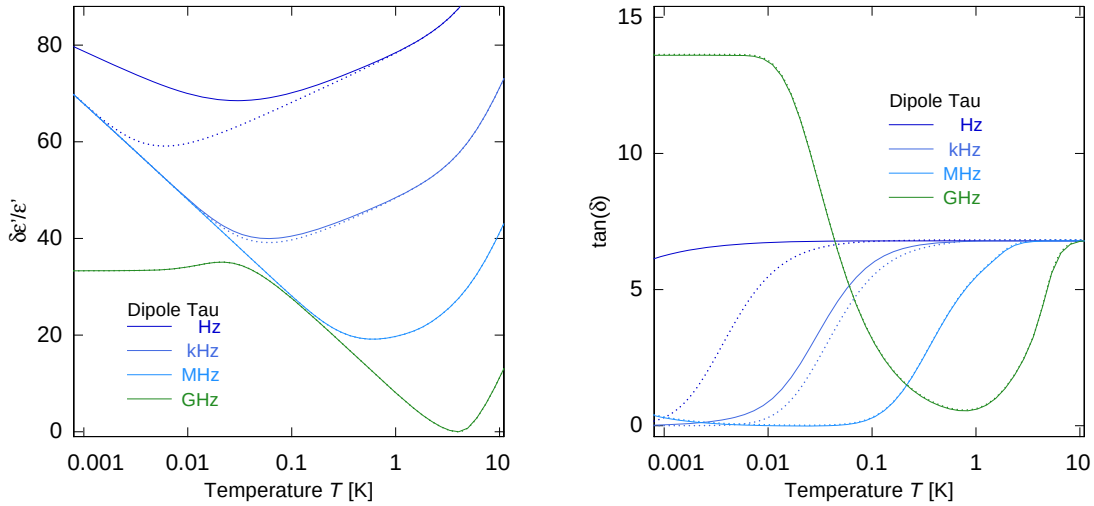

Figure 2.24: Change of the real part of the dielectric function $\delta\varepsilon'/\varepsilon'$ (left) and the loss tangent $\tan(\delta)$ (right) as a function of temperature for frequencies between 1 Hz and 1 GHz and with interaction driven relaxation given by (2.79). Unmodified calculations of the standard tunneling model are shown as dotted lines.

dielectric function is shown. A larger interaction strength $P_0U_0 = 4.7 \cdot 10^{-3}$ than for the dipole gap was chosen in order to shift the onset of the interaction to higher temperatures.

Both in $\delta\varepsilon'/\varepsilon'$ and in $\tan(\delta)$, the influence is only visible at low temperatures and frequencies. The minimum of $\delta\varepsilon'/\varepsilon'$ at 1 Hz is shifted to higher temperatures and it is flattened off, the 1 kHz is barely and the higher frequencies are not at all influenced, even at the high interaction strengths that has been chosen here. The same picture shows in the loss: at lowest frequencies it remains at the plateau value, almost to lowest temperatures. The 1 kHz shows a contribution of the T dependence, shifting the original T^3 flank a little, while again the highest frequencies are not touched.

2.4.4 Short dephasing times

Within the framework of the standard tunneling model, a possible influence of the spin spin dephasing time τ_2 on the dielectric function is usually neglected. This dephasing time is, at least for two-level systems, limited by the spin lattice relaxation time τ_1. Both τ_1 and τ_2 will increase towards lowest temperatures, reaching values of several hundred and about ten microseconds at 7.5 mK in N-BK7 respectively

[Fic12].
In numeric calculations of the standard tunneling model, no influence of τ_2 on the dielectric function was found, for $\tau_2 > 10^{-7}s$, as then for all temperatures and frequencies the relation $k_B T \leq \omega\tau_2$ holds true. At smaller dephasing times, however, a significant influence can be observed, as is shown in figure 2.25.

Here, a constant transverse dephasing time $\tau_2 = 3 \times 10^{-9}$ s was assumed. While a nonzero temperature dependency is of course a more realistic assumption, this very basic modification gives a first intuition as to what short influence short dephasing times could have on the dielectric function. Contrary to other modifications of the model, the short transverse dephasing time purely affects the resonant signal. The low temperature branch of $\delta\varepsilon'/\varepsilon'$ flattens off below about 100 mK, while the high temperature part remains the same as for larger dephasing times, as for high temperatures the resonant interaction will not be affected by the small τ_2 any more. The high temperature plateau in $\tan(\delta)$ also remains unchanged and only the low temperature plateau is slightly reduced.

Measurements of the phasing time τ_2 can be made in two pulse polarization echoes,

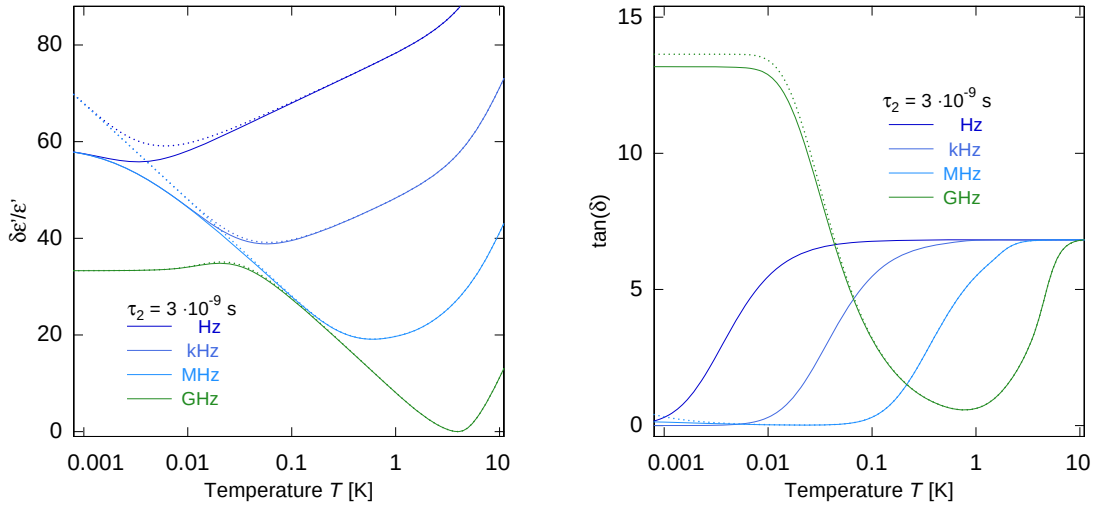

Figure 2.25: Change of the real part of the dielectric function $\delta\varepsilon'/\varepsilon'$ (left) and the loss tangent $\tan(\delta)$ (right) as a function of temperature for frequencies between 1 Hz and 1 GHz and with a very dephasing time $\tau_2 = 3 \times 10^{-9}$ s. Unmodified calculations of the standard tunneling model are shown as dotted lines.

where a very short dephasing time would lead to a strongly reduced echo amplitude in the experimentally accessible range beginning at about one micro second. In N-BK7 and similar glasses, where the echo amplitude is large after this timescale, the effect of strongly reduced transverse relaxation times does not have to be taken into account. However, if there were some glasses showing additional relaxational

processes down to lowest temperatures, both τ_1 and τ_2 might be significantly smaller and the reduced transverse relaxation time would have to be considered.

2.4.5 Incoherent tunneling and thermally activated processes

The standard tunneling model in its most strict form is only assumed to be valid for temperatures below a few kelvin. At higher temperatures, the tunneling systems will no longer tunnel coherently and thermal activation eventually becomes relevant, so that the approximation of two-level tunneling systems is no longer applicable. As the measurements performed in this thesis cover temperatures up to about ten kelvin, we will shortly discuss incoherent tunneling and thermal activation. The considerations will give us indications, as to when the assumption of coherently tunneling two-level tunneling systems should still be valid.

At lowest temperatures, the two-level tunneling systems show coherent tunneling due to slow relaxation rates. As these rates strongly increase towards higher temperatures, the thermal bath will destroy the coherence of the tunneling systems, leading to incoherent tunneling. This was considered using mode coupling theory in [Wür97]. The crossover to incoherent tunneling leads to additional relaxational processes not weighed by $(\Delta_0/E)^2$. Such relaxational processes lead both to a steepening of the real part of the dielectric function and to an increase of the loss tangent at the crossover temperature.
At even higher temperatures than the regime of incoherent tunneling, thermal activation of the two-level systems becomes the dominating process. If the thermal energy of the particle is sufficiently high, the barrier between the two wells of the double well potential can be overcome. The particle can then move classically between the two wells with the rate

$$\tau_{\mathrm{th}}^{-1} = \tau_0^{-1} \cosh\left(\frac{\Delta}{2k_{\mathrm{B}}T}\right) \exp\left(\frac{-V}{k_{\mathrm{B}}T}\right), \tag{2.80}$$

where τ_0^{-1} is directly proportional to the vibrational frequency of the well $h\nu_0 = 2E_0$ and V is the height of the tunneling barrier [Tie92]. If the potential is assumed to be purely quadratic and the mass of the tunneling particles to be constant, then we find the approximation

$$V = \lambda E_0 \,. \tag{2.81}$$

This is strictly true only for large tunneling parameters λ, so for a small overlap of the two wells. As the parameters are assumed to be very broadly distributed, we can still use this approximation to calculate effects of thermal activation on the two-level systems.

An even more simplified version of the thermal relaxation rate is given as

$$\tau_{\mathrm{th}}^{-1} = \tau_0^{-1} \exp\left(\frac{-V}{k_{\mathrm{B}}T}\right), \tag{2.82}$$

leaving out the dependence on the systems asymmetry [Rau95]. Again, as we integrate over all systems, this simplification will change the quantitative but not the qualitative effects of thermal activation with given parameters.
We have used the values given in [Tie92] of $E_0/k_{\mathrm{B}} = 12\,\mathrm{K}$ and $\tau_0 = 5 \times 10^{-13}\,\mathrm{s}$ to make the numerical calculations shown in figure 2.26.

Both in the real part of the dielectric function and the loss, the influence of the

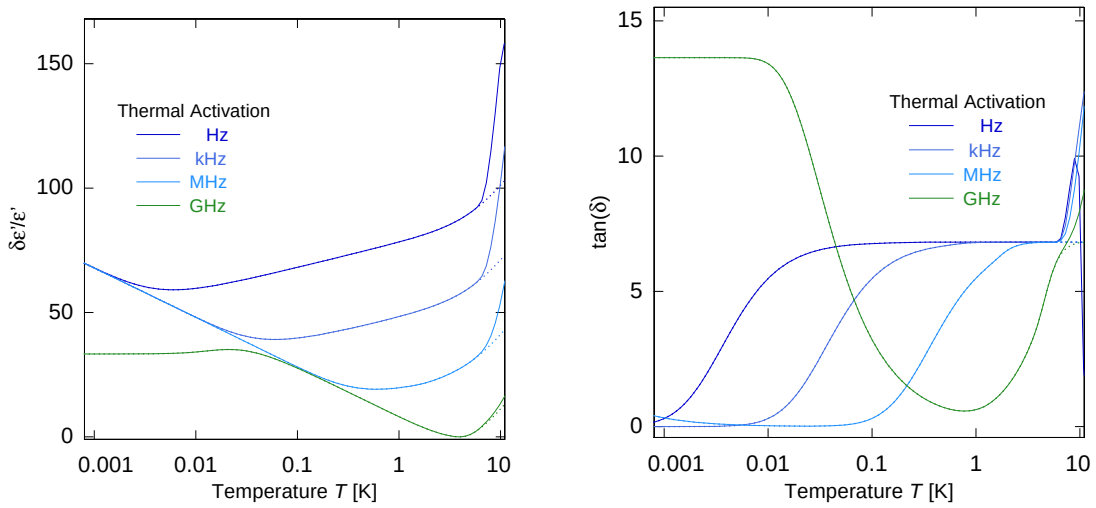

Figure 2.26: Change of the real part of the dielectric function $\delta\varepsilon'/\varepsilon'$ (left) and the loss tangent $\tan(\delta)$ (right) as a function of temperature for frequencies between 1 Hz and 1 GHz including relaxation due to thermal activation. Unmodified calculations of the standard tunneling model are shown as dotted lines.

thermal activation is seen at all frequencies, at temperatures above about 6 K. In $\delta\varepsilon'/\varepsilon'$, we see a very steep rise of the curves, much steeper than the two phonon relaxation. While the onset of two phonon relaxation is only temperature and not frequency dependent, we see a small but definite influence of the measurement frequency on the onset of thermal relaxation.
While the steep rise of $\delta\varepsilon'/\varepsilon'$ at high temperatures could also be due to another coherent relaxation process, the behavior of the loss tangent at high temperatures shows the difference between coherent tunneling and thermal activation. A coherent relaxation, scaled with $(\Delta_0/E)^2$, will not change the plateau region. Thermal relaxation, however, leads to a steep rise of $\tan(\delta)$ towards high temperatures. The signal then drops down after a sharp maximum, going to zero at higher temperatures. The onset of this effect is seen in the 1 Hz curve, but shifted to higher temperatures for

the other frequencies.

As mentioned above, the tunneling barriers found when fitting thermal excitation to dielectric data can easily be of the order of 10 K. This suggests that the model is a phenomenological description of the real processes in the temperature range above several kelvin, rather than a microscopic description [Wür97].
Both incoherent tunneling and thermally activated relaxation at high temperatures will significantly influence the dielectric properties of glasses. As the effects both lead to a rather drastic increase of the loss tangent, we can assume the effects of incoherent tunneling and thermal activation to be unimportant as long the plateau of the loss tangent is still flat.

2.4.6 The soft potential model

Until now, we have only considered double well potentials. A more general form was introduced in the soft potential model, which was developed in [Kar83] in order to explain thermal properties of glasses above a few kelvin, where they deviate from the standard tunneling model. Here, instead of a double well potential of two harmonic wells, a potential of the form

$$V(x) = E_0 \left(\eta \left(\frac{x}{a} \right)^2 + \xi \left(\frac{x}{a} \right)^3 + \left(\frac{x}{a} \right)^4 \right) \tag{2.83}$$

is assumed, where E_0 is the binding energy of the potential, x is the generalized coordinate, a is a length of the order of inter-atomic spacing and η and ξ are dimensionless, small parameters. Due to the disorder of the system, η and ξ are assumed random, but in the limit of soft potentials their absolute values are much smaller than one.
For small temperatures $T < 1\,\mathrm{K}$, the soft potential model effectively becomes the standard tunneling model, while at higher temperatures the quasi harmonic oscillators included in the model through $\eta > 0$ become important. They dominate the specific heat and thermal conductivity [Par93, Buc92].
The dielectric properties of a glass can again be influenced in two ways: at temperatures above one kelvin we eventually find the onset of thermal excitation, that is similar to the one described above and will lead to a rise of the loss tangent $\tan(\delta)$ and the real part $\delta\varepsilon'/\varepsilon'$ of the dielectric function. The density of states can also be enlarged at temperatures of about 10 K, as the higher energy levels of the quasi harmonic oscillators will also contribute and we no longer only have the distribution of two-level systems in the tunneling systems. This will lead both to a rise of the loss tangent $\tan(\delta)$ and the real part $\delta\varepsilon'/\varepsilon'$ at higher temperatures.

3. Nuclear Moments in Dielectric Glasses

The main focus of this thesis is the possible influence of large nuclear electric quadrupoles on the dielectric properties of glasses. We will therefore give a short overview over the findings leading to the discovery of the influence of nuclear quadrupoles on the properties of glasses at very low temperatures. This will be followed by an introduction to nuclear quadrupole resonance (NQR) and the relevant energy and frequency ranges found in glasses containing elements that carry nuclear quadrupole moments. Finally, we will present the theoretical models developed to predict the influence of the nuclear quadrupole moments on the dielectric properties of glasses.

3.1 Magnetic field effects in non magnetic glasses

Within the framework of the standard tunneling model, we do not expect any influence of magnetic fields on the dielectric properties of glasses. Indeed, it has been suggested to use the low temperature slope of low frequency measurements of the dielectric constant as a magnetic field resistant thermometers at very low temperatures. Such thermometers showed no notable sensitivity to magnetic fields up to 9 T [Wie87] or even 20 T [Pen95]. The first observations of a linear magnetic field dependence of the dielectric function on external magnetic fields in the millitesla range, observed in [Str98], therefore came as a big surprise. Further measurements

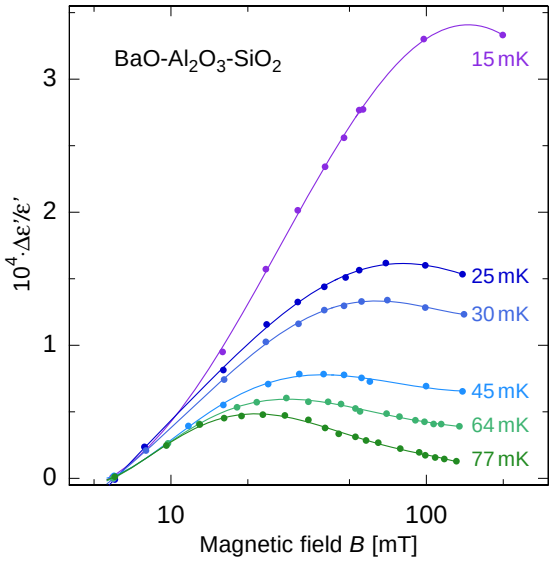

Figure 3.1: Magnetic field effect on $\Delta\varepsilon'/\varepsilon'$ in Albasi at different temperatures and small magnetic fields [Str00].

showed even larger effects: as shown in figure 3.1, even at small fields a very notable magnetic field effect is observed in the multicomponent glass BaO-Al_2O_3-SiO_2, in short Albasi. At higher fields the dependence of the dielectric function on the magnetic field becomes non monotonous [Str00, Woh01b, Hau02, Pol09]. The change of $\Delta\varepsilon'/\varepsilon'$ can become as big as 20% of the total signal at small temperatures.

In order to explain this unexpected behavior, the tunneling of particles in three dimensional wells was suggested [Ket99, Str00]. These so called Mexican hat potentials, that enclose a finite area and thus enable an Aharanov Bohm effect, would lead to a periodic variation of the dielectric function with an external magnetic field. It should be noted though, that for a single tunneling particle, the first maximum of the signal would be reached at fileds of the order of 1×10^5 T, while in experiments it is observed at a few millitesla. As the magnetic field dependence of the maximum scales inversely with the number of charge carrying particles in one tunneling system, this would mean that the relevant tunneling systems causing the magnetic field effect would have to consist of very large ensembles of tunneling atoms.

Subsequent dielectric polarization experiments allowed a further investigation

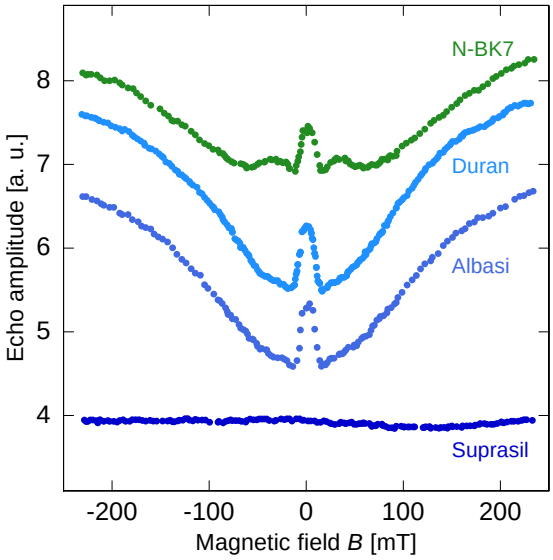

Figure 3.2: Magnetic field effect on the amplitude of two pulse dielectric polarization echoes of different dielectric glasses at 12 mK and 1 GHz with a separation time of $t_{12} = 1.7\,\mu s$ for Duran and $t_{12} = 2\,\mu s$ otherwise. Data from [Lud03]

of the effects of magnetic fields on glasses. First magnetic field dependence effects were discovered in Albasi [Lud02], where the amplitude of the echo depends strongly on an applied magnetic field, while the echo decay remains largely the same as in zero field. Further measurements revealed similar magnetic field dependencies in a variety of multicomponent glasses such as N-BK7 or Duran, while the quartz glass Suprasil showed no notable field dependence [Lud03], as is shown in figure 3.2. The data shows a strongly increased echo amplitude at high fields, indicating a stronger

coherence. The exact shape of the curve depends both on the temperature of the sample and the separation time t_{12} of the pulses.

A three dimensional potential is not the only cause that could lead to the observed magnetic field dependence, as it is known that the level splitting due to nuclear electric quadrupoles depends on external magnetic fields. It was therefore suggested by Würger et al. , that this could be the cause for the observed magnetic field dependence of the echo amplitude [Wür02]. As will be discussed in more detail in section 3.2, the coupling of a nucleus carrying and electric quadrupole moment to a local field gradient causes a characteristic splitting into sublevels.

As shown schematically in figure 3.3, the electric field gradients in the two wells of

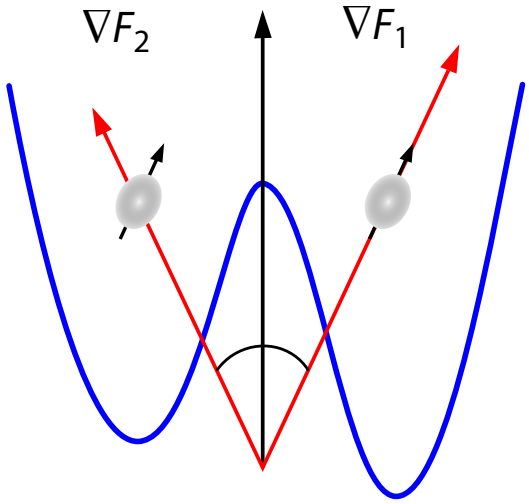

Figure 3.3: Double well potential with a tunneling particle carrying a nuclear quadrupole moment. The electric field gradients differ in the two wells, leading to additional energy splittings.

a double well potential will in general neither point in the same direction nor have the same strength. If an unperturbed tunneling particle is located mainly in well one, its spin and thereby its quadrupole quantization axis will align with the local field gradient. When the particle tunnels to well two, the spin quantization axis will no longer be aligned with the local field gradient. The coordinate and nuclear spin contribution to the systems Hamiltonian therefore will no longer diagonalize simultaneously, leading to a splitting of the former levels into partly degenerate sublevels.

3.2 Nuclear quadrupole resonance

Nuclei with a spin $I \geq 1$ posses a nuclear electric quadrupole moment. As these nuclei are non-spherical, they can couple to local electric field gradients. By measuring this coupling, one can infer details of the local charge distribution, thus making a detailed analysis of bonding lengths and angles in both crystalline and disordered solids possible. Overviews are given in, for example, [Smi71, Vog92, Sui06].
On the other hand, the level splittings caused by nuclear quadrupole interaction are in the order of several hundred kHz to MHz and therefore accessible in the low temperature range below 10 K, that is discussed in this thesis. .

In a deformed nucleus, the quadrupole moment Q of the charge distribution is defined by

$$eQ = \int \rho_n (3z_n^2 - r_n^2)\, \mathrm{d}r^3 \tag{3.1}$$

where ρ_n is the nuclear charge density in a volume $\mathrm{d}r^3$, z_n is the axis of symmetry concerning the nuclear spin and r_n the radius of the nucleus.

If a nucleus is spherical, Q will vanish as $z_n = r_n$. In oblate or prolate nuclei,

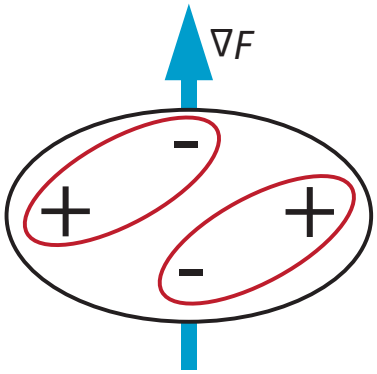

Figure 3.4: Schematic drawing of an oblate nucleus aligned along an electric field gradient. The two anti aligned dipoles that precess around the local electric field are drawn in red.

however, the resulting quadrupole moment will be a negative or positive area respectively, usually given in barn.

In a classical picture, the deformed nucleus effectively contains two anti-aligned dipoles, as shown schematically in figure 3.4. It will thus not be affected by constant electric field as all forces will cancel out. An electric field gradient, however, will exert different torques on both dipoles and thereby a net torque will lead to a precession of the nucleus around the electric field. The nuclear quadrupole resonance is then just the difference between the two Larmor frequencies of the dipoles.
The local electric field gradient at the nucleus $\nabla\mathbf{F}$ can also be written as the second

derivatives of the local electrostatic potential V:

$$\nabla \mathbf{F} = V_{ij} \frac{\partial^2 V}{\partial r_i \partial r j} = V_{xx} + V_{yy} + V_{zz} \tag{3.2}$$

Defining the principal axes in a way that $|V_{xx}| \leq |V_{yy}| \leq |V_{zz}|$, we can further define

$$V_{zz} := eq \tag{3.3}$$

and

$$\eta := \frac{V_{xx} - V_{yy}}{V_{zz}} \ . \tag{3.4}$$

The field gradient along the z-axis eq defines the direction of the nuclear spin in the case of a symmetrical potential, where the asymmetry parameter η equals zero.
In this symmetric case, the Hamiltonian of the system can be diagonalized using the nuclear spin along the z-axis I_z and the magnetic quantum number m. We can then define the quadrupolar coupling constant C_Q and the corresponding frequency ν_Q derived from the energy eigenvalues of the system:

$$C_Q = \frac{e^2 q Q}{h} \tag{3.5}$$

$$\nu_Q = \frac{3\, e^2 q Q}{4I(2I+1)h} = \frac{3\, C_Q}{4I(2I+1)} \tag{3.6}$$

The frequency ν_Q sets the scale of the transition frequencies of nuclei that can be excited and measured. With the usual selection rules $\Delta m = 0, \pm 1$, the resulting transition frequencies are

$$\nu_{m,m\pm1} = \nu_Q \, |(2m \pm 1)| \ \text{ with } |\mathrm{m}|, |\mathrm{m} \pm 1| \leq \mathrm{I} \ . \tag{3.7}$$

If the local field gradient is not symmetric, $\eta \neq 0$, the resulting transition frequencies need to be modified. In the case of $I = 3/2$ we find

$$\nu = \frac{e^2 q Q}{h} \left(1 + \frac{\eta^2}{3}\right)^{1/2} \ , \tag{3.8}$$

giving effective frequencies elevated by up to 15% for $\eta = 1$. For higher nuclear spins, the influence of the asymmetry parameter can not be calculated analytically any more. The resulting frequencies, however, always lie between the highest and lowest possible frequency thats occur at $\eta = 0$.

As a well ordered atomic lattice in a crystal provides very well-defined field gradients, the transition frequencies one can measure with NQR are very sharp. The disordered structure of glasses on the other hand leads to great variations in both bond lengths

Isotope	Nuclear Spin I	Quadrupole moment Q [barn]	Coupling constant C_Q [kHz]	Quadrupole frequency ν_Q [kHz]	Measured material
^{2}H	1	+0.003	165	124	^{2}HC in Glycerol [a]
^{11}B	3/2	+0.04	300	150	BO_4 in Glass [b]
^{11}B	3/2	+0.04	$2.2 - 2.65 \cdot 10^3$	$1.1 - 1.3 \cdot 10^3$	BO_3 in Glass [b]
^{17}O	5/2	-0.26	$2.35 - 5.0 \cdot 10^3$	$350 - 700$	Glass [c]
^{23}Na	3/2	+0.10	$1.8 \cdot 10^3$	900	Glass [d]
^{27}Al	5/2	+0.15	$3.5 - 4.5 \cdot 10^3$	$530 - 680$	Glass [b]
^{39}K	3/2	+0.05	$1.7 \cdot 10^3$	840	Crystal [e]
^{91}Zr	5/2	-0.2	$20.5 \cdot 10^3$	$3 \cdot 10^3$	$ZrSiO_4$ Crystal [f]
^{137}Ba	3/2	+0.24	$7 - 25 \cdot 10^3$	$3.5 - 12.5 \cdot 10^3$	Crystals [g]
^{165}Ho	7/2	+3.5	$360 \cdot 10^3$	$27 \cdot 10^3$	$Ho(OH)_3$ [h]
^{181}Ta	7/2	+3.3	$470 - 590 \cdot 10^3$	$33 - 42 \cdot 10^3$	OH in metal [i]

Table 3.1: List of cations and their quadrupolar coupling constants and frequencies commonly found in glasses. Data taken from a [Sch92] b [Pra06] c [Mae96] d [Xue93] e [Bas91] f [Bas90] g[Ham10] h [Bun85] i [Pei83], wherever possible data measured in glasses was used. Nuclear Quadrupole moments from [Sto05].

and angles and thereby in η, and sometimes even to varying coordination numbers of cations, changing C_Q. This smears out the observed frequencies, which is best seen in the difference between BO_3 and BO_4 rings given in table 3.1. Measurements performed on vitreous and crystalline borates show a broadening of the NQR frequencies in the glassy state for given local chemical composition [Bra99], but the values given in the table give a good indication of the transition frequencies present in glasses.

The quadrupole frequency ν_Q given in table 3.1 needs to be modified according to (3.8) for $I = 3/2$, bringing the measured frequencies close to C_Q. The possible harmonics of 4 or even 6 times ν_Q for $I = 5/2$ and 7/2 respectively at $\eta = 0$ bring the observed frequencies up even higher.

The overview in the table shows, that relevant nuclei for the glasses investigated in this thesis lead to quadrupole frequencies ranging from about 100 kHz in the case of ^{11}B to more than 100 MHz for the nuclei ^{165}Ho and ^{181}Ta that carry very large nuclear quadrupole moments. Since the lowest temperatures used in this thesis correspond to frequencies that lie around several MHz, it is most likely that the nuclei with the largest quadrupole frequencies will have the greatest effects on the dielectric measurements performed in this thesis.

3.3 Influence of nuclear quadrupoles on polarization echoes

The sublevels present due to the nuclear quadrupole moments change the tunneling systems from a two-level to a multi-level system, enabling additional dephasing whose rate depends on the spacing of the sublevels. This spacing can be changed through the application of an external magnetic field that leads to a Zeeman splitting of the sublevels. As the sublevels distance changes with the magnetic field and levels can cross, the dephasing rate will be non monotonous. At large enough fields, the Zeeman splitting of the energy levels will be large enough for the system to become an effective two-level system once again, leading to no additional dephasing and a larger echo amplitude, as seen in figure 3.2.

The effects described above can only be realized in systems containing nuclear electric quadrupoles. An isotope dependent field dependency of the echo amplitude on an external magnetic field would therefore be a strong evidence of the influence of nuclear quadrupoles on the dielectric properties of glasses at low temperatures. Such a measurement was realized in [Nag04] on natural and deuterated glycerol. While natural glycerol contains no nuclear electric quadrupoles, the deuteron nucleus carries a small quadrupole moment. The results of the measurements are shown in figure 3.5.

As predicted by the model, the echo amplitude in the deuterated sample is much

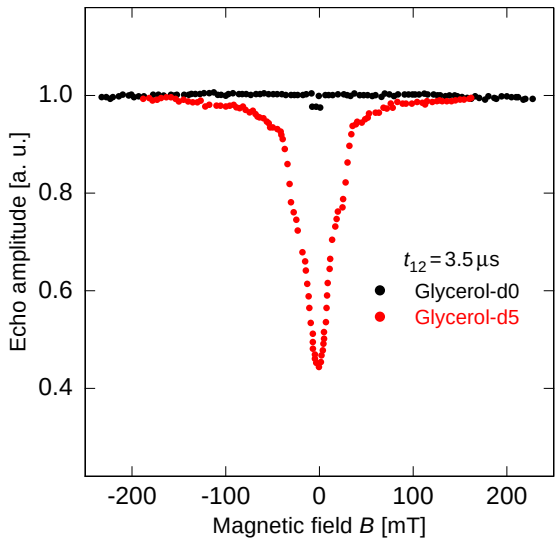

Figure 3.5: Magnetic field effect on the amplitude of two pulse dielectric polarization echoes of natural glycerol-d0 and deuterated glycerol-d8 at 13.4 mK and 1 GHz with a separation time of $t_{12} = 3.5\,\mu s$. Data from [Nag04]

smaller than that of the natural glycerol in zero magnetic field. The application of a magnetic field on deuterated glycerol then leads to an increase of the echo amplitude. At high fields, it approaches the level of the natural glycerol, showing the suppression of a dephasing process only present in the deuterated sample. Subsequent simula-

tions using a microscopic model of tunneling glycerol molecules were able to very accurately describe the magnetic field dependence of the echo amplitude of partially deuterated glyercol, as is shown in figure 3.6 [Baz08].

The measurements shown above were conducted at a fixed pulse separation time

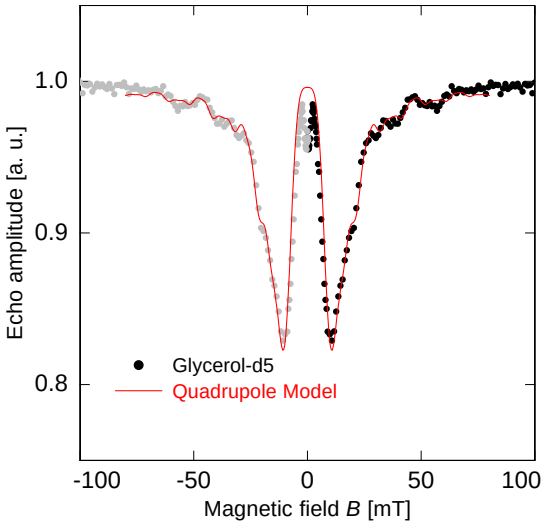

Figure 3.6: Magnetic field dependence of deuterated glycerol at $T = 12\,\mathrm{mK}$ and a pulse separation of $8\,\mu\mathrm{s}$ and a numeric calculation including nuclear quadrupole effects [Baz08].

and in varying fields. The energy splitting of the sublevels at a fixed fields will lead to a beating of the echo amplitude with the pulse separation time due to the transition rate between the sublevels. In a system with a wide variety of electric field gradients and therefore sublevel splittings, the beating can not be directly observed, but will lead to a reduction of the echo amplitude. Glycerol, however, contains tunneling systems with very well homogenous energy splittings and a very small nuclear quadrupole resonance frequency, leading to a small rate and thus an observable beating of the echo amplitude with decay time.

In figure 3.7 the beating of glycerol-d5, where 5 out of 8 possible C−H bonds of each molecule are replaced by C−^{2}H, at a temperature of 4 mK with and without an external magnetic field is shown. The oscillations in zero field are well visible. In high fields, the large Zeeman splitting again leads a suppression of the rate, visible here in the larger echo amplitude without a superimposed oscillation.

As we have seen, the theoretical predictions of the effect of nuclear electric quadrupole moments on the echo amplitude in glasses at low temperatures match the experimental findings very well. Before turning to a model developed for the effects of nuclear quadrupole moments on the dielectric function, we will look at nuclear quadrupole resonance and the energy and frequency ranges that are covered by isotopes found in multicomponent glasses in order to better predict the temperatures and frequencies where effects of nuclear quadrupoles on the dielectric function are to be expected.

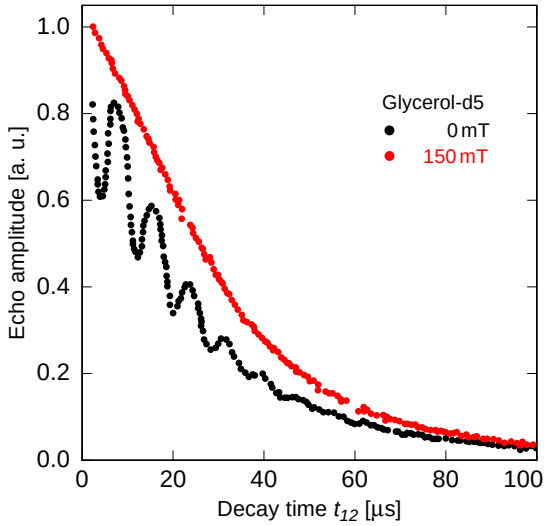

Figure 3.7: Decay of the Echo amplitude in deuterated glycerol at $T = 4\,\mathrm{mK}$ without and with an applied external magnetic field. The beating is due to the quadrupole splitting of the deuteron nuclei [Bar13].

3.4 Influence of nuclear quadrupoles on the dielectric function

As shown in section 3.1, the application of external magnetic fields has a non linear effect on the dielectric function on nuclear quadrupole containing glasses. A theory developed in [Bur06a, Bur06b, Bur06c] investigates possible mechanisms behind this effects.

In each tunneling system containing a particle carrying a nuclear quadrupole moment, we need to compare the two competing processes: On the one hand the tunneling process, that is characterized by the overlap of the coordinate wave functions and thus, as given in (2.18) by the tunneling amplitude Δ_0. On the other hand we now need to take into account the nuclear spin Hamiltonian with its corresponding energy scale of $E_Q = h\nu_Q$ and the overlap of the nuclear spin wave functions

$$\alpha^* = \alpha^n \,, \quad \text{where} \quad \alpha = \langle \psi_{Ql} | \psi_{Qr} \rangle \tag{3.9}$$

that depends on the number n of tunneling particles involved in one tunneling system [Bur06c].

If the tunneling amplitude is larger than the quadrupole interaction, $\Delta_0 > nE_Q$, the system is dominated by tunneling described by the standard tunneling model. If, however, the quadrupole interaction becomes comparable to or even larger than the tunneling amplitude, the effect must be taken into account. The effective tunneling amplitude of such a system is given both by the coordinate and the nuclear spin waveform overlap, yielding

$$\Delta_0^* = \alpha^* \Delta_0 \,. \tag{3.10}$$

The effective tunneling parameter can therefore be summarized as being

$$\Delta_0^* = \begin{cases} \Delta_0 & \Delta_0 \gg nE_Q, \\ \alpha^n \Delta_0 & \Delta_0 \ll nE_Q. \end{cases} \tag{3.11}$$

The renormalization of the tunneling parameter leads to a gap in the distribution of the effective tunneling amplitude Δ_0^* and thereby in the total density of states:

$$P\left(\Delta_0^*\right) = \begin{cases} P/\Delta_0^* & \Delta_0^* \gg nE_Q, \\ 0 & \alpha^n nE_Q \ll \Delta_0^* \ll nE_Q, \\ P/\Delta_0^* & \Delta_0^* \ll \alpha^n nE_Q. \end{cases} \tag{3.12}$$

This formula is only true, if we look at the lowest energy sublevels. If the temperature is far larger than the quadrupole interaction, all sublevels can contribute to the dielectric function and the effective signal is not altered. so that $\Delta_0^* = \Delta_0$. At lower Temperatures, $k_\mathrm{B}T \ll E_Q$, only the lowest sublevels will contribute and the reduced tunneling parameter (3.10) is valid.
We therefore expect a plateau in $\delta\varepsilon'/\varepsilon'$ at temperatures $nE_Q\alpha^n < k_\mathrm{B}T < E_Q$ and an unchanged behavior of the dielectric function at both higher and lower temperatures. The plateau will become more pronounced at higher nuclear spins and if more particles participate in the tunneling motion. In figure 3.8, the calculated gaps in the distribution function for $I = 1$ and various numbers n are depicted. Instead of using

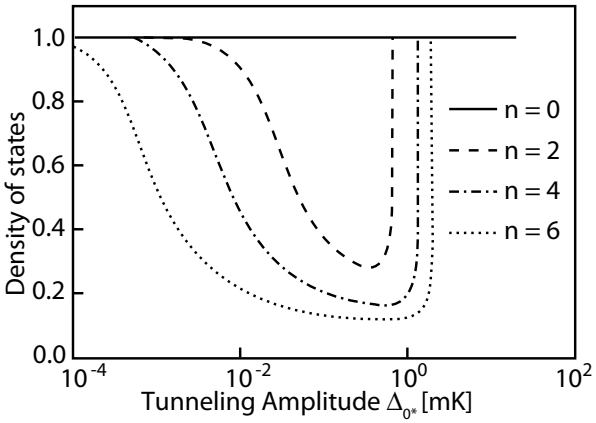

Figure 3.8: Pseudogaps in the distribution function of Δ_0^* for $I = 1$ and varying numbers of tunneling particles, compared to the flat distribution of the standard tunneling model for $n = 0$.

the exact form of the gap as given in [Bur06c] for simulations, it was approximated by a modified Gaussian gap in the flat distribution

$$P(\Delta_0, E)\,\mathrm{d}\Delta_0\mathrm{d}E = P_\mathrm{STM}\; A\left(1 - a\,\exp\left(\frac{-(\Delta_0 - h\nu_Q)^2}{2(k_\mathrm{B}\delta T)^2}\right)^4\right)\,\mathrm{d}\Delta_0\mathrm{d}E\;. \tag{3.13}$$

This form of the pseudogap is steeper than a regular Gaussian, leading to a less pronounced effect at smallest Δ_0^*, that would be similar to the cutting off of Δ_0 described in section 2.4.2. This way, the pure effect of the plateau is more pronounced.

For the simulation, a depth of $a = 0.9$, a quadrupole interaction energy of $h\nu_Q = 20\,\mathrm{mK}$ and a width of $k_\mathrm{B}\delta T = 6\,\mathrm{mK}$ was chosen. This is at the upper maximum of expected quadrupole interaction energies as given in table 3.1. As seen in figure

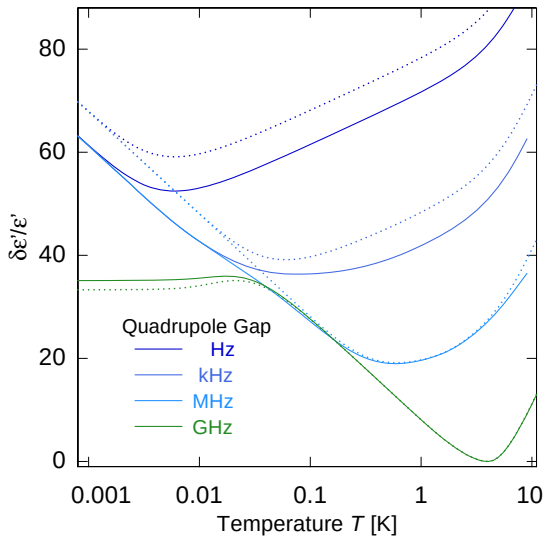

Figure 3.9: Change of the real part of the dielectric function $\delta\varepsilon'/\varepsilon'$ as a function of temperature for frequencies between 1 Hz and 1 GHz and with a modified distribution function due to long range interaction, as given by (3.13). Unmodified calculations of the standard tunneling model are shown as dotted lines.

3.9, the pseudogap leads not to a clear plateau, but rather to a slight flattening off at the resonant interaction slope of $\delta\varepsilon'/\varepsilon'$. This is most clear at high frequencies, where the onset of relaxational processes happens at temperatures far higher than the quadrupole interaction energy. At frequencies where the minimum is in the temperature range of the gap, it is strongly deformed. In our case, we see a broadened minimum of the 1 kHz curve. The slope at lowest frequencies is unchanged when compared to the unmodified curves of the standard tunneling model in figure 2.15.
The considerations above were made for zero magnetic field. Applying an external magnetic field will have several effects: At small fields, possible degeneracies of levels will be lifted via Zeeman splitting, leading to more available levels and to an effective increase in the distribution function. This would increase the dielectric response of the system. At higher fields, the Zeeman splitting will be so large, that the double well potentials will effectively become two-level systems again. If the interaction with the magnetic field is stronger than the quadrupole interaction, the overlap of the spin part of the wave function will become unity. A quadrupole carrying glass in high fields should therefore show standard tunneling model like behavior, as discussed for polarization echoes in section 3.1.

In figure 3.10, the real part of the dielectric function of Albasi is shown, both in zero field and at as a combination of data taken at the fields where the dielectric function is maximal in figure 3.1 and where the influence of nuclear quadrupoles should therefore be minimal.
The plateau at temperatures below about 10 mK is very pronounced in zero field.

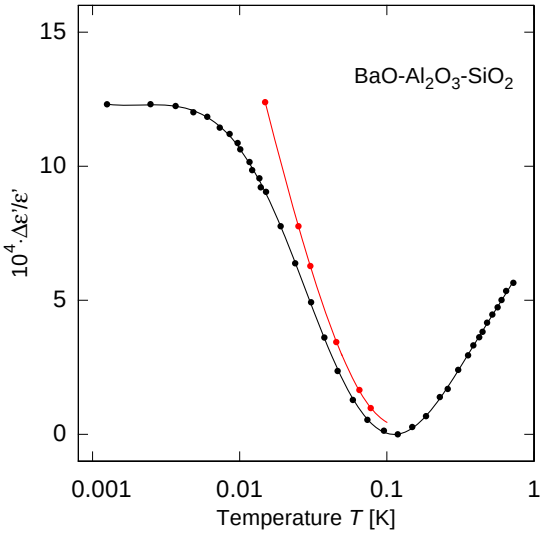

Figure 3.10: Real part of the dielectric function $\Delta\varepsilon'/\varepsilon'$ of Albasi at zero field (black) and at the fields of maximal $\Delta\varepsilon'/\varepsilon'$, as shown in figure 3.1. [Ket99].

Using estimations made with the quadrupole model in [Bur06c], the quadrupole interaction would have to be very strong and more than six atoms carrying the relevant quadrupole moment would have to form tunneling systems. It is intriguing to see, that the magnetic fields lift the dielectric function and lead to a behavior that is consistent with the standard tunneling model, even showing the $-2:1$ slope ratio. The quadrupole model described above does predict this magnetic field effect, but only at much larger fields than those in the millitesla range applied in this case.
The effect of nuclear quadrupoles on the dielectric function at temperatures $k_\mathrm{B}T > E_Q$ have also been considered [Ser07]. The model here predicts an additional contribution to $\delta\varepsilon'/\varepsilon'$ that at high temperatures is proportional to E_Q/T. It then drops to zero at $E_Q \approx k_\mathrm{B}T$ and the dephasing due to the interaction described above takes over. Like all effects caused by nuclear quadrupoles, this additional $1/T$ contribution to the dielectric function should be very sensitive to magnetic fields and in this case first show a strong increase and then a slow decrease with increasing magnetic field strengths.
Until now, only resonant processes contributing to the dielectric function have been considered here. As strong quadrupole interactions can move the energy scale to temperatures where relaxational processes are important, a possible influence of should be considered. The rather closely spaced additional sublevels can be a source for a non phononic relaxation, especially if tunneling systems can interact over long distances [Bur06a, Pol05]. The long range interaction has discussed in section 2.4.3 has been attributed to nuclear quadrupoles in [Pol05], therefore predicting both τ_1 and τ_2 to have a $1/T$ dependence. In this case the interaction driven relaxation would be strongly magnetic field dependent [Bur06a].
First hints of a relaxational interaction of two-level systems in glasses with nuclear quadrupole moments have been observed at measurements of the nuclear spin lat-

tice relaxation times τ_1 in doped amorphous borates [Sze75]: When compared to the relaxation times in crystals, the nuclear relaxation times of quadrupole carrying nuclei was more than one order of magnitude shorter. An interaction between the quadrupole moments and nearby tunneling systems might account for this drastic effect.

All of the models discussed above only consider nuclear quadrupoles that are part of two-level tunneling systems. The effects predicted therefore should be smaller than or at most equal to effects predicted by the standard tunneling model, as in multicomponent glasses not all tunneling systems contain atoms carrying nuclear quadrupoles.

4. Experimental Methods

Having given an introduction to the theoretical background relevant for the measurements performed in the framework of this thesis in chapter 2, this chapter will focus on the experimental methods employed. First, a short introduction to the working principle of dilution cryostats is given, followed by a brief section concerning thermometry.
As the measurements within this thesis span almost eight orders of magnitude in frequency, ranging from 60 Hz to 1 GHz, we have used three different measurement setups, that will be described here. A special focus is hereby put on the low frequency setup, as the focus of the thesis is set on measurements in the hertz to kilohertz regime.
Finally, we will have a look at the four different glass samples used for this thesis and their chemical composition.

4.1 Generation and measurement of low temperatures

4.1.1 Working principle of a dilution cryostat

Within the framework of this thesis, the dielectric properties of different glasses were measured between 7.5 mK and 300 K. In order to be able make measurements at stable temperatures at lowest temperatures for extended periods of time, a dilution refrigerator was employed. Detailed descriptions of the working principles of these machines can be found in literature [Ens05, Pob07], so only a short introduction will be given here.

The dilution refrigerator uses a closed cycle of a ^{3}He/^{4}He mixture, as is schematically shown in figure 4.1. Towards low temperatures $T < 700\,\mathrm{mK}$, the two helium isotopes separate into distinct phases, thus lowering their entropy. However, even at lowest temperatures $T \to 0$ and at normal pressure, about 6.5 % of ^{3}He are dissolved in ^{4}He , as this minimizes the system's total energy. In the cryostats mixing chamber, we therefore find a phase of almost pure ^{3}He floating on top of the heavier ^{3}He/^{4}He mixture. If the concentration of ^{3}He in the mixture is reduced, ^{3}He atoms will transfer form the concentrated phase into the dilute phase. As their entropy is lower in the concentrated phase, this transition effectively cools its surroundings by $\Delta Q = T\Delta S = 84\,\mathrm{J/K^2}T^2$ per mol ^{3}He.
The depletion of the ^{3}He/^{4}He phase is achieved by connecting the mixing chamber to the so called still, where the mixture is heated to about 700 mK. The ^{3}He evapo-

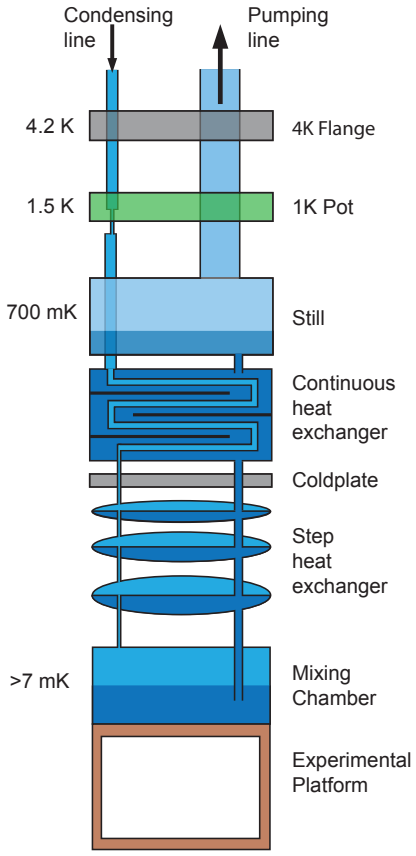

Figure 4.1: Schematic drawing of a dilution cryostat with the ^{4}He rich phase depicted in dark and the concentrated ^{3}He phase in light blue. The drawn components are enclosed by a vacuum chamber connected to the 4 K flange and surrounded with liquid ^{4}He This so called helium bath is not drawn here. Approximate temperatures are given at the different stages of the cryostat from the 4 K flange to the mixing chamber.

rates easily, while the ^{4}He with its higher boiling temperature will almost completely remain in its liquid phase. The resulting vapor is then pumped, cleaned, and recondensed using the precooling of both a helium bath above the 4 K flange and the 1 K–pot. This pot, filled with ^{4}He from the bath and pumped, has a temperature of about 1.5 K.

The precooled ^{3}He then flows back through capillaries to the mixing chamber via two sets of counterflow heat exchangers that minimize the heat input to the mixing chamber and the attached experimental platform. The quality of the heat exchangers and the existence of heat leaks (for example due to cables leading from room temperature to the experimental platform) determine the base temperature of the cryostat. In the case of the cryostats used in this thesis, base temperatures of about 6 mK allowed stable measurements of 7.5 mK and upward by heating the experimental platform.

If the experimental platform is heated to temperatures above approximately 1.4 K, the ^{3}He/^{4}He mixture starts to evaporate quickly, making stabilized measurements impossible. In order to be able to measure up to about 10 K, it is useful to only inject a small amount of the mixture into the system to thermally connect the 1 K–pot to

the experimental platform and use the ^{3}He/^{4}He cycle as a well pumped evaporation cryostat.

4.1.2 Thermometry

We differentiate between two classes of thermometers: Primary thermometers like fix point thermometers or noise thermometers allow a direct determination of the temperature without prior calibration. Often, however, they provide only a few discrete temperature points or need several minutes for the determination of a temperature. In order for stable, temperature dependent measurements to be conducted, we therefore used different resistance thermometers. These secondary thermometers need to be calibrated against primary thermometers but then provide continuous and fast temperature measurements.

Measurements below 10 K were performed with carbon resistors showing a temperature dependent resistance that grows monotonously for $T \to 0$. At 10 mK, the resistance of the carbon resistors used in this thesis is about 150 kΩ. The readout was performed with AC resistance bridges AVS-47[1] or LR700[2]. These bridges can perform very precise measurements using only very small excitation voltages, which prevents an overheating of the thermometer at lowest temperatures.

At higher temperatures, above 10 K, the temperature was measured using either a RhFe-thermometer or a Si-diode. The principle of the measurement was the same, as with the carbon thermometer, but the almost linear temperature dependence of the resistance of RhFe at higher temperatures allows for comfortable measurements in this temperature range. The Si-diode is a calibrated model [3], set up for measurements from room temperature down to about 4 K.

4.1.3 Cables and heat sinks

In order to prevent heating of the measurement setup by the cables leading down from room temperature into the cryostat, both the inner and outer conductor of the coaxial cables used for the measurements were thermally anchored at the thermal stages of the cryostat. In order to prevent reflections in the cables, the heat sinks were matched to 50 Ω impedance. As is shown in figure 4.2, the outer conductor is connected directly to a gold plated copper box via an SMA connector, while the

[1] AVS-47, RV-Elektroniikka Oy Picowatt, Veromiehentie 14, FI-01510 Vantaa, Finland
[2] LR700, Linear Research Inc., 5231 Cushman Place, Suite 21, San Diego, CA 92110-3910, USA
[3] LakeShore model DT-670-CU1.4L, Lake Shore Cryotronics Inc., Westerville Ohio 43082, USA

inner conductor of the SMA connector is soldered to a Niobium strip on a thin sapphire plate. For the stages above the still, semi rigid coaxial cables were used for

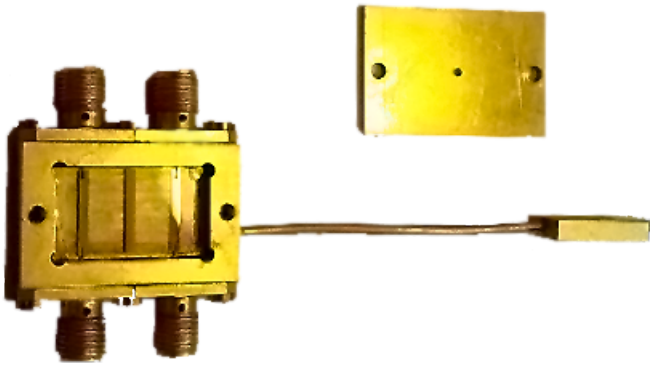

Figure 4.2: Heat sink as used in this thesis: 50 Ω impedance matched setup suitable for high frequency measurements.

all measurements. Below this stage, they were only used for the measurements at high frequencies close to 1 GHz. As the cables had no direct connection to the sample (see section 4.4), they were not heat sunk below the still. For the lower frequency measurements stainless steel mini coaxial cables were used, that were heat sunk at the experimental platform.

4.2 Measurement setup for low frequency measurements

The main focus of this thesis was on low frequency measurements of the dielectric function at low temperatures. We have used a microstructured interdigital capacitance, that allows for a very good thermal coupling. The details of the measurement setup, the readout, thermal coupling and the conversion of the measured data to the complex dielectric function treated by theory are given in this section.

4.2.1 Microstructured interdigital capacitance

The usual form of capacitors used in precision measurements of the dielectric constant is that of a simple or stacked plate capacitor. While this shape offers the advantage of homogenous, easily calculable field distributions, the ratio between the capacitance and the amount of dielectric employed depends linearly on the thickness of the sample. With a typical sample of about $10 \times 10 \times 0.5\,\mathrm{mm}^3$, one obtains capacitances of only 3 pF to 10 pF, depending on the sample's relative permittivity. Since the measurements at low frequencies were direct measurements of the capacitance, a larger value would increase the precision of the measurement. At the same time, the sample needed to be kept small and well thermally connected in order to prevent thermal decoupling.

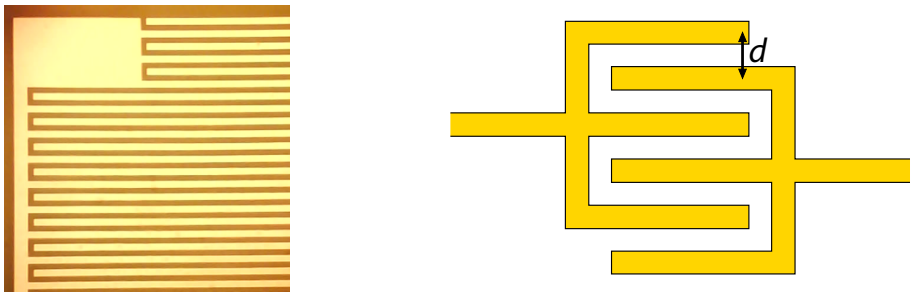

Figure 4.3: Detail of the interdigital capacitance and one bond pad (left) and schematic drawing of the interdigital structure (right) used for the low frequency measurements. The distance between the centers of two adjacent fingers was chosen to $d = 50\,\mu m$.

This combination of requirements was achieved by using a microstructured interdigital capacitance, as shown in figure 4.3 [Kin08]. The fingers form parallel capacitors on the surface of the glass, leading to a far larger total capacitance. As the electric field distribution for this capacitor can not be calculated analytically, a finite element simulation [4] was used in order to simulate the distribution. A sample simulation is shown in 4.4. The total capacitance per area of the interdigital capacitor increases, if

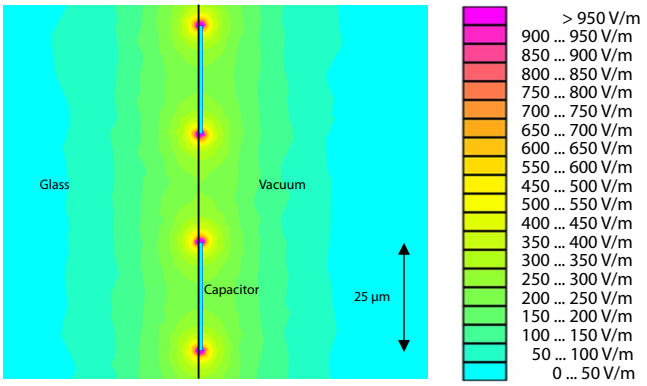

Figure 4.4: Finite element simulation of the electric field distribution of the interdigital capacitance. The relative permittivity of N-KZFS11 and a voltage of $V_{exc} = 10\,mV$ were used.

the distance d of the fingers is decreased. However, this also leads to higher electric fields at constant excitation voltages V_{exc}. This then can lead to non linear excitation of the sample, as equation (2.63) is no longer fulfilled. The distance of the fingers is therefore always a compromise between low enough electric fields and high enough capacitances.

Both the finger size and their distance for all interdigital capacitors that were measured in this thesis was chosen to be $25\,\mu m$, leading to a total distance between centers of adjacent fingers of $d = 50\,\mu m$. The simulation then shows a maximal electric field strength of about $|F| \approx 2\,kV/m$ for an excitation voltage of $10\,mV$. The estimated limit for the linear range, given a typical dipole moment of $p_0 = 3\,D$ and a temperature of $5\,mK$ is $20\,kV/m$, so the linear range lies well within the possibilities

[4] www.femm.info/wiki/HomePage

of the measurement setup.
The total interdigital capacitance consists of 140 fingers of 10 mm and 60 fingers of 4 mm on glass samples that have a total size of $12 \times 12 \times 0.5\,\mathrm{mm}^3$. The fingers are made of a 800 nm copper layer covered with 200 nm of gold to prevent oxidation.

4.2.2 Sample holder

The sample holder used for low frequency measurements is shown in figure 4.5. It was built to maximize thermal contact between the sample and the holder and consists of a T-shaped copper body, that is covered in 1.5 µm of gold to prevent oxidation and for a better thermal connection of the sample.

The sample itself is pressed to the holder via a CuBe-spring. Since the microfabri-

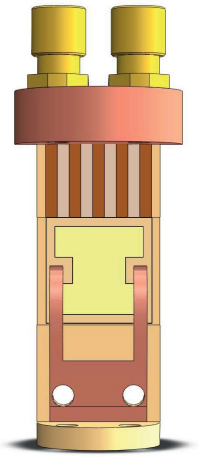

Figure 4.5: Sample holder for the low frequency measurements with the microstructured interdigital capacitance.

cated structure of the interdigital capacitance only uses one side of the sample, the back can be fully metalized with 1.9 µm of copper and 100 nm of gold, ensuring a good thermal contact. In order to make the contact even better, two holes of about 8 mm × 2 mm were cut into the holder, directly behind the sample. Through these holes, 25 µm gold bonds can connect the back of the sample and the holder. Between 12 and 30 bonds were placed for each measurement.
For the readout of the capacitance via the measurement bridge, coaxial cables were connected to the sample holder via SMA connectors. The inner conductors of the SMA connectors on the holder were soldered to copper strips on Kapton foil that was glued to the sample holder. The copper strips were then bonded to the sample via 25 µm aluminum bonds. As these bonds become superconducting below 1.19 K the sample was thermally isolated from the cables at low temperatures.

4.2.3 Thermal coupling of the sample

The mean value for heat dissipated in the sample due to an applied ac electric field of frequency ν and excitation voltage V_{exc} on the capacitor is

$$P = \frac{1}{4} C \nu V_{\mathrm{exc}}^2 \tan(\delta) \; . \tag{4.1}$$

Even for the highest frequency $\nu = 20\,\mathrm{kHz}$ and an excitation voltage of 10 mV applied on the sample with the largest capacitance $C = 80\,\mathrm{pF}$ used in this thesis and including $\tan(\delta) = 0.1$ due to the low pass filters, the dissipated power is only 4 pW, so no thermal decoupling should be expected even at lowest temperatures.

As different thermal resistances play a role in the thermalization of the sample,

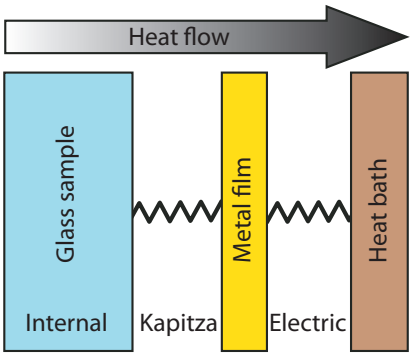

Figure 4.6: Schematic model of the thermal resistances present in the low frequency measurement setup. The total thermal resistance is a sum of the internal thermal resistance of the sample, the Kapitza resistance and the resistance of the gold bonds.

we will nonetheless have a closer look at their temperature dependent contributions. Any heat dissipated within the sample must first travel through the sample, then the metal film and finally the gold bonds in order to reach the heat bath of the experimental platform, as shown schematically in figure 4.6. As the thermal conductances all become smaller towards lowest temperatures, their values at 10 mK are compared below.

Internal heat resistance of the glass Heat produced in the interdigital capacitor during measurements must travel through the entire glass sample of thickness d. The internal thermal conductivity of the sample must therefore be taken into consideration. It was already shown in section 2.2 that the thermal conductivity of glasses decreases quadratically with temperatures. As an approximation for all samples, we will use the thermal conductivity of vitreous silica, that is about $\kappa \approx 1\,\mathrm{W/cm\,K}$ at 1 K. If the heat is produced on top of the sample, we find

$$G_{\mathrm{gl}}(T) = \kappa \frac{A}{d} \left(\frac{T}{T_0} \right)^2 = 0.3\,\mathrm{nW/mK} \left(\frac{T}{10\,\mathrm{mK}} \right)^2 \; . \tag{4.2}$$

Internal heat that is released due to thermalization after a temperature step is created homogeneously in the sample and must therefore travel smaller distances, so the thermal conductivity given above is a lower boundary.

Kapitza resistance At the interface of the glass substrate and the metallic film, a thermal boundary resistance due to acoustic mismatch occurs [Swa89]. This so-called Kapitza resistance is of the form

$$R_{\mathrm{K}}(T) = \frac{R_1^2}{A} T^3 \,. \tag{4.3}$$

Using the numerical tables in [Che76], we can approximate the thermal boundary resistance R_1^2 between copper and the glass samples used in this thesis. As the boundary resistance depends on the speed of sound, that is rather similar in all samples, and the density we find $R_{\mathrm{Gl1}}^{\mathrm{Cu}} \approx 9.5\,\mathrm{K}^4\,\mathrm{cm}^2/\mathrm{W}$ for Herasil and $R_{\mathrm{Gl2}}^{Cu} \approx 7.8\,\mathrm{K}^4\,\mathrm{cm}^2/\mathrm{W}$ for N-KZFS11.
With a sample size of $1.2\,\mathrm{cm} \times 1.2\,\mathrm{cm}$ that is fully metalized, the total thermal conductivity due to the Kapitza resistance becomes

$$G_{\mathrm{K}}(T) = \frac{1}{R_{\mathrm{K}}(T)} = T^3(0.15 - 0.18)\mathrm{W/K}^4 = (0.15 - 0.18)\mathrm{nW/mK} \left(\frac{T}{10\,\mathrm{mK}}\right)^3 . \tag{4.4}$$

Thermal conductivity of the metal bonds The thermal conductivity from the gold film on the glass sample to the sample holder can be approximated by that of the gold bonds with an average length of 2.5 mm and a diameter of 25 µm that connect the two pieces. Using the Wiedeman-Frantz law that connects thermal and electrical conductivity via the constant $L = 2.44 \times 10^{-8}\,\mathrm{W}\,\Omega/\mathrm{K}^2$, we find

$$G_{\mathrm{el}}(T) = \frac{L}{R_{4\mathrm{K}}} T = n\,0.039\,\mathrm{nW/mK} \left(\frac{T}{10\,\mathrm{mK}}\right) , \tag{4.5}$$

where we have calculated the resistance $R_{4\mathrm{K}} = \rho_{\mathrm{el}}\, l/(A\, RRR)$ at 4 K via the specific resistivity $\rho_{\mathrm{el}} = 2.4 \times 10^{-8}\,\Omega/\mathrm{m}$ of gold at room temperature and a typical RRR of 20 for the gold bonds. The total thermal conductivity then depends on the number n of bonds set. As it was always at least 12, the lowest conductivity through the bonds was 0.52 nW/mK at 10 mK.

The total thermal conductance is given by

$$G_{\mathrm{tot}} = \left(\frac{1}{G_{\mathrm{gl}}} + \frac{1}{G_{\mathrm{K}}} + \frac{1}{G_{\mathrm{el}}}\right)^{-1} . \tag{4.6}$$

As has been shown above, all three components are roughly equal at 10 mK. At higher temperatures, the electric heat conductivity of the bonds will limit G_{tot}, while at lower temperatures the Kapitza resistance becomes the dominant contribution.

4.2.4 Data readout

The data readout for the low frequency measurements was accomplished using a commercial AH2700[5] capacitance bridge, a schematic drawing of which is shown in figure 4.7. The bridge generates sinusoidal signals with frequencies ranging from $\nu = \omega/2\pi = 60\,\mathrm{Hz}$ to $20\,\mathrm{kHz}$ and using excitation voltages V_{exc} between $0.1\,\mathrm{mV}$ and $15\,\mathrm{V}$. The voltage is applied at the High gate of the bridge. By varying the Tap 1

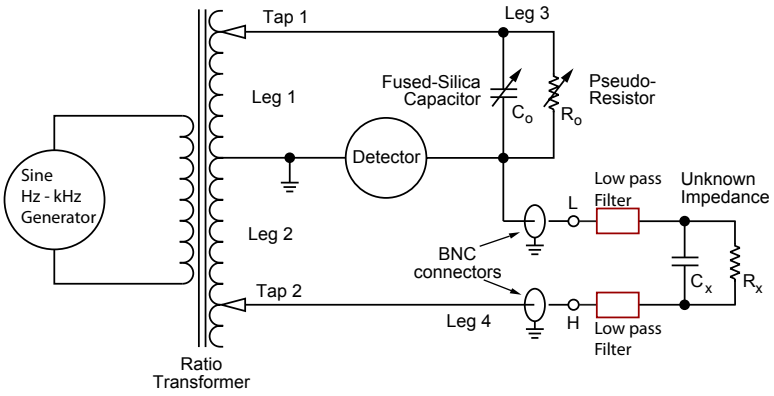

Figure 4.7: Schematic circuit diagram of the AH2700 capacitance bridge. The red low pass filters introduced in section 4.2.6 were directly connected to the BNC connectors at the High and Low end [AH04].

and 2, as well as the reference impedance $R_0 + \mathrm{i}\omega C_0$, the unknown impedance of the sample can be measured. Both the signal in phase and shifted by $\pi/2$ are read out and then converted to the measurement quantities C and $\tan(\delta)$, the values are then read out via a LabVIEW[6] program.

The reference impedance in the capacitance bridge is kept at a constant temperature and allows for an accuracy of $\pm 5\,\mathrm{ppm}$ using optimal excitation voltages. The voltages used in the course of this thesis were usually far lower than the optimal ones used for capacitances of about $100\,\mathrm{pF}$, lowering the accuracy by about one order of magnitude. At each sample, measurements with very low excitation voltages $V_{\mathrm{exc}} \leq 1\,\mathrm{mV}$ were taken and then compared to measurements taken at higher voltages to rule out thermal decoupling and nonlinear excitations. These higher voltages of about $3\,\mathrm{mV}$ to $30\,\mathrm{mV}$ allow for more precise measurements.

The low pass filter boxes were introduced in order to suppress high voltage signals that couple into the bridge's output. Even at very small amplitudes they can disturb the measurements, as is discussed in section 4.2.6. Signals coupling into the measurement line are suppressed by commutation of the bridge's signal.

[5] Andeen Hagerling, 31200 Bainbridge Road Cleveland, Ohio 44139-2231 U.S.A., www.andeen-hagerling.com/

[6] LabVIEW 6.0, National Instruments, Austin, Texas, USA, /www.ni.com/labview/

4.2.5 Correcting for stray capacitances

The total measured capacitance C is the sum of the capacitance of the dielectric filled sample C_s and a parasitic stray capacitance C_p due to the electric field in the vacuum above the interdigital capacitor. It needs to be taken into account when calculating $\Delta\varepsilon'/\varepsilon'$ and $\tan(\delta)$ of the sample from the measured values.
If we assume the stray capacitance to be parallel to the dielectric filled capacitance, we can calculate a filling factor

$$f = \frac{C_\mathrm{s}}{C} = \frac{C - C_\mathrm{p}}{C} \,. \tag{4.7}$$

From the measured capacitance we then find

$$\frac{\Delta C}{C} = \frac{\Delta C_\mathrm{s}}{C_\mathrm{s}} \frac{C_\mathrm{s}}{C} = \frac{\Delta\varepsilon'}{\varepsilon'} \, f \,, \tag{4.8}$$

where we assume the stray capacitance to be temperature independent. For the loss tangent of the sample, we need to assume an RC parallel circuit as an equivalent circuit for the measurement setup. We then find

$$\tan(\delta)_\mathrm{meas} = \frac{1}{2\pi\nu RC} = \frac{1}{2\pi\nu RC_\mathrm{s}} \frac{C_\mathrm{s}}{C} = \tan(\delta) \, f \,, \tag{4.9}$$

where R is the dissipative resistance of the equivalent circuit, that is assumed to be solely caused by the dielectric.

The simulation of finger pairs using the relative permittivity of the samples used in this thesis as given in table 4.1 yields parasitic stray capacitances of

$$C_\mathrm{p}(\text{Herasil}) = 8.2\,\mathrm{pF} \qquad C_\mathrm{p}(\text{HY-1}) = 9.7\,\mathrm{pF} \qquad C_\mathrm{p}(\text{N-KZFS11}) = 10\,\mathrm{pF} \,. \tag{4.10}$$

The total capacitance of the setup at temperatures below 10 K is

$$C(\text{Herasil}) = 37\,\mathrm{pF} \qquad C(\text{HY-1}) = 60\,\mathrm{pF} \qquad C(\text{N-KZFS11}) = 79\,\mathrm{pF} \,, \tag{4.11}$$

leading to filling factors between 0.77 and 0.9, for which the measured data needs to be corrected. The values are in good agreement with the approximation

$$f \approx \frac{\varepsilon'}{\varepsilon' + 1} \tag{4.12}$$

which can be used, as due to the flat interdigital capacitor the measurement setup is symmetric with respect to the dielectric filled sample and the vacuum above it.

4.2.6 Low pass filters

The measurements in this thesis were conducted down to temperatures of 7.5 mK. Even with a very good thermalization of the samples and the suppression of parasitic heat input via the cables, a flattening of the curves towards lowest temperatures had been observed in previous measurements [Däh10]. This could be attributed to high frequencies that are generated in very small amplitudes by the AH2700 capacitance bridge.

The low pass filters, shown schematically in figure 4.8, were designed using

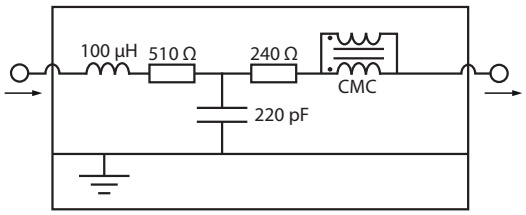

Figure 4.8: Schematic circuit diagram of the low pass filters used in this thesis. The cutoff frequency is at $\nu_0 \approx 1\,\mathrm{MHz}$.

the electrical circuit simulation LT Spice IV[7]. They effectively suppress frequencies above $\nu_0 \approx 1\,\mathrm{MHz}$. In addition to an RLC low pass, they also contain common mode chokes[8] that further reduce noise.

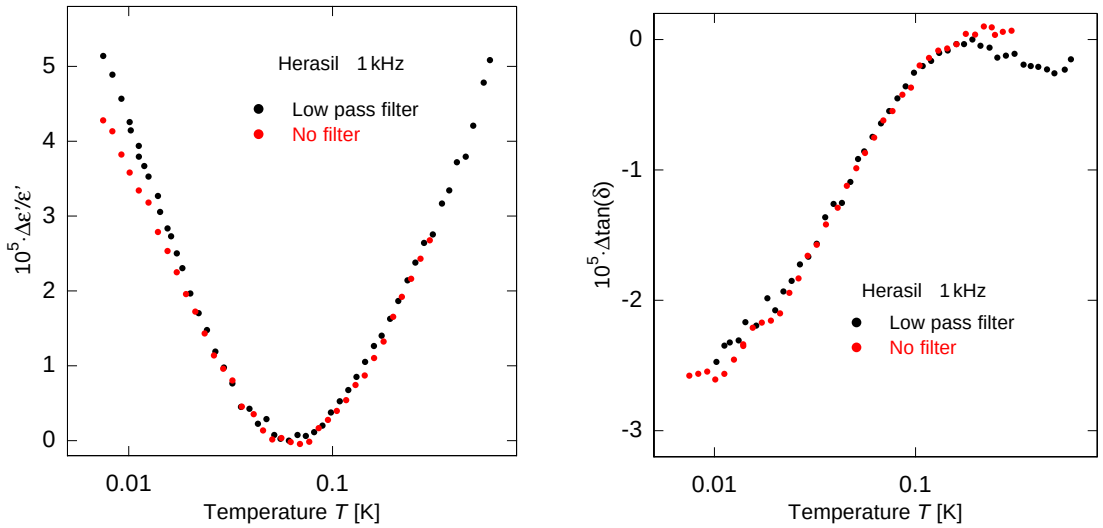

Figure 4.9: Change of the dielectric function $\Delta\varepsilon'/\varepsilon'$ (left) and the loss tangent $\Delta\tan(\delta)$ (right) of Herasil as a function of temperature for a frequency of 1 kHz, with and without low pass filters.

[7] www.linear.com/designtools/software/#LTspice
[8] SMD Common Line Filter 744226, Wuerth Electronics

The effect of low pass filtering on a sample of Herasil quartz glass is shown in figure 4.9. In the real part $\delta\varepsilon'/\varepsilon'$ we see a clear difference between unfiltered and filtered data at lowest temperatures, while the scattering of the loss data $\tan(\delta)$ makes it much harder to see a clear distinction. Above 30 mK, the high frequency noise seems to play only a negligible role.
The filters together with the capacitance on the sample form an RLC component, that turns the angle of the capacitance C^* and the loss tangent $\tan(\delta)^*$ measured by the capacitance bridge. The additional phase angle is about 0.1 rad at 20 kHz and rapidly decreases towards lower frequencies. It is therefore necessary to compensate for this effect in order to obtain an undistorted signal from the sample.
The measured loss tangent with filter boxes consists of the loss stemming from the sample $\tan(\delta)_s$ that changes with temperature, and an additional angle from the low pass filter $\tan(\delta)_f$, that is assumed to be constant. The correction angle then becomes

$$\delta_0 = a \cdot \arctan\left(\tan(\delta)_{\min}\right) \quad \text{where} \quad a = \frac{\tan(\delta)_{\min}}{\tan(\delta)_{\max}} \,, \tag{4.13}$$

where $\tan(\delta)_{\min}$ and $\tan(\delta)_{\max}$ are the smallest and largest measured values at each measurement. By including the factor a, we prevent an over correction of the additional loss tangent and acknowledge the fact, that there might be an intrinsic loss of the sample even at lowest temperatures.
Conversions from C^*, $\tan(\delta)^*$ to C, $\tan(\delta)$ then can be achieved by first changing from the loss tangent to the imaginary part of a complex capacitance $C^* = C^*_{\mathrm{re}} + \mathrm{i}C^*_{\mathrm{im}}$

$$C^*_{\mathrm{im}} = C^*_{\mathrm{re}} \ \tan(\delta)^* \tag{4.14}$$

and rotating both C^*_{re} and C^*_{im} by an angle of $-\delta_0$. The resulting complex capacitance C_{re} and C_{im} can then be used to obtain the loss tangent $\tan(\delta) = C_{\mathrm{im}}/C_{\mathrm{re}}$.
The angle correction due to the low pass filters changes neither the temperature dependence of the real part $\delta\varepsilon'/\varepsilon'$, nor of the loss tangent $\tan(\delta)$. Its influence is only on the absolute value of $\tan(\delta)$, as was checked by comparing unfiltered data with both corrected and uncorrected low pass filtered measurements.

Figure 4.10 shows the results of these comparisons. The unfiltered data only goes down to 15 mK, as no thermalization steps were taken for this measurements, leading to thermal decoupling at lower temperatures.
Although the low pass filters cause a loss angle of $\delta \approx 0.1$, which is very large compared to the value of $\delta = 1.5 \times 10^{-3}$ measured without filters in the high temperature plateau region, the use of low pass filters does not distort the curves significantly. An exact determination of $\tan(\delta)$ is, however, not possible even after the correction, which only gives us values within about 50% of the true value, mostly due to the unknown residual loss at lowest temperatures.
The temperature ramps measured in this thesis were mostly taken with filters, as

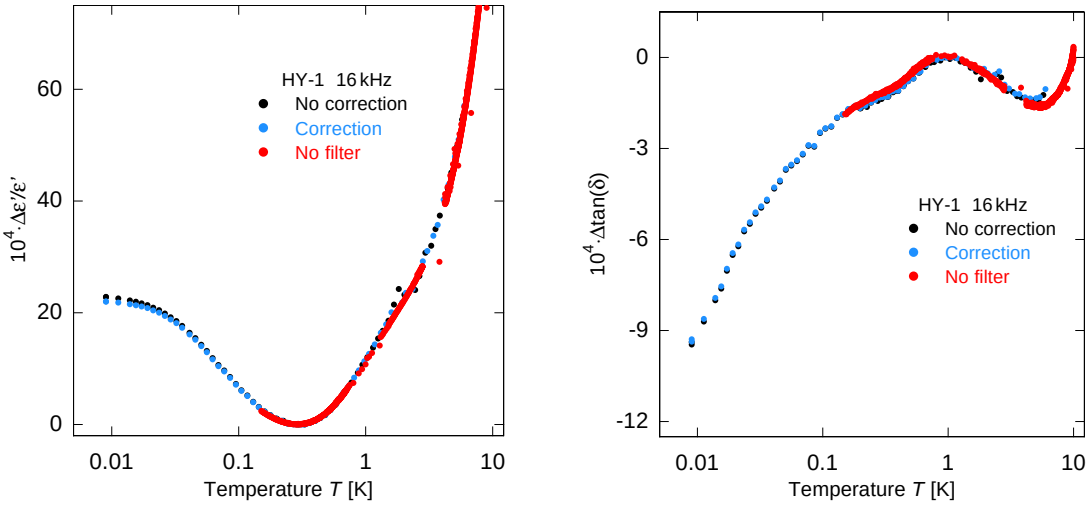

Figure 4.10: Change of the dielectric function $\Delta\varepsilon'/\varepsilon'$ (left) and the loss tangent $\Delta\tan(\delta)$ (right) of HY-1 as a function of temperature for a frequency of 16 kHz. The black and blue curves are measured with low pass filters and then corrected (blue) , the red data points without filters.

in this way continuous measurements could be taken down to lowest temperatures. An absolute value of the loss tangent $\tan(\delta)$ could therefore not be determined for all measurements. The same is true for the high frequency measurements due to the intrinsic quality factors of the LC resonators, whose value could not be determined to the precision of 1×10^{-6} necessary for the absolute value of the loss tangent. We therefore only look at the change of the loss tangent $\Delta\tan(\delta)$ in the analysis of the data.

4.3 Measurement setup for MHz measurements

In contrast to the direct measurements of the capacitance and loss tangent via a capacitance bridge performed at low frequencies, the measurements at higher frequencies were conducted using LC resonators. Their resonance frequency ν_0 and quality factor Q also allow the calculation of $\Delta\varepsilon'/\varepsilon'$ and $\Delta\tan(\delta)$. The design of the resonator, signal path and data readout as well as the conversion of the measured quantities into the desired ones are discussed below.

4.3.1 LC resonator

The measurements performed in the MHz range were conducted using the LC resonator, that is shown in figure 4.11 and was developed in [Zei15]. It consists of two

parallel capacitors filled with the sample and a coil of silver plated copper wire and has a total diameter of 40 mm and a height of 50 mm. It is designed to provide excellent thermal coupling, an intrinsic quality factor of $Q > 1000$ at high temperatures and contains no additional dielectric apart from the samples, thus enabling precise measurements at low temperatures.

The sample holder consists of three parts of tempered oxygen and hydrogen free

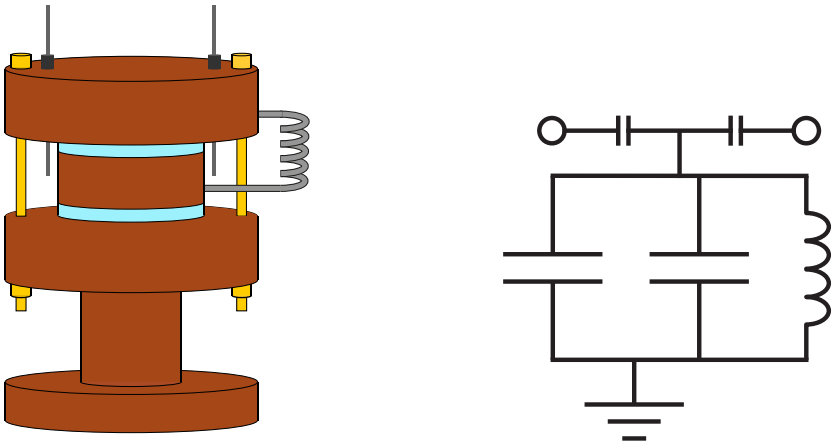

Figure 4.11: Schematic drawing (left) and circuit diagram (right) of the LC resonator used for measurements in the MHz-regime, as developed in [Zei15].

copper. The two outer parts, connected via the brass screws and additionally shorted via another silver plated copper wire, are connected to ground via the experimental platform. The large diameter of the sample holder ensures that the heat transport from the samples to the experimental platform is strong enough for a good thermalization of the sample even at lowest temperatures. The measurement signal is coupled into the resonator via weak capacitive coupling using the antennae shown in the drawing.

Brass disk springs on the screws allow for the compensation of thermal contraction of the samples and ensure a good thermal and electric contact between the samples and the sample holder. The samples themselves are thin glass disks of $d = 0.5\,\mathrm{mm}$ thickness and a diameter of 25 mm, leading to capacitances of 30 pF to 70 pF per sample disk. In order to ensure an even better contact between the samples and the holder, all samples are metalized with a sputtered 200 nm thick gold layer over the whole 24 mm diameter of the sample holder.

As the two capacitors share the middle part of the sample holder as their common high electrode, no additional dielectric is needed in order to electrically separate thermally connected parts. This allows for higher intrinsic quality factors and a higher precision of the experiment. The addition of two capacitors also lowers the

resonance frequency ν_0 of the setup, as

$$\nu_0 = \frac{1}{2\pi\sqrt{LC}} \,. \tag{4.15}$$

Thermal and electric contact between the middle plate and ground is achieved via the coil that consists of 12 windings of the 1.5 mm silver plated copper wire. The part of the wire connecting the coil to the sample holder is several centimeters long and the orientation of the coil is such, that the coupling of its magnetic field into the samples is very weak. With an inductance of $L = (256 \pm 25)$ nH, the resonance frequency ranges from 25 MHz to about 40 MHz, depending on the relative dielectric permittivity of the samples.

4.3.2 Measurement circuit

The resonance of the LC resonator is measured using the HP 8752C[9] network analyzer. It both excites the resonator and reads out the voltage that is coupled out of the resonator. A schematic drawing of the measurement circuit is shown in figure 4.12. The transmitting power of the network analyzer can be varied between −20 and

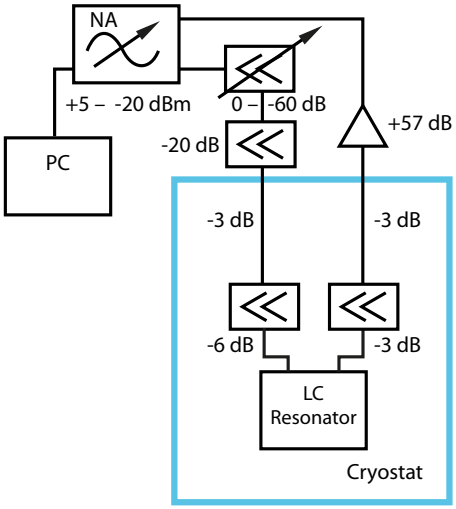

Figure 4.12: Schematic measurement circuit of the MHz setup between the network analyzer (NA) and the LC resonator. The components within the blue box are situated in the cryostat.

5 dBm. For the very small values of excitation power required for the experiment, additional attenuators are used in the measurement circuit: A step attenuator[10] allows a variation of the excitation power over a large range. An additional fixed value attenuator of −20 dB outside the cryostat lets us achieve excitation powers as small

[9] HP 8752C, Hewlett-Packard Company, 3000 Hanover Street, Palo Alto, CA 94304-1185 USA
[10] Step Attenuator AE116-60-01-0N, Weinschel, 5305 Spectrum Drive Frederick , MD 21703 USA

as −100 dBm or even below, considering the very weak capacitive coupling of the resonator to the signal line. The attenuators in the cryostat[11], connected directly to the LC resonator, help dampen possible standing waves in the cables.
Prior to detection the signal that is coupled out of the cryostat is amplified by 57 dB[12].
The step attenuator and variable power output of the network analyzer allow for adaptions of the measurement signal with temperature, thus minimizing heating and nonlinear effects, while allowing good signal to noise ratios.
Both the data acquisition and the temperature are regulated via a LabVIEW program. It continuously sweeps appropriate frequency bands and records the output power, thus creating resonance curves that are then treated further externally.

4.3.3 Data readout

At each temperature step, once the sample is thermalized, resonance curves are averaged in order to increase the precision of the measurement. At high temperatures, where high excitations are possible without negative side effects, only three to five curves need to be averaged, while towards lower temperatures where the excitations are smaller the number of averaged curves is strongly increased.

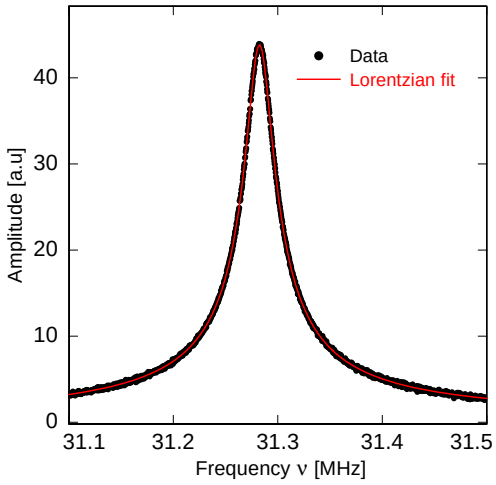

Figure 4.13: Resonance curve of N-BK7 measured at 100 mK and Lorentz curve fit. Data by [Hom15]

[11] All fixed value attenuators are of the type 18AH, Inmet, 300 Dino Drive, Ann Arbor , MI 48103 USA

[12] MiTEQ M/N-AU-4A-0150, L-3 Narda-MITEQ, 435 Moreland Road, Hauppauge, NY 11788 USA

The resonance curves show a Lorentzian line shape

$$L(\nu) = \frac{AQ}{\sqrt{(\nu^2 - \nu_0^2)Q^2 + \nu^2\nu_0^2}} + \left(a\nu^2 + b\nu + c\right) \ , \tag{4.16}$$

that depends on the resonance frequency ν_0 and the quality factor Q of the resonator, as well as the amplitude A of the measurement. The second part of the equation accounts for the background signal that is determined by the whole measurement circuit. An example for a resonance curve with a fit is shown in figure 4.13.

For further treatment of the measured data, we are interested in the dielectric function of the glass samples. Its real part can be obtained from the capacitance of the two parallel plate capacitors with an area A and thickness d via

$$C = 2\varepsilon' \frac{A}{d} \ , \tag{4.17}$$

which is in turn connected to the resonance frequency by the relation given in equation (4.15). The capacitance of the empty resonator ($\varepsilon' = 1$) is $C_0 = 16\,\mathrm{pF}$. The measured capacitance also contains the stray capacitance that was determined to $C_\mathrm{s} = 5\,\mathrm{pF}$ [Zei15], so that the measured capacitance becomes

$$C_\mathrm{meas} = \varepsilon' C_0 + C_\mathrm{s} = \frac{1}{4\pi^2 L\nu_0^2} \quad \Leftrightarrow \quad \varepsilon' = \frac{1}{C_0}\left(\frac{1}{4\pi^2 L\nu_0^2} - C_\mathrm{s}\right) \ . \tag{4.18}$$

This equation is only valid, if the thermal expansion of the sample is negligible. As for the measured samples the relative thermal expansion is at most $\alpha \leq 10^{-5}\,1/\mathrm{K}$, the effect becomes at most $\Delta d/d \leq 0.3\%$ between room temperature and 7.5 mK. It can therefore be neglected.
The relative change of the real part of the dielectric function can now be determined via the resonance frequency of the resonator as given by equation (4.15)

$$\frac{\Delta C}{C} = \left(\frac{\Delta\nu_0^{*2}}{\nu_0} - 1\right) \ . \tag{4.19}$$

Here, ν_0^{*2} is a reference frequency that is usually chosen to be at the maximum value of ν_0, so that the resulting relative change of the dielectric function will always be positive.

The loss tangent of the setup is simply connected to the quality factor of the resonance via

$$\tan(\delta) = \frac{1}{Q} \ . \tag{4.20}$$

Measurements performed on Herasil, which has a loss tangent smaller than 1×10^{-6} at lowest temperatures, have shown that the resonator has an intrinsic loss of $\tan(\delta)_\mathrm{int} =$

7.75×10^{-4} that is mainly determined by the electric loss within the coil. It needs to be subtracted from the measured loss in order to obtain the loss of the sample. Due to this intrinsic loss, changes of the loss tangent of the order of 1×10^{-4} and larger can be resolved with the setup.

4.3.4 Correcting for stray capacitances

Again, we need to take into account the filling factor f of the setup, that is given by equation (4.7). The stray capacitance is again to be assumed parallel to the dielectric filled capacitance, constant in temperature and without loss. We then obtain for the real part of the dielectric function

$$\left(\frac{\Delta\nu_0^{*2}}{\nu_0} - 1\right) = \frac{\Delta C}{C} = \frac{\Delta C_\mathrm{s}}{C_\mathrm{s}}\frac{C_\mathrm{s}}{C} = \frac{\Delta\varepsilon'}{\varepsilon'}\, f \ . \tag{4.21}$$

The loss tangent is determined by

$$\tan(\delta)_\mathrm{meas} = \frac{1}{2\pi\nu_0 RC} = \frac{2\pi\sqrt{LC}}{RC} = \frac{2\pi\sqrt{L}}{R\sqrt{C_\mathrm{d}}}\sqrt{\frac{C_\mathrm{d}}{C}} = \tan(\delta)\,\sqrt{f} \ . \tag{4.22}$$

In contrast to the low frequency measurements, where the filling factor enters as a linear correction in both $\Delta\varepsilon'/\varepsilon'$ and $\tan(\delta)$, its influence is only with $\sqrt{f}$ in the loss tangent of the LC resonator. As the quality factor and thereby the loss tangent is measured at the resonance frequency, which is in turn dependent on the capacitance, measuring with a resonator setup leads to a different correction of stray capacitances when compared to fixed frequency measurements using capacitance bridges.
As C_p is only about 5 pF and the two parallel plate capacitors have a combined capacitance of 60 pF even when filled with Herasil, the filling factor is at least 0.90 for all measured samples and only a small correction.

4.3.5 Electric fields and power input in the sample

In order to avoid both heating and nonlinear driving of the samples, the applied power at the sample has to be chosen as low as possible, while still allowing for good signal to noise ratios. This becomes most relevant at lowest temperature.
The samples have a size of $A = 4.8\,\mathrm{cm}^2$, leading to input powers P between $260\,\mathrm{pW/cm}^2$ at $-59\,\mathrm{dBm}$ and $260\,\mathrm{fW/cm}^2$ at $-89\,\mathrm{dBm}$. With a sample thickness of $d = 0.5\,\mathrm{mm}$ and a relative dielectric constant $\varepsilon_\mathrm{r} \approx 6$, a quality factor of $Q \approx 1000$ and a frequency of $\nu \approx 30\,\mathrm{MHz}$, we find that the electric field in the samples

$$F = \sqrt{\frac{PQ}{Ad\varepsilon_0\varepsilon_\mathrm{r}2\pi\nu}} \ , \tag{4.23}$$

range between 1 V/m and 50 V/m, so we are far below the 2 kV/m reached in the low frequency setup.
The calculations made above do not yet take into account the weak coupling of the setup. As the small antennae radiate homogeneously in all direction, only a small portion of the power they radiate is coupled into the LC circuit. The values given above can thus be only an upper limit of the actual values in the sample.

As is shown in figure 4.14, a change of the applied power does not change the

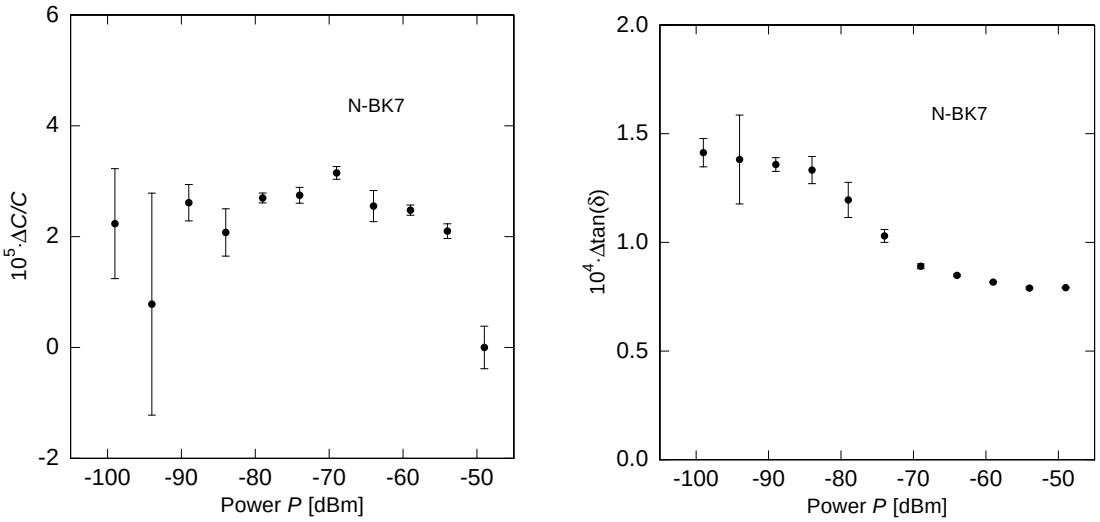

Figure 4.14: Influence of the input power P applied to the sample on the capacitance $\Delta C/C$ (left) and the loss tangent $\Delta \tan(\delta)$ (right) of N-BK7 at a temperature of 20 mK and a frequency of 30 MHz [Hom15].

real part of the dielectric function of N-BK7 within the margin of error at 20 mK. The loss tangent $\tan(\delta)$, however, is constant at high powers, then shows a clear rise towards lower powers and settles at a new plateau value at low powers. This is due to the very strong excitation dependence of the resonant loss., which is much larger than that of the relaxational contribution.
For low temperatures, measurements on this sample were therefore conducted at -89 dBm, while at temperatures above 100 mK a power of -59 dBm could be used without effects on either $\delta\varepsilon'/\varepsilon'$ or $\tan(\delta)$.
Similar measurements were performed on all samples and appropriate input powers were chosen accordingly.

4.4 Measurement setup for GHz measurements

Similar to the measurements in the MHz regime, those in the GHz regime were performed using an LC resonator. The higher frequency necessitates the use of a different setup both for the resonator and the signal creation and path, both of which will be described below.

4.4.1 LC Resonator

While the resonator for MHz measurement is a classic LC resonator with separate coil and capacities, the one used in the GHz range is a so called $\lambda/4$ reentrant cavity circuit. A schematic drawing of a cut through the resonator used in the course of this thesis is shown in figure 4.15. It is built out of gold plated copper and has a res-

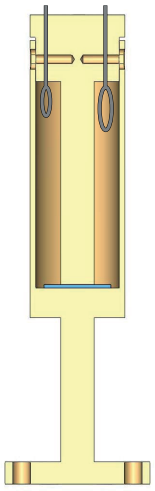

Figure 4.15: Schematic drawing of a cut through the LC resonator used for measurements in the GHz regime. The sample, shown in blue, is at the location of the high electric field.

onance cavity of about 42.5 mm height and is 18 mm in diameter, the inner rod has a diameter of 8 mm. The signal is inductively coupled into and out of the system via coupling loops at the top of the resonator and excites an electromagnetic standing wave. The resulting magnetic field is maximal at the top of the resonator, while the electric field in this transversal magnetic mode is maximal and most homogenous at the gap at the bottom. Even here, its strength is only a few V/m at the excitations used in this thesis, so no nonlinear effects should occur.
Due to the oscillation of the electromagnetic field energy, the reentrant cavity resonator can be seen as an oscillating LC circuit where the cylinder walls, the rod and the loops act as the inductor while the gap acts as the capacitor. As the magnetic field runs parallel to the cavity walls, the coupling strength of the loops can be adjusted by simply orienting them more or less perpendicular to the field. For the dielectric measurements performed in this thesis, a weak coupling is desired in order

to maximize the quality factor of the resonator and not dampen it via the measurement circuit, so the loops are turned parallel to the cavity walls. A further decrease in the coupling was not necessary, as the quality factor was limited by ohmic loss due to induced currents in the resonator [Wes15] when using the coupling loops.
The rod in the middle of the resonator is connected to the lid so that thermal extensions of the resonator are compensated and the size of the small gap with the sample remains the same from room temperature down to the millikelvin range. The sample itself is a small square glass plate of $12\,\mathrm{mm}^2 \times 12\,\mathrm{mm}^2$ size and a thickness of 0.5 mm, that is pressed down by the rod and thermally attached with a small amount of vacuum grease.

4.4.2 Measurement circuit

The measurement circuit of the GHz setup is shown schematically in figure 4.16. The signal generator[13]creates an amplitude modulated carrier signal.

The carrier signal V_{car} corresponds to the measurement frequency $\nu \approx 0.85 - 1\,\mathrm{GHz}$

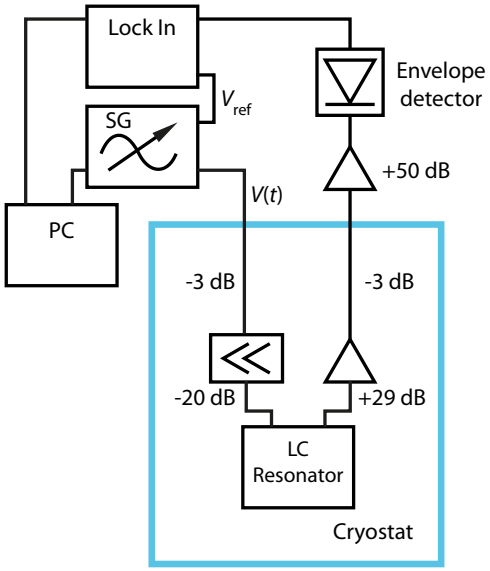

Figure 4.16: Schematic measurement circuit of the GHz measurement setup between the signal generator (SG) and the LC resonator. The components within the blue box are situated in the cryostat.

and is modulated with a 1 kHz signal. The modulation ratio between the carrier amplitude A_{car} and the modulation amplitude A_{mod} is at 80%. This envelope signal is directly sent to a LockIn amplifier[14] where it serves as a reference signal.
The modulated voltage $V(t)$ is also sent into the cryostat with an amplitude of

[13]Signal generator 100 kHz–2 GHz SMH, Rhode und Schwarz, Mühldorfstrasse 15, 81671 München, Germany

[14]SR830, Stanford Research Systems, Inc., 1290-D Reamwood Avenue, Sunnyvale, CA 94089, USA

$P_{\text{in}} = -50\,\text{dBm}$. There, it is dampened by $-20\,\text{dB}$ by an attenuator that is thermally coupled to the heat exchangers of the cryostat, thus minimizing thermal noise input to the resonator via the cables. The signal is then coupled into the resonator via the coupling loop, that is simply soldered on the inner part of a coaxial cable. After coupling out of the resonator, the signal is amplified by 28 dB using a low temperature HEMT amplifier[15] and by a further 50 dB at room temperature.
Finally, an envelope detector consisting of a germanium diode[16] and a low pass filter demodulates the signal and passes it to the LockIn amplifier, where it can be compared to the reference signal.
As the resonator changes the amplitude of the carrier signal, the amplitude of the modulation signal changes as well and by analyzing the latter, the resonance frequency and the quality factor of the resonator can be measured indirectly.

4.4.3 Data readout

Just like in the case of the MHz resonator, frequency sweeps are conducted with the setup, leading to Lorentzian shaped resonance curves. The evaluation of the curves is also conducted similar to the MHz case as described in section 4.3.3.
Again, the determination of both the filling factor and the intrinsic loss of the setup is needed in order to correct the measured quantities. The intrinsic loss of the system was determined to $\tan(\delta)_{\text{int}} = 8.33 \times 10^{-4}$ in [Wes15].
The filling factor of the setup could not be measured directly, as it largely depends on the exact spacing between the resonator body and the rod. As the temperature dependent behavior of $\Delta\varepsilon'/\varepsilon'$ should be the same for all frequencies at high temperatures, the curves were adjusted to match the slopes of the MHz and low frequency measurements above about 6 K. The thus determined filling factor is about $f \approx 0.5$ for both HY-1 and N-KZFS11 [Hau15, Wes15]. Similar resonators were shown to have filling factors of 0.45 [Ens91] and 0.7 [Wei95].

4.5 Measured samples

Within the course of this thesis, samples of four different glass types were measured: The pure quartz glass Herasil and the multicomponent glass N-BK7 served as reference materials, while the multicomponent glasses N-KZFS11 and HY-1 were used to determine possible influences of large nuclear quadrupole moments on the dielectric

[15] LNA BB 1020 A-COOL, KUHNE electronic GmbH, Scheibenacker 3, 95180 Berg / Oberfranken, Germany

[16] AA118, New Jersey Semi-Conductors Products, Inc., 20 Stern Ave., Springfield, New Jersey 07081, USA

Parameter	Unit	Herasil[a]	N-BK7[b]	N-KZFS11[c]	HY-1[d]
T_G	°C	1180	557	551	590
ρ	g/cm^3	2.20	2.51	3.20	3.19
α	10^{-6}/K	0.3	7.1	6.6	102
ε_r		3.7	5.6[e]	8.5[e]	6.1[e]
$P_0 p_0^2$	10^{-13}C/J m^2	0.06[e]	1.3[f]	3.5[e]	5.6[e]
v_l	m/s	5800[g]	6000[g]		
v_t	m/s	3800[g]	3800[g]		

Table 4.1: Material properties of the samples: Glass temperature T_G, density ρ, coefficient of thermal expansion α, relative dielectric constant ε_r, dielectric density of states $P_0 p_0^2$ and longitudinal and transversal sound velocity v_l and v_t. Data taken from [a][Her10], [b] [Sch07], [c] [Sch14], [d] [Hoy16a], [e] this Thesis, [f] [Woh01a] and [g] [Hun76].

Herasil	OH^-	Al	Ca	Li	Na	Ti	Fe	K
	150	20	1	1	1	1	0.8	0.8

Table 4.2: Trace elements in the quartz glass Herasil 3 in ppm. Data from [Her10], trace amounts of equal or less than 0.1 ppm were neglected.

properties of glasses at low temperatures. An overview over their properties is given in table 4.1.

The samples of the quartz glass Herasil were used used to test both the newly developed low frequency and MHz measurement setups [Luc11, Zei15]. It contains only traces of other constituents than SiO_2, as given in table 4.2. The main dielectric signal needed for the measurements comes from the OH^- ions in the glass, as was shown in figure 2.7. Their concentration in Herasil is very low, so the measured dielectric density of states $P_0 p_0^2$ is almost two orders of magnitude smaller than in the other measured samples.

Quartz glass like Herasil or Suprasil has, however, often been used as a standard glass in previous measurements [vS76, Fro77, Esq92, vR98, Cla00, Las78]. The results obtained on the new measurement setups can therefore easily be compared to the old measurements, allowing a check of their validity. The low signal also sets a boundary on the precision that can be obtained in the measurement setups.

N-BK7	SiO_2	Na_2O	B_2O_3	K_2O	BaO	Al_2O_3	
	74.8	10.1	9.6	4.7	0.76	0.03	
	Si	Na	B	K	Ba	Al	O
	24.9	6.8	3.8	3.1	0.38	0.01	60.9

Table 4.3: Composition of the borosilicate glass N-BK7 in molar and atomic percents [Lud03].

HY-1	SiO_2	Na_2O	BaO	Ho_2O_3	B_2O_3	Sb_2O_3	
	74	18	3.4	1.2	3.8	0.1	
	Si	Na	Ba	Ho	B	Sb	O
	25	12	1.7	0.5	1.5	0.03	60

Table 4.4: Composition of the glass HY1 in molar and atomic percents[17]all values are known with a relative error of ±2 % of the given values. The boron oxide content could not be measured directly but was approximated using [Hoy16b].

The multicomponent glass N-BK7 used for additional reference measurements in the MHz range is also a widely used sample. Not only dielectric [Bec90, Rog97b, Woh01a] measurements have been performed on the glass, but it has also been used to study the interaction between tunneling systems [Arn75, Nal04] and to measure the polarization echoes [Lud03, Bur13]. As is shown in table 4.3, it contains no elements with large quadrupole moments.
The two main constituents apart from SiO_2, that carries no nuclear quadrupole moment, are Na_2O and B_2O_3, which both contain quadrupole carrying nuclei with frequencies given in table 3.1. Comparisons both to the pure quartz glass to determine possible influences of the higher dielectric density of states $P_0 p_0^2$ and possible effects stemming from the small nuclear quadrupoles and to the other multicomponent glasses in order to better distinguish influences of their elements with large nuclear quadrupoles, are therefore intriguing.

The main focus of this thesis lies on the possible influence of elements with large nuclear quadrupoles on the dielectric function of glasses. Two different glasses were chosen, containing significant amounts of Ho_2O_3 in the case of HY-1 and TA_2O_5 in the case of N-KZFS11. Both glasses are fabricated on an industrial scale by Hoya Optics and Schott respectively and used for optical precision measurements, ensuring a constant and high quality of the sample materials.

N-KZFS11	SiO_2	Na_2O	B_2O_3	ZrO_2	Ta_2O_5	Nb_2O_5	ZnO	
	40	16	25	12.6	5.1	0.3	0.8	
	Si	Na	B	Zr	Ta	Nb	Zn	O
	13	11	9.8	4.2	1.5	0.1	0.4	60

Table 4.5: Composition of the glass N-KZFS11 in molar and atomic percents[18], all values are known with a relative error of ±10 % of the given values. The boron oxide content could not be measured directly but was approximated using [Sch15].

The glass HY-1 usually serves as a calibration filter for lasers, having very narrow absorption lines in the visible spectrum. Apart from the main constituents SiO_2, Na_2O and B_2O_3, it contains about one molar percent of Ho_2O_3 and three percent of BaO. Its high content of dielectrically active materials, leading to a high $P_0 p_0^2$, make dielectric measurements on the glass easy to perform even at low excitation voltages or powers. It should be noted, that holmium not only has a nuclear quadrupole moment, but also a very strong magnetic moment and spin-orbit coupling. The magnetic properties holmium aluminosilicates have been measured at low temperatures [Cha80]. No dielectric measurements have been reported, but microwave experiments in the MHz-range were conducted on holmium aluminosilicates with various holmium concentrations between 1.5% and 10% were conducted in [Ler84, Ler87]. These measurements allow for an estimation of concentration dependent effects in this class of materials.

The special short flint glass N-KZFS11 produced for optical precision molding, contains about five molar percent of Ta_2O_5, as well as more than ten percent of ZrO.
As tantalum has no magnetic moment due to its shell, and is a network former while holmium is an intermediate oxide, the different electromagnetic environments of the two elements might lead to different effects in the low temperature dielectric properties of N-KZFS11 and HY-1. A comparison of the two glasses therefore might help in discerning different nuclear related mechanisms in glasses at very low temperatures. The content of elements with medium to large nuclear quadrupole moments in N-KZFS11, given in 4.5, is thus even higher than in HY-1, while it has a similar amount of dielectrically active components. First measurements of the low temperature dielectric properties of N-KZFS11 were conducted in [Kin08, Däh10, Luc11] and now continued in this thesis.

[17]Measured by Meyer and Varychev, Geologisches Institut, Heidelberg University
[18]Measured by Meyer and Varychev, Geologisches Institut, Heidelberg University

5. Experimental Results

In this chapter, we will present the experimental results obtained within this thesis using the different measurement setups described in the previous chapter. First we will discuss the thermalization of the two samples that contain very large nuclear quadrupole moments at very low temperatures. We then turn to dielectric measurements with the focus on the low frequency dielectric properties of different glasses. In particular, we will contrast the behavior of glasses with and without large nuclear quadrupoles and will develop a new understanding of the impact of nuclear moments on the dielectric properties of glasses at low temperatures.

5.1 Thermalization measurements

As it was shown in previous investigations [Kin08, Däh10], that the measured sample N-KZFS11 appears to have a much larger specific heat than other glasses, thermalization measurements were performed for all samples, in order to see whether they reach thermal equilibrium at very low temperatures in the experiments discussed here. All temperature dependent measurements of $\Delta\varepsilon'/\varepsilon'$ and $\Delta\tan(\delta)$ were conducted in temperature steps of 10 %, with continuous measurements of the dielectric function. An equilibrium of the sample and the heat bath of the cryostat is reached, once the measurement variables show no more time dependence.

Examples of such measurements on N-KZFS11 performed at 120 Hz are shown in

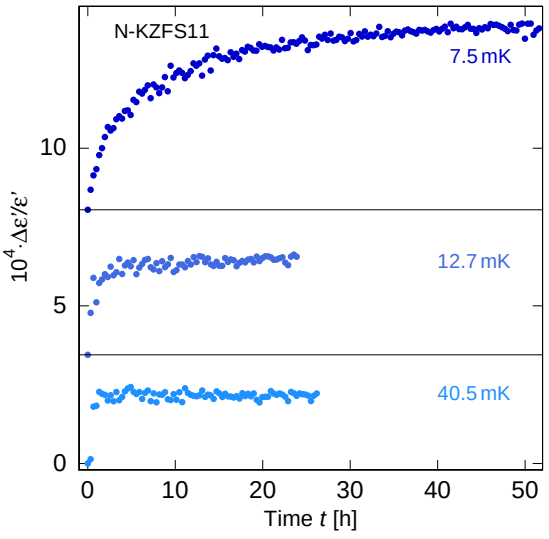

Figure 5.1: Time evolution of the change of the real part of the dielectric function $\Delta\varepsilon'/\varepsilon'$ of N-KZFS11 after temperature steps of 10 % at three different temperatures taken at 120 Hz.

figure 5.1 for three different temperatures. It is clearly visible, that at temperatures of 40 mK and above the sample thermalizes within less than an hour. At a temperature of 12.7 mK, the thermalization time has increased to about three hours and becomes clearly visible in the data. Towards even lower temperatures, the thermalization times increase drastically, the data still showing a clear drift after fifty hours at 7.5 mK. Similar effects were also observed in HY-1.
As described in section 4.2.3, the low frequency setup was designed to provide a very good thermal coupling of the sample. Indeed, in N-BK7 and Herasil the thermalization times stayed below two hours for all temperatures in all three measurement setups. Since the thermal coupling of the different samples can be assumed to be very similar, the long thermalization times therefore indicate a very large heat capacity of the samples HY-1 and N-KZFS11.
In order to further analyze this behavior at low temperatures a fit assuming exponential convergence of the sample towards the bath temperature leading to a change of the capacitance of $C(t) = C_T(1 - a\ \exp(-\tau_{\mathrm{th}}/t))$ was performed at each temperature step. The thermalization time constants τ_{th} of HY-1 and N-KZFS11 extracted from these fits are shown in figure 5.2, with the thermalization times of N-BK7 as a reference for both samples.

The temperature dependence of the thermalization times τ_{th} can be fit using equa-

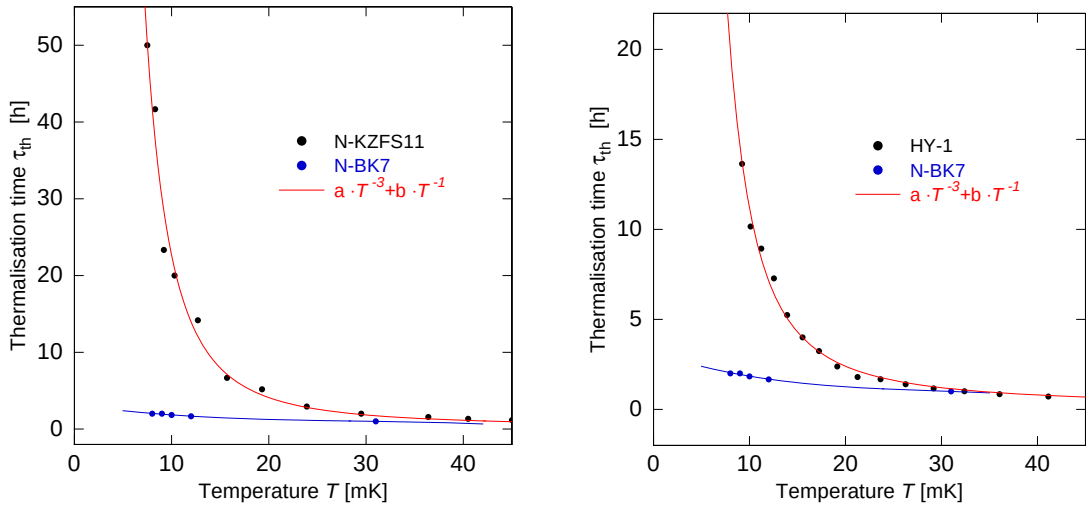

Figure 5.2: Thermalization times of N-KZFS11 (left) and HY-1 (right) below 50 mK and fits calculated using equation (4.6). The thermalization times of N-BK7 that are shown for comparison in both figures were measured in [Hom15] with a similar setup.

tion (4.6) that describes the thermalization assuming the Kapitza resistance between the samples and the metalized layer, proportional to T^3, and the heat transport via gold bonds linear in T. The contribution of the thermalization within the glass sample was assumed to be negligible. As can clearly be seen in figure 5.2, the fits describe

the data very well, allowing for the determination of the samples' heat capactiy.
As the total heat capacitance C_V of the sample is connected to the thermalization time via the thermal conductance G, we can extract an approximate molar heat capacitance c_V from the fits via

$$\tau = \frac{C_V}{G} = \frac{c_{V,\mathrm{K}}}{nG_\mathrm{K}} + \frac{c_{V,\mathrm{el}}}{nG_\mathrm{el}} \,. \tag{5.1}$$

Here, n is the number of atomic moles in the sample calculated from the sample size, the density and mean atomic masses are taken from tables 4.4 and 4.5. The electronic conductances were given by the number of gold bonds used, 12 for HY-1 and 18 for N-KZFS11. As both the Kapitza resistance and electronic conductance are not precisely known, $c_{V,\mathrm{K}}$ and $c_{V,\mathrm{el}}$ are used as independent fit parameters, giving an estimate of the uncertainty of this rough approximation.

Measurements of the heat capacity on other glasses show a linear temperature dependence in the two-level tunneling regime, as was already discussed in section 2.2. In stark contrast to this, the heat capacity of bot HY-1 and N-KZFS11 appears to be almost constant between 7.5 mK and 50 mK. The absolute values deduced from the thermalization times are

$$c_V(\text{HY-1}) = 0.47 \pm 0.01 \mathrm{J/mol\,K} \qquad c_V(\text{N-KZFS11}) = 0.95 \pm 0.05 \mathrm{J/mol\,K} \,, \tag{5.2}$$

which for both samples is of the order of $2-5\%$ of the $3R = 25\,\mathrm{J/mol\,K}$ that are given by the law of Dulong-Petit and more than seven orders of magnitude larger than the value of $c_V(\text{N-BK7}) = 2 \times 10^{-7}\,\mathrm{J/mol\,K}$ that was measured in N-BK7 at 10 mK [Hal12].
This means, that in addition to phonons and tunneling systems, we see a very large contribution to the specific heat in the two samples, that is not present in other glasses. As HY-1 and N-KZFS11 both contain nuclei with very large nuclear quadrupole frequencies, the assumption that these nuclei are the source of the unknown heat capacity is rather natural. A large contribution to the specific heat of about $3R$ has been observed in the crystal $Ho_3Al_5O_{12}$ at a temperature of 220 mK and has been attributed to electric quadrupole ordering [Nag01]. This further backs the notion of a nuclear heat capacity due to the quadrupole carrying elements in the two glasses HY-1 and N-KZFS11.

5.2 Dielectric measurements of the standard glasses Herasil and N-BK7

In this section we will discuss the low temperature dielectric properties of the two standard glasses Herasil and N-BK7. The measurements serve as a reference to those performed in the two glasses containing large nuclear quadrupole moments, that were measured in the same setups. This will allow us to better investigate the influence of the nuclear quadrupole moments on the dielectric properties of glasses at low temperatures. We will here very briefly discuss the results of the measurements performed on Herasil and then turn to those on N-BK7 in more detail.

Figure 5.3 shows the change of the real part of the dielectric function up to 10 K

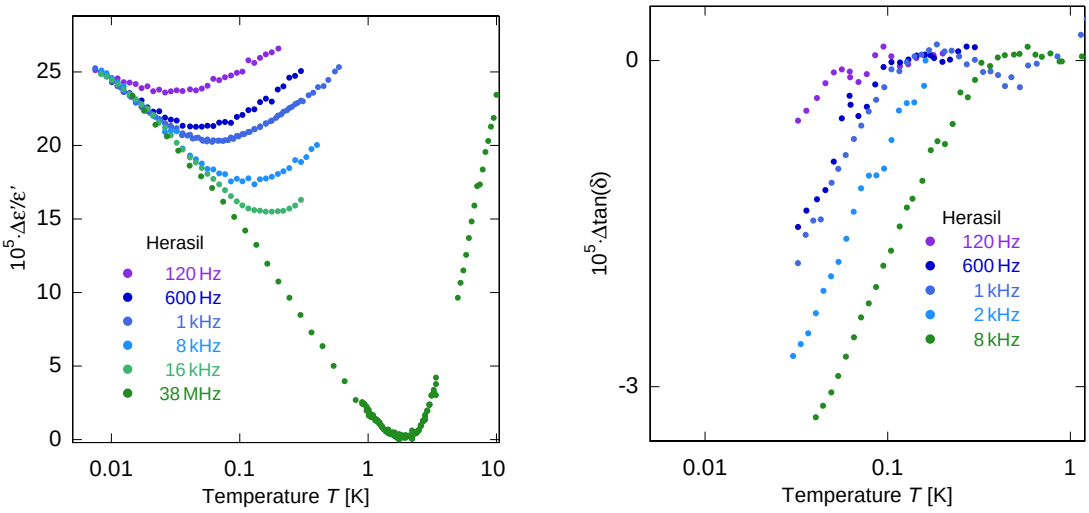

Figure 5.3: Change of the real part of the dielectric function $\Delta\varepsilon'/\varepsilon'$ (left) and the loss tangent $\Delta\tan(\delta)$ (right) of Herasil as a function of temperature between 10 mK and 10 K at frequencies between 120 Hz and 38 MHz. Data at 38 MHz from [Zei15]

and the change of the loss tangent up to 1 K. As expected, all curves in $\Delta\varepsilon'/\varepsilon'$ follow a common resonant slope at low temperatures and then rise after a frequency dependent minimum towards high temperatures. The resonant slope, however, is not straight but flattens off somewhat towards lowest temperatures at all frequencies. This leads to a slope ratio of $-1:1$ rather than $-2:1$ in the one phonon dominated regime of the low frequency curves, an observation that has, as mentioned before, already been made in various other glasses.

The measurement performed at 38 MHz show a steeper high temperature slope and a narrower minimum, indicating the onset of the two phonon relaxation at temperatures only slightly above the minimum. This can be easily seen, when the position of the minima is plotted against frequency in a double logarithmic plot, as shown

in figure 5.5. The $\nu^{1/3}$ shift of the minima then shows as a straight line, its offset determined by the coupling strength of the phonons to the tunneling systems.
The loss tangent of Herasil shows the common plateau region for all low frequency measurements, as well as the expected decrease of the loss tangent with T^3 towards lowest temperatures. The onset of the decrease is frequency dependent, as expected from the standard tunneling model.

Similar to the quartz glass Herasil, many low temperature measurements have already been conducted on the multicomponent glass N-BK7. The results of dielectric low frequency measurements from previous works [Woh01a, Bec90, Kin08] , alongside high frequency data measured in [Hom15], are shown in figure 5.4.

The low frequency data of the change of the real part of the dielectric function is

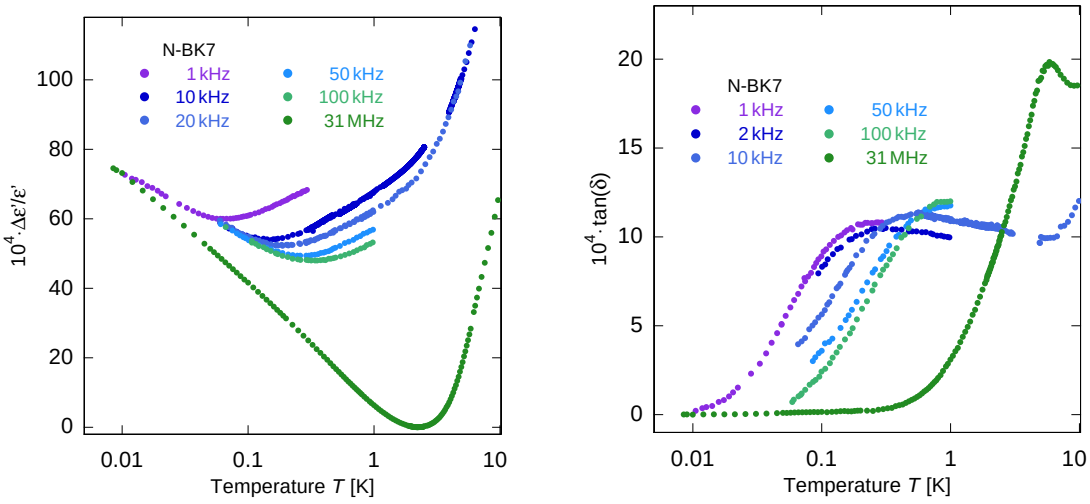

Figure 5.4: Change of the real part of the dielectric function $\Delta\varepsilon'/\varepsilon'$ (left) and loss tangent $\tan(\delta)$ (right) of N-BK7 as a function of temperature between 10 mK and 10 K at frequencies between 1 kHz and 31 MHz. Data from [Woh01a, Bec90, Kin08, Hom15].

aligned to match on the common resonant slope at low temperatures. It shows the decreased slope ratio of about $-1:1$ instead of $-2:1$ in the one phonon regime, that is also present in Herasil. The onset of the two phonon process is again nicely visible by the increased slope above about 2 K.
Very surprisingly, the data measured at 31 MHz shows a distinctly steeper resonant slope than the low frequency data, a feature that could not be observed in the measurements performed on Herasil, as shown in figure 5.3.
While the modifications of the standard tunneling model proposed in chapter 2 often change the low temperature slope, they always do so uniformly for all frequencies. The discrepancy must therefore stem from an yet unexplained effect influencing small frequencies more than high ones. As it does not show up in the measurements per-

formed on Herasil, it might be due to the chemical composition of the multicomponent glass, that contains elements with nuclei carrying electric quadrupole moments. The loss tangent shows the frequency dependent rise with T^3 from low temperatures to the plateau at high temperatures. The plateau region in the low frequency data is not completely flat but slightly slopes down towards high temperatures, as one would expect when assuming a restricted distribution of the tunneling splitting. An onset of thermal activation at about 6 K is seen in the 10 kHz measurements. The 31 MHz, however, curve not only goes up to much larger values than the low frequency data but also shows a peak at 6 K rather than a plateau region.

In order to better discriminate between possible causes for the deviations of the

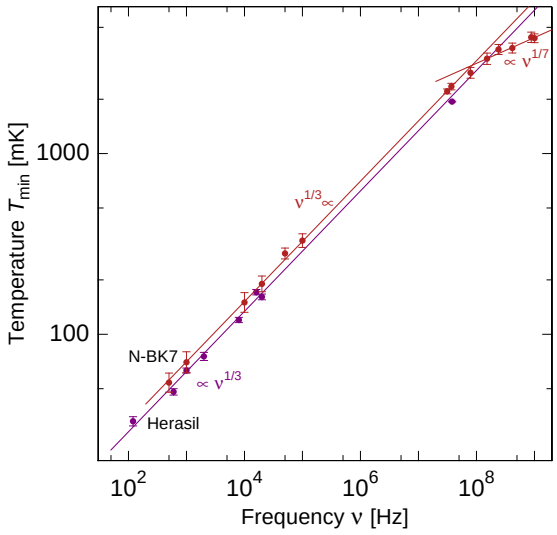

Figure 5.5: Temperature of the minimum in the real part of the dielectric function $T_{\min}$ of Herasil (dark red) and N-BK7 (red) as a function of frequency. The expected $\nu^{1/3}$ dependence for one phonon relaxation and $\nu^{1/7}$ dependence for the two phonon relaxation are shown as solid lines. Data of N-BK7 at 500 Hz from [Rog97a], between 30 MHz and 1 GHz from [Fre16].

measured data from the standard tunneling model, we have plotted the temperature of the minimum $T_{\min}$ in $\Delta\varepsilon'/\varepsilon'$ for all measured frequencies of Herasil and N-BK7 in figure 5.5. As already shown in section 2.3.5, the frequency dependence of the minimum directly shows the temperature dependence of the dominant relaxation mechanism. This allows us to reliably determine the dominant relaxation mechanisms in a glass even without using the means of elaborate numeric calculations.
As we can see, both Herasil an N-BK7 are dominated by the expected one phonon process over five orders in frequency up to about 30 MHz, shown by the shift of $T_{\min}$ with $\nu^{1/3}$. The very similar coupling strengths for one phonon relaxation in the two glasses lead to two parallel lines in the data, that lie very close together. Above about 30 MHz, the two phonon process becomes dominant, leading to a $\nu^{1/7}$ dependence of $T_{\min}$. This confirms the two phonon process as the cause of the narrower minimum in $\Delta\varepsilon'/\varepsilon'$ at high frequencies seen in figures 5.3 and 5.4. The thermal excitation seen in the two figures as a rise in the loss tangent is not yet visible in the shift of $T_{\min}$, as it will only dominate its position at even higher frequencies.

We have shown that the dynamic behavior of the two standard glasses Herasil and N-BK7 is completely governed by one and two phonon relaxation between 7.5 mK and several kelvin, where thermally activated processes become relevant. The deviations from the standard tunneling model observed in the data must therefore, at least in large parts, stem from a modified distribution function of the tunneling two-level systems. We will therefore compare the curves obtained using two modifications of the distribution function, namely a Gaussian in the tunneling parameter λ as introduced in section 2.4.2 and the dipole gap in the distribution caused by long range interaction as described in section 2.4.3, to the measured data of N-BK7. This will later help us discriminate between effects due to similar distributions and those due to a change in the system's dynamics in the glasses HY-1 and N-KZFS11.

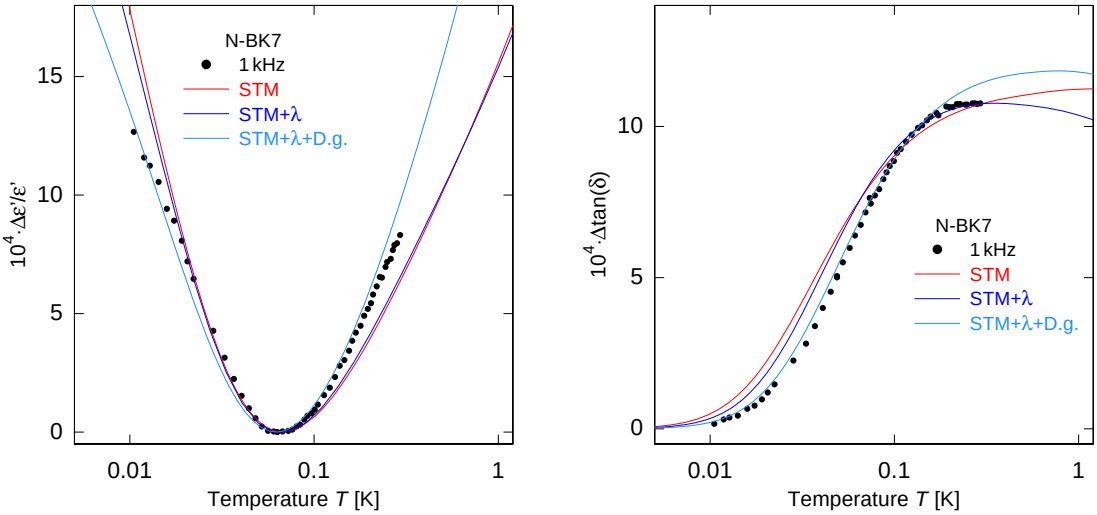

Figure 5.6: Change of the real part of the dielectric function $\Delta\varepsilon'/\varepsilon'$ (left) and the loss tangent $\Delta\tan(\delta)$ (right) of N-BK7 as a function of temperature between 10 mK and 250 mK at a frequency of 1 kHz. Numeric calculations based the standard tunneling model including appropriate changes of the distribution function are drawn as solid lines. Data from [Woh01a].

For the modifications of the distribution function considered here, we have used the values obtained for the restriction of the tunneling parameter λ of Suprasil [Bec90] and the so called dipole gap in the distribution due to long range interaction with $P_0U_0 = 1.5 \times 10^{-3}$ measured in [Nat98] on N-BK7. The long range interaction alone leads to a rise of the high temperature plateau of the loss tangent towards high temperatures, which is not observed in the data. Numeric calculations including this effect therefore always also include a restricted distribution of tunneling parameters to counteract the effect on the high temperature plateau region.

Figure 5.6 shows the measured data and the numeric calculations, where the unmodified standard tunneling model is drawn in red, the calculations including a Gaussian in λ are shown in dark blue and those including both a Gaussian in λ and the dipole gap in the distribution are drawn in light blue. All calculation parameters were chosen so the resulting curves fit the minimum region in $\Delta\varepsilon'/\varepsilon'$, the parameters used for for the fits are given in A.1. The same parameters were used for all three frequencies discussed below.
While none of the distributions of parameters included in the numeric calculation leads to a perfect description of the data, we see that the light blue curve shows a slope ratio of $\Delta\varepsilon'/\varepsilon'$ very close to the observed $-1:1$. Both restrictions of the distribution function also show a decrease of the plateau in the loss tangent towards higher temperatures.

As the measurements performed at 10 kHz extend to higher temperatures, we can

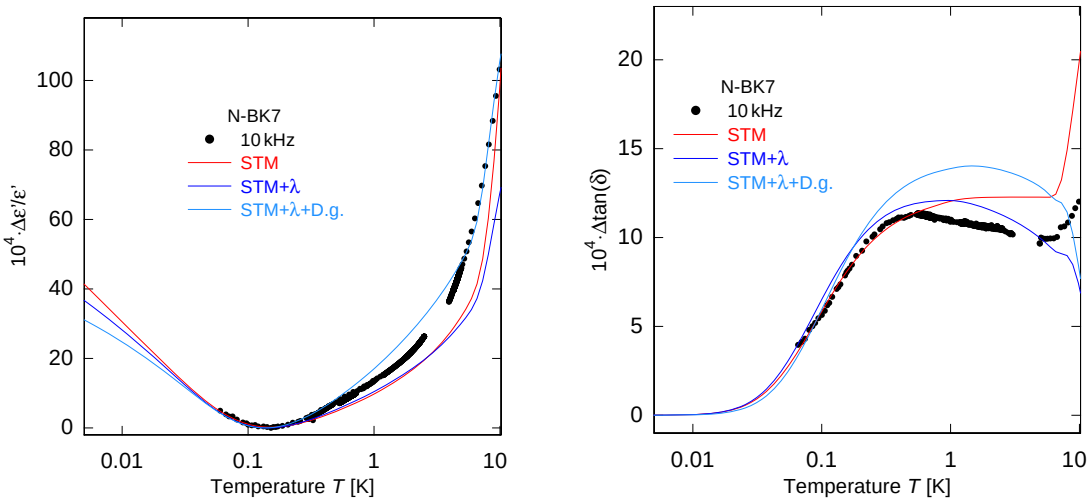

Figure 5.7: Change of the real part of the dielectric function $\Delta\varepsilon'/\varepsilon'$ (left) and the loss tangent $\Delta\tan(\delta)$ (right) of N-BK7 as a function of temperature between 50 mK and 10 K at a frequency of 10 kHz. Numeric calculations based the standard tunneling model including appropriate changes of the distribution function are drawn as solid lines. Data from [Bec90, Kin08].

better compare the influence of modified distributions to the data in this temperature range in figure 5.7. The inclusion of thermally activated processes in the numeric simulations leads to the rise of the loss tangent at temperatures above 6 K, seen well in the red curve. The strong reduction of states in the modified distributions leads to a suppression of this rise, showing that the actual distribution of parameters in N-BK7 must be broader than assumed here. The biggest discrepancy between the calculations and the data is seen in the two phonon relaxation regime, where the data's slope is less steep than that of the model. Again, this points to a broader

distribution than assumed in the calculations. The same is true for the two phonon regime in the real part of the dielectric function, where we see deviations, while the one phonon and thermally activated regime are well described by the doubly modified distribution function.

Finally, the numeric calculations were compared to the data measured at 31 MHz,

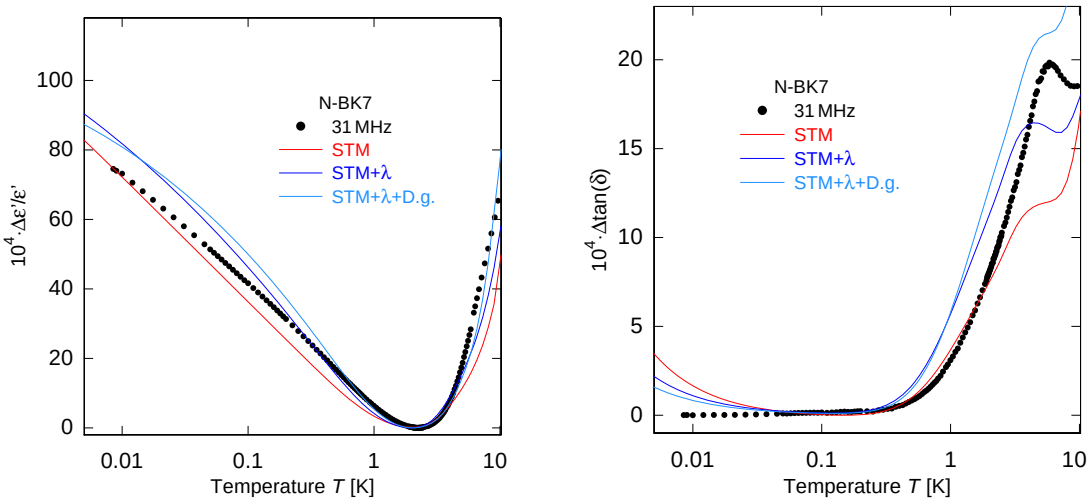

Figure 5.8: Change of the real part of the dielectric function $\Delta\varepsilon'/\varepsilon'$ (left) and the loss tangent $\Delta\tan(\delta)$ (right) of N-BK7 as a function of temperature between 10 mK and 10 K at a frequency of 31 MHz. Numeric calculations based the standard tunneling model including appropriate changes of the distribution function are drawn as solid lines. Data from [Hom15].

with the results shown in figure 5.8. As we can see, the different restrictions to the distribution of parameters both lead to the increase in the loss tangent when compared to the low frequency plateau value and the maximum around 6 K observed in the data.

With the given modifications of the standard tunneling model's distribution, no parameter set could be found that describes the data from low to high frequencies over the entire temperature region equally well. Still, by including rather simple modifications to the distribution function like a Gaussian distribution of the tunneling parameter λ and the dipole gap, we can already explain many deviations from the pure standard tunneling model. The decreased slope ration in $\Delta\varepsilon'/\varepsilon'$ as well as the slope in the high temperature plateau of $\Delta\tan(\delta)$ and the strongly increased plateau value at high frequencies must be due to a modified distribution of the parameters close to the combination shown here in numeric calculations.
Only the different resonant slope between the low frequency and the megahertz regime remains puzzling. As it is most probably not caused by a modification of the

distribution function, its root must lie in a dynamic process that affects low frequencies more than high ones but is not strong enough to dominate over the phononic relaxation.

5.3 Dielectric measurements of HY-1

In order to investigate the influence of large nuclear quadrupoles on the dielectric properties of glasses at low temperatures, we have performed measurements on the glass HY-1. As described in sections 3.4 and 4.5, HY-1 contains about 0.5 % of holmium atoms, that have a nuclear quadrupole frequency in the high megahertz range. The effects of any nuclear quadrupole driven effects should therefore be very large in this sample.

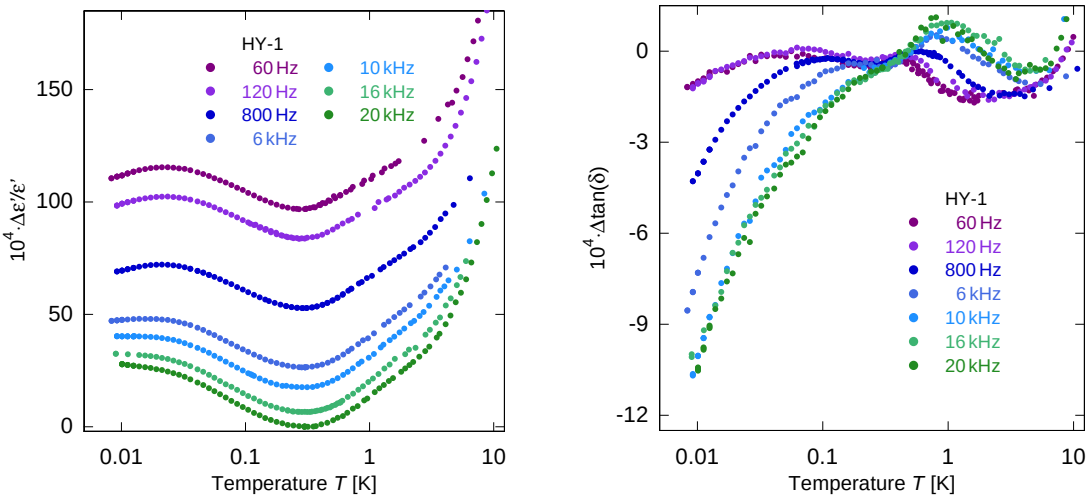

Figure 5.9: Change of the real part of the dielectric function $\Delta\varepsilon'/\varepsilon'$ (left) and the loss tangent $\Delta\tan(\delta)$ (right) of HY-1 as a function of temperature between 8.3 mK and 10 K at frequencies between 60 Hz and 20 kHz.

Figure 5.9 shows the change of the dielectric function of HY-1 between 8.3 mK and 10 K in the low frequency regime from 60 Hz to 20 kHz. Even at first glance, the measurements look strikingly different from those performed on Herasil and N-BK7. Instead of being frequency dependent, the minimum in $\Delta\varepsilon'/\varepsilon'$ does not shift in temperature with the measurement frequency but is constant over the whole frequency range depicted here. It lies at approximately 300 mK, much higher than the minima observed in the other two glasses in the same frequency range, as was shown in figure 5.5.

Even more surprising is the low temperature behavior of the data, that shows a maximum around 15 mK at the lowest frequencies. The height of this maximum decreases with increasing frequency, until only a decrease in the slope of $\Delta\varepsilon'/\varepsilon'$ towards lowest temperatures remains at frequencies larger than 6 kHz. This behavior of the higher frequencies looks similar to the plateau in $\Delta\varepsilon'/\varepsilon'$ due to a pseudo gap in the parameter distribution, predicted by theory (see section 3.4). Such a plateau, however, would show a frequency independent behavior and does not explain the constant minimum temperature in $\Delta\varepsilon'/\varepsilon'$, that is determined by the dominant relaxation. The cause herefore can thus not lie in a modified distribution function.

As the temperature of the minimum $T_{\min}$ is related to the temperature dependence of the dominant relaxation, a constant minimum is related to a constant relaxation rate. Such a rate, never before observed in glasses at low temperatures, can not be of phononic origin and is most likely due to the presence of nuclear quadrupoles.

As the phononic relaxation has already died out at 15 mK in structural glasses even at 60 Hz, only the temperature dependence of the non phononic relaxation present in the glass can be the cause of the maximum in $\Delta\varepsilon'/\varepsilon'$. Such a decrease of the relaxation rate would have its strongest effects at lowest frequencies, as the additional relaxation contributes less and less towards higher frequencies. Such a behavior is observed in the measured data. This means that the low frequency data of HY-1 seems to be dominated by a nuclear spin based relaxation that is constant at intermediate temperatures and then dies out towards lower temperatures. Interestingly, the highest nuclear quadrupole splitting in holmium (see table 3.1) corresponds to temperatures of about 7.5 mK. This further confirms the idea, of a nuclear spin based relaxation rate that decreases once the thermal energy becomes comparable to the level splitting caused by the nuclear quadrupoles.

The loss tangent $\tan(\delta)$ of HY-1 also shows unexpected features. At lowest frequencies, the loss does not decrease to zero towards lower temperatures, but shows a very large residual loss even at 10 mK. This has been verified in measurements of the absolute loss tangent, which lies above 1.5×10^{-3} at 200 mK for all frequencies shown here. The low temperature flank of all curves does not match a T^3 behavior. This is yet another sign, that the nuclear spin based relaxation must be temperature dependent in HY-1. The relaxation causing the high loss is again less important for higher frequencies, causing the loss tangent to decrease towards lowest temperatures. Interestingly, both the curves of the frequencies 60 and 120 Hz and those between 10 and 20 kHz lie almost perfectly on top of each other, while much larger differences are observed at the intermediate frequencies.

In the high temperature plateau regime, we see a frequency dependent maximum in all curves, followed by the slightly sloping plateau usually observed in glasses, indicating a phonon dominated regime. Finally, the increase of the loss tangent at 7 K over the whole frequency range indicates the beginning of thermal activation.

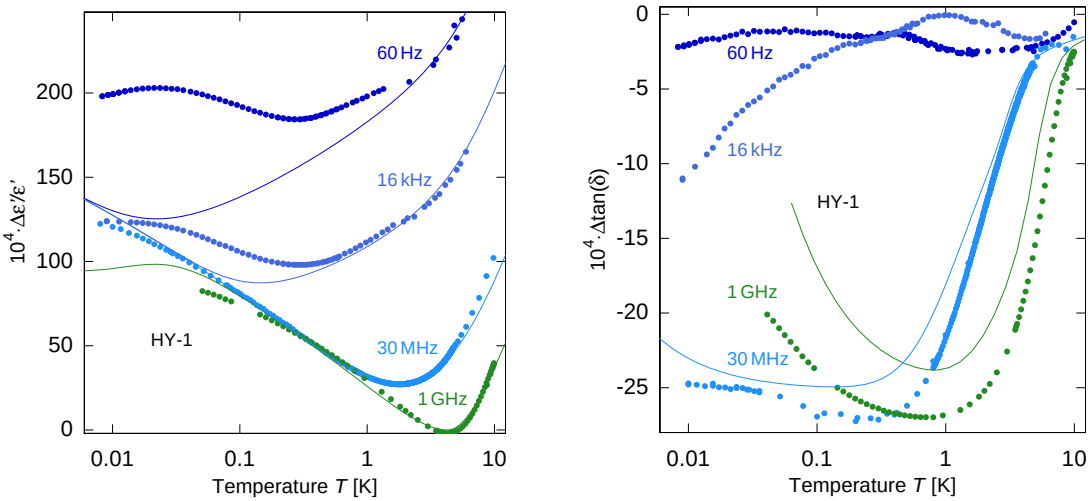

Figure 5.10: Change of the real part of the dielectric function $\Delta\varepsilon'/\varepsilon'$ (left) and the loss tangent $\Delta\tan(\delta)$ (right) of HY-1 as a function of temperature between 10 mK and 10 K at frequencies between 60 Hz and 1 GHz. Numeric calculations of the standard tunneling model including long range interaction are drawn as solid lines. Data at 30 MHz from [Zei15], at1 GHz from[Hau15].

In order to further investigate the nuclear spin based relaxation, measurements were performed at 30 MHz and 1 GHz. The results, along with measurements at 60 Hz and 16 kHz, are shown in figure 5.10. The solid lines are numeric calculations of the standard tunneling model including the dipole gap, that are shown along with the data for all frequencies at the real part of the dielectric function and the high frequencies at the loss tangent. The parameters are given in table A.1.

The data clearly shows a crossover from the nuclear relaxation dominated regime at low frequencies, to a phonon relaxation dominated regime at high frequencies. The minimum in $\Delta\varepsilon'/\varepsilon'$ shifts with frequency at high temperatures and both $\Delta\varepsilon'/\varepsilon'$ and the change of loss tangent $\Delta\tan(\delta)$ can be qualitatively described by the standard tunneling model including the dipole gap.
We now see that the low frequency curves in $\Delta\varepsilon'/\varepsilon'$ converge towards a common resonant slope at temperatures below the maximum, where it should then start to rise again towards lowest temperatures. Indeed, the 16 kHz curve might very well join this slope at temperatures only slightly below the ones achieved within this thesis.

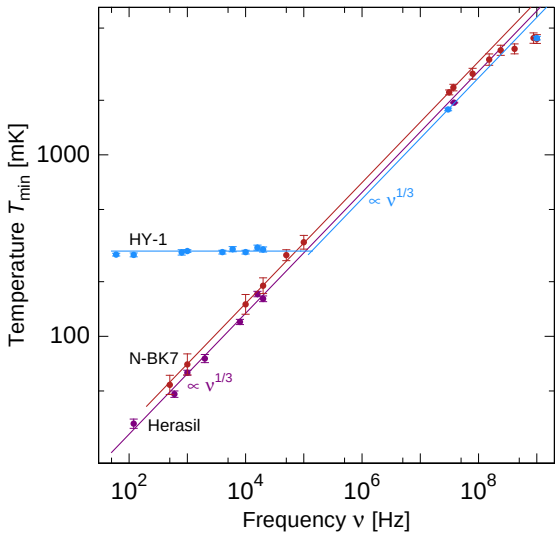

Figure 5.11: Temperature of the minimum in the real part of the dielectric function $T_{\min}$ of HY-1 (light blue) as a function of frequency. The expected $\nu^{1/3}$ behavior for one phonon relaxation and the constant value found in $\Delta\varepsilon'/\varepsilon'$ at low frequencies are shown as solid lines. The data of Herasil (dark red) and N-BK7 (red) are shown as reference.

The contribution of the nuclear relaxation to the 60 Hz curve is so large, that one would most probably have to measure down to temperatures of 1 mK or below in order to see a rise in the data.

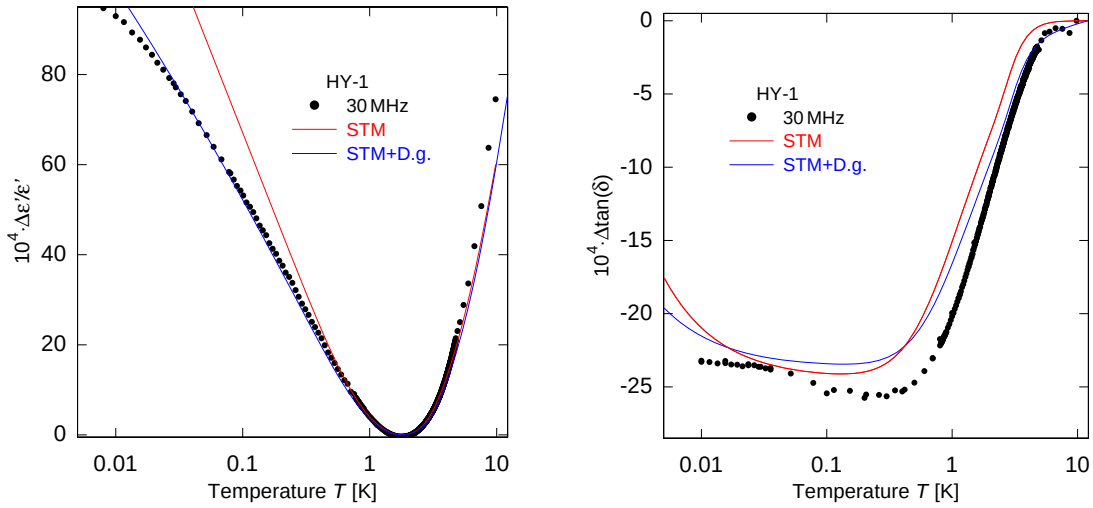

Figure 5.12: Change of the real part of the dielectric function $\Delta\varepsilon'/\varepsilon'$ (left) and the loss tangent $\Delta\tan(\delta)$ (right) of HY-1 as a function of temperature between 7.5 mK and 10 K at a frequency of 30 MHz and calculations of the unmodified standard tunneling model (red) and including the dipole gap (blue). Data from [Zei15].

Just like in the two standard glasses, we can track the temperature dependence of the minima in the change real part of the dielectric function. The results are shown in figure 5.11 in the usual double logarithmic plot. The regime of constant non phononic

loss is clearly visible. Once the phononic relaxation becomes stronger than the nearly constant relaxation, the temperature of the minima shifts again, shown here by the values at 30 MHz and 1 GHz. The latter, as expected, lies in the two phonon regime and matches the N-BK7 measurements very well. The crossover frequency between the two regimes dominated by phononic and nuclear spin based relaxation lies at about100 kHz.

We can further investigate the additional, nuclear spin based relaxation process in HY-1, by comparing the measured data to numeric calculations of the standard tunneling model, the parameters are again given in table A.1. As the constant relaxation rate of HY-1 is in the high kilohertz range, we do not expect large influences of the nuclear spin based relaxation on the high frequency behavior. Indeed, the comparison between the measured 30 MHz data and numeric calculations of the standard tunneling model, with and without a dipole gap, as shown in figure 5.12, show only the quantitative disagreement already found in N-BK7. A similar comparison was made for the 1 GHz data, where we see the same behavior. It is shown in the appendix A.2. As the calculations including the dipole gap are able to fit the real part of the dielectric function very well over a large temperature range, we have used them for the comparison to the broadband data shown in figure 5.10.

The situation is very different, if we look at the data measured at 800 Hz and com-

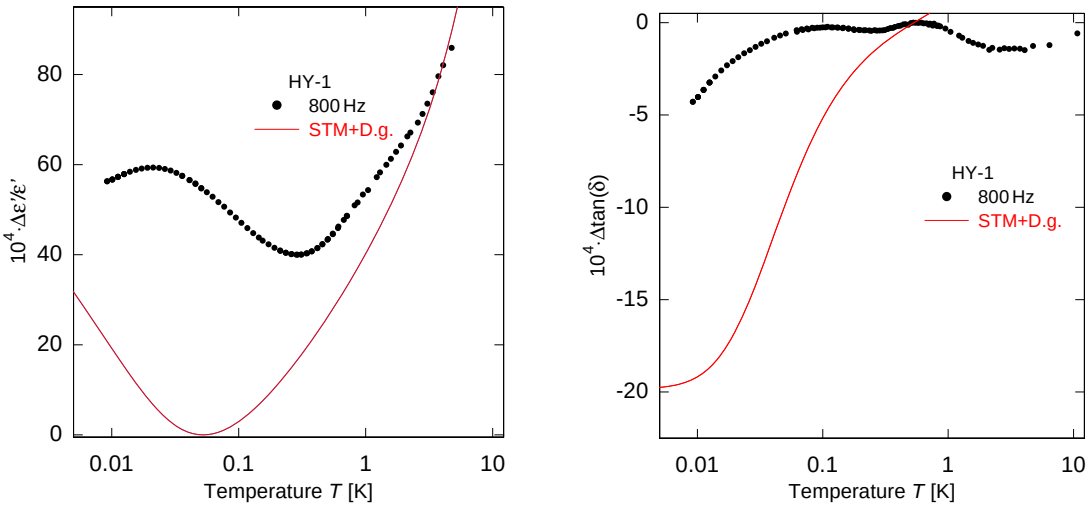

Figure 5.13: Change of the real part of the dielectric function $\Delta\varepsilon'/\varepsilon'$ (left) and the loss tangent $\Delta\tan(\delta)$ (right) of HY-1 as a function of temperature between 7.5 mK and 10 K at a frequency of 800 Hz and numeric calculations of the standard tunneling model including the dipole gap.

pare it to the calculations, as was done in figure 5.13. The large difference between the calculations and the measured data in $\Delta\varepsilon'/\varepsilon'$ is caused by the aforementioned nuclear spin based relaxation. We can now clearly see, the additional signal caused

by the relaxation, that shifts the minimum and causes a maximum as it dies out. As we would need to include a restriction of the tunneling parameter λ in order to model the slope in the plateau region of the loss tangent, we have cut off the simulations at this part here. At lower temperatures, we see the large residual loss caused by the relaxation. We also se two maxima, one below 100 mK and another around 300 mK. While the lower must be caused to the nuclear spin based relaxation, the maximum at higher temperatures can be traced back to the two phonon relaxation.

When plotting the temperature of the high temperature maximum versus frequency, we find a $\nu^{1/7}$ dependence as expected from two phonon relaxation, as shown in figure 5.14. While the onset of the two phonon relaxation in the loss tangent is usually hidden in the plateau region at low frequencies, we can see a clear onset here. The one phonon process does not show in the maxima, but the loss rather seems change from the nuclear spin based relaxation more or less directly to a two phonon dominated regime.

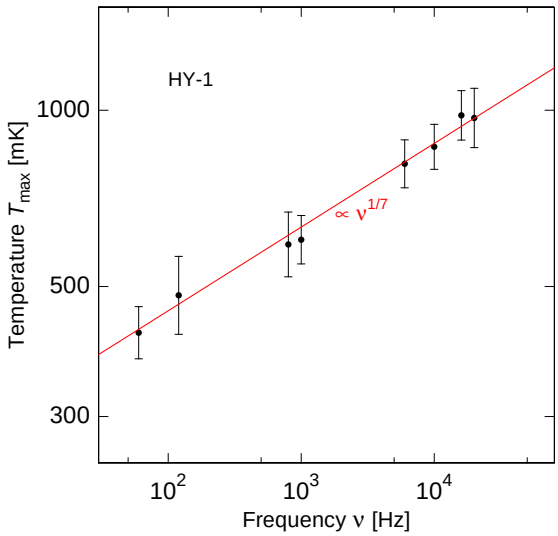

Figure 5.14: Temperature of the maximum in $\Delta \tan(\delta)$ of HY-1 as a function of frequency. The expected $\nu^{1/7}$ behavior for two phonon relaxation is shown as a solid line.

5.4 Model of a nuclear spin based relaxation rate

As the measurements performed on HY-1 have shown, the presence of large nuclear quadrupoles in the glass causes an additional relaxation that dominates the dielectric function below about 300 mK. While at high temperatures the rate is constant, as indicated by the fixed temperature of the minimum in the change of the real part of the dielectric function, it becomes noticeably smaller at low temperatures.
The rate must be due to a coupling of the tunneling two-level systems to the nuclear

quadrupole moments, as its effect are of the same order as those caused by the coupling of the two-level system to phonons. A direct coupling of the nuclear moments to the applied electric fields would cause a much larger signal, which is not observed in the measurements.

The exact temperature dependence of the relaxation rate is not known, but we can

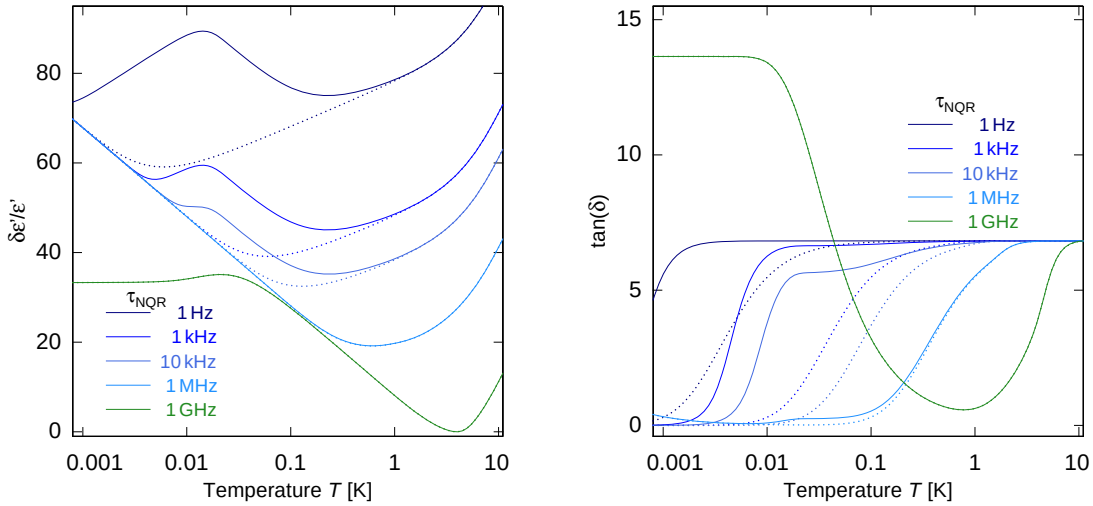

Figure 5.15: numeric calculations of the change of the real part of the dielectric function $\delta\varepsilon'/\varepsilon'$ (left) and the loss tangent $\tan(\delta)$ (right) as a function of temperature between 1 mK and 10 K at frequencies between 1 kHz and 1 GHz with an additional nuclear quadrupole driven relaxation. Unmodified calculations of the standard tunneling model are shown as dotted lines.

investigate the general effects of such a nuclear quadrupole driven relaxation rate by using a simplified phenomenological approach with the rate

$$\tau_{\mathrm{NQR}}^{-1} = \tau_{\mathrm{c},0}^{-1} \left(\frac{\Delta_0}{E}\right)^2 \coth\left(\frac{E}{2k_{\mathrm{B}}T}\right)\left(1 - \exp\left(\frac{-T}{2\delta T}\right)^a\right) . \tag{5.3}$$

The rate introduced here is constant at high temperatures. As the thermal occupation of the sublevels that are sensitive to the relaxation should be taken into consideration, we have included the usual $\coth(E/2k_{\mathrm{B}}T)$. As the rate takes place in the regime of coherent tunneling it is weighed by $(\Delta_0/E)^2$.

We have chosen a simply temperature dependent cutoff for the relaxation rate, that leads to a decrease at low temperatures. As the data does not suggest a T^n behavior, we have chosen here a modified exponential decay of the rate. For $a = 2$, the decay is simply a Gaussian centered around $T = 0$. As the temperature dependence of the dielectric function is strongly influenced by the shape of the cutoff, the parameter a was chosen as a variable, set to 3.5 in the numeric calculations presented here.

The results of numeric calculations including the nuclear quadrupole driven relaxation are shown in figure 5.15. A rate of $\tau_{\mathrm{c},0}^{-1}/2\pi = 138\,\mathrm{kHz}$ was deduced from figure

5.11, leading to $T_{\min} \approx 300\,\mathrm{mK}$ in the low frequency regime. In order to model the maximum at 15 mK, a width of $\delta T = 10\,\mathrm{mK}$ was used in the calculations.
The curves show all the main features found in the measurements performed on HY-1. The temperature $T_{\min}$ in the change of the real part of the dielectric constant is fixed at low frequencies and then shifts due to the phononic relaxation at frequencies larger than the nuclear spin based relaxation rate. This is expected, as the contribution to the real part should be large for $\omega\tau \ll 1$ and then become zero at $\omega\tau \gg 1$. The cutoff of the rate towards low temperatures leads to a decrease of the nuclear quadrupole driven relaxational contribution, which therefore becomes unimportant at all frequencies towards very low temperatures. At this point, only the resonant contribution in $\Delta\varepsilon'/\varepsilon'$ is still present and all curves follow the common low temperature resonant slope of the purely phononic standard tunneling model. Depending on the frequency, the cutoff leads to a low temperature maximum in the curves or simply to a small plateau.

Looking at the loss tangent, we see the extended plateau at low frequencies due

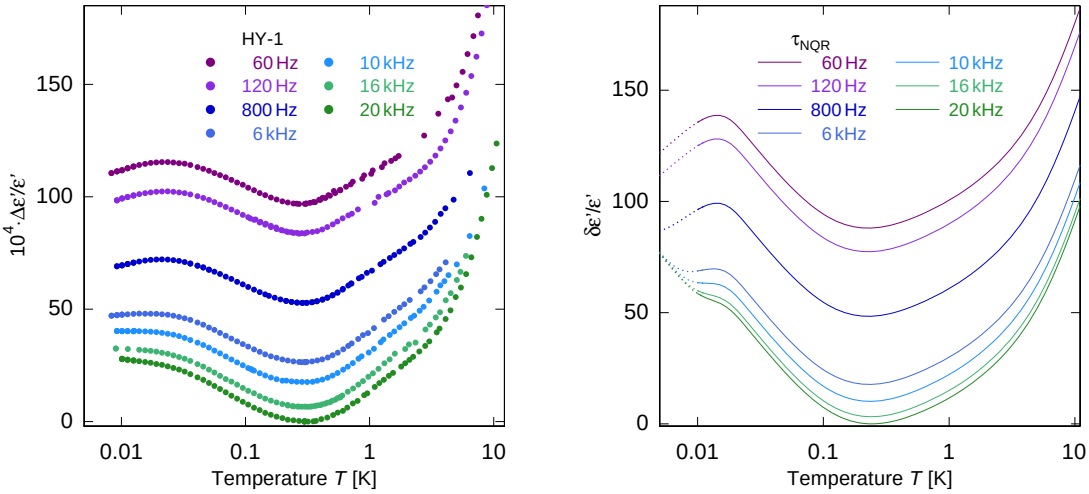

Figure 5.16: Change of the real part of the dielectric function $\Delta\varepsilon'/\varepsilon'$ of HY-1 (left) and numeric calculations including nuclear quadrupole driven relaxation (right) as a function of temperature between 8.3 mK and 10 K at frequencies between 60 Hz and 20 kHz.

to the constant part of the nuclear quadrupole driven relaxation. As was already shown in section 2.3.4, the loss caused by a single relaxation rate becomes unimportant for frequencies both much larger and much smaller than $\omega\tau = 1$. We therefore expect the largest influence at frequencies corresponding to $\nu \approx \tau_{c,0}^{-1}/2\pi$. At lowest frequencies we must then recover the a loss tangent that is dominated by phononic relaxation, just like at high frequencies. If the nuclear relaxation possesses not only one rate, but rather a distribution of rates, then the real part of the dielectric function would be dominated by the highest rate, in our case 138 kHz. In the loss, we

would, however, see a contribution of the nuclear spin based relaxation due to the lower rates at smaller frequencies, where the influence of large relaxation rates is already close to zero.
The shape of the low temperature slope in the intermediate frequency regime is, however, completely defined by the temperature dependence of the cutoff in τ_{NQR}^{-1}. At 10 kHz, this leads to a second plateau at intermediate temperatures: As the phononic relaxation decreases, the loss tangent first decreases from the high temperature plateau value to a slightly lower plateau defined by the constant relaxation with T^3. With the onset of the low temperature cutoff of the nuclear quadrupole driven relaxation, the loss tangent drops to zero.

In order to better compare the numeric calculations of this new model to our data, calculations with the values used in the low frequency measurements were performed and are shown next to the data in figures 5.16 to 5.18. No direct overlay of data and calculations was made for the sake of clarity.
We can see that even the very simplified phenomenological assumption for the low temperature cutoff of τ_{NQR}^{-1} leads to the correct general features in the curves. For the real part of the dielectric function, the comparison of model and data shows that the chosen temperature dependence causes a maximum that is still too sharp at low temperatures. The data shows a much broader maximum, corresponding to a gentler cutoff in the relaxation rate.

For a better comparison in the temperature region of the cutoff and possible

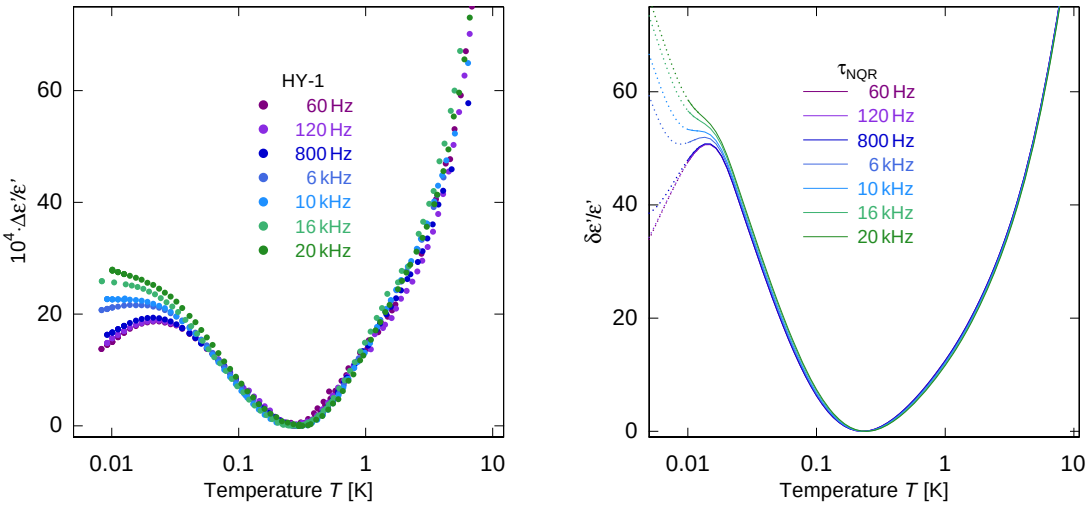

Figure 5.17: Change of the real part of the dielectric function $\Delta\varepsilon'/\varepsilon'$ of HY-1 (left) and numeric calculations including nuclear quadrupole driven relaxation (right) as a function of temperature between 8.3 mK and 10 K at frequencies between 60 Hz and 20 kHz. All curves are shifted to the minimum of $\Delta\varepsilon'/\varepsilon'$ for a better comparison of the cutoff region.

differences in the shapes of the curves, the change of the real part of the dielectric function has been shifted to the minimum in figure 5.17. Both the data and the numeric calculations are almost frequency independent for temperatures down to the minimum in the curves. Even the very small shift of the minimum temperature T_{min} with frequency observed in the data is reproduced in the calculations. It seems to stem from the slight increase of the low temperature slope at higher frequencies, where the nuclear quadrupole driven relaxation is smaller and the cutoff thus bends down the curve less at temperatures between the minimum and the maximum of the curves.

The shifted data also allows us a better look at the exact influence of the cutoff of τ_{NQR}^{-1} and its frequency dependence below the maximum. The curves at different frequencies are almost identical, both in the measured data and the calculations, as long as the relaxational contribution is still significant, seen best at the two lowest frequencies. Only when the curves approach the common resonant flank, do the shapes diverge. The higher frequencies most probably reach the resonant flank only a few millikelvin below the lowest temperatures measured here. The 16 kHz curve does indeed seem to join the 30 MHz curve in figure 5.10, confirming this assumption.

As the shape of the cutoff influences the low temperature behavior of the loss

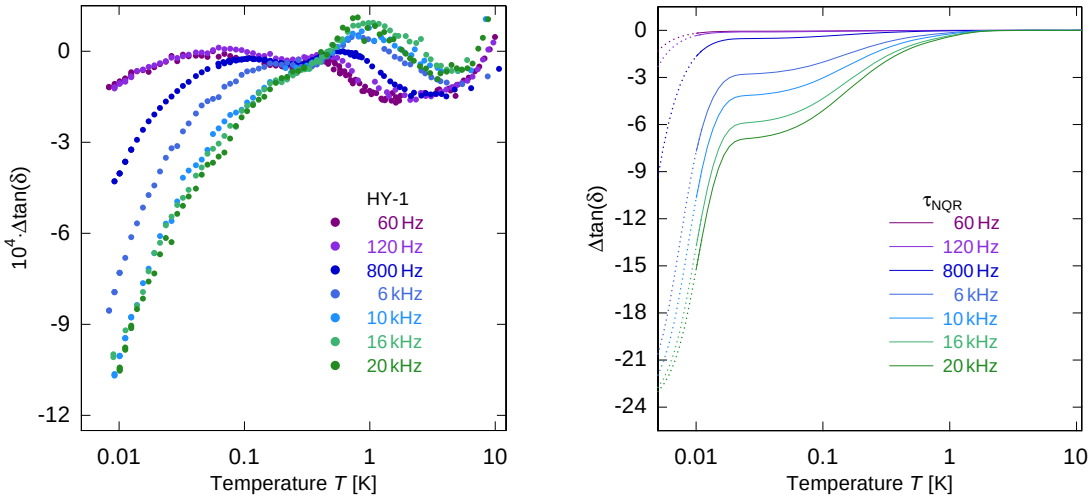

Figure 5.18: Change of the loss tangent $\Delta\tan(\delta)$ of HY-1 (left) and numeric calculations including nuclear quadrupole driven relaxation (right) as a function of temperature between 8.3 mK and 10 K at frequencies between 60 Hz and 20 kHz.

tangent directly, a bigger difference between the measured data and the calculations can be seen in figure 5.18. Also, the temperature range that is noticeably influenced as the nuclear quadrupole driven relaxation dies out is far larger in the loss tangent than in the real part of the dielectric function. Using the phenomenological

model, the numerically calculated curves only drop off from an intermediate plateau at temperatures around 20 mK, corresponding to the position of the maximum in the change of the real part of the dielectric function. The data, however, shows a much gentler drop from the very narrow intermediate plateau at temperatures as high as 200 mK at high frequencies. As the numeric calculations still only show the onset of a one phonon dominated regime for the lowest two frequencies – discernible by plateau extended to lower temperatures than for the higher frequencies – no clear evidence either in favor or against multiple nuclear spin based relaxation rates in HY-1 can be drawn from these measurements. Future measurements at even lower frequencies and temperatures can help answer this question.

5.5 Elastic measurements of HY-1

The dielectric measurements of HY-1 have shown many features, that were not present in the measurements of the standard glasses Herasil and N-BK7. We have therefore also performed low frequency elastic measurements on this glass. They allow us to probe the full distribution of two-level systems via elastic interaction, thus excluding the possibility that the effects observed in dielectric measurements which we have attributed to a coupling of tunneling two-level systems to the nuclear quadrupole moments are caused by a subset of two-level systems that only couples dielectrically.
The double paddle oscillator used for the elastic measurements is similar to the one used in [Cla00], using the capacitive measurement setup developed in [Hem15]. Only discrete modes can be excited in the paddle, but its shape allows for several of these modes between several hundred hertz and ten kilohertz.

The theoretical framework for the elastic measurements is very similar to that of dielectric measurements, only replacing the coupling

$$C_\mathrm{d} = \frac{p_0^2 P_0}{\varepsilon_0 \varepsilon_\mathrm{r}} \quad \text{with} \quad C_\mathrm{a} = \frac{\gamma^2 P_0}{\rho v^2} \,, \tag{5.4}$$

where γ and v are the elastic coupling of two level systems and the sound velocity. In addition, we find a factor of -1 in the change of the sound velocity with respect to its corresponding change in the real part of the dielectric function.

The results of the measurements performed at three different frequencies between 900 Hz and 5600 kHz are shown in figure 5.19. The elastic data shows the same features as the dielectric measurements. Both the constant minimum at about 300 mK and the maximum at 15 mK found in the dielectric measurements can bee seen as

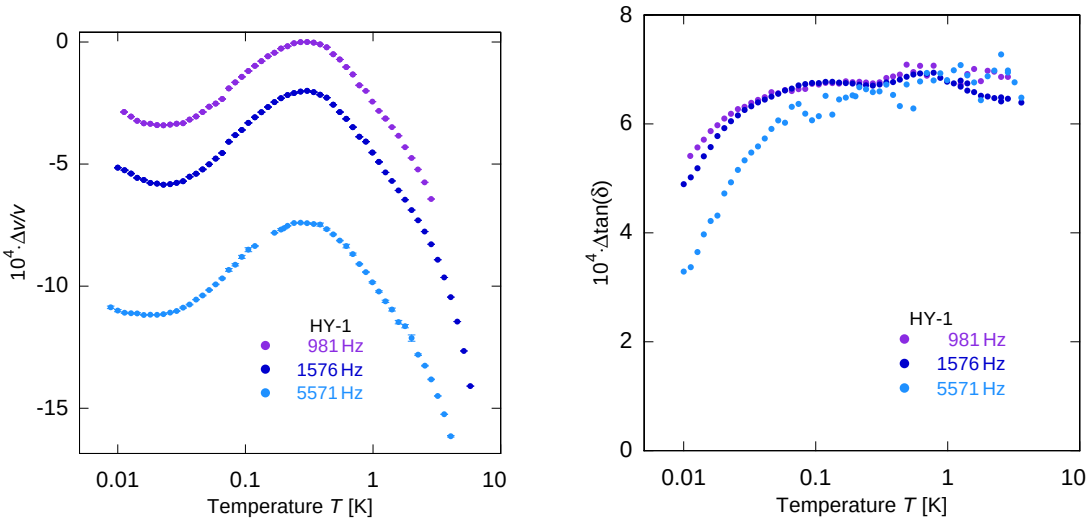

Figure 5.19: Change of the sound velocity $\Delta v/v$ (left) and the loss tangent $\Delta \tan(\delta)$ (right) of HY-1 as a function of temperature between 10 mK and 5 K at frequencies between 900 Hz and 5600 Hz. Data from [Hem14].

respective maxima and minima in the change of the sound velocity.
The loss tangent in the elastic measurement also remains at very high values down to lowest frequencies and shows the decrease at lowest temperature that does not match a T^3 behavior but is dominated by the reduction of the nuclear quadrupole driven relaxation. The measurement at 1576 Hz also clearly shows the maximum observed in the dielectric measurements, that is most probably caused by the two phonon relaxation process, and the second plateau at lower temperatures. As the measurements of the other two frequencies are too noisy, a possible shift of the maximum can not be observed here.

An even better comparison of the elastic and dielectric properties of HY-1 can be made, when overlaying measurements performed at similar frequencies. This has been done in figure 5.20 for the change of sound velocity and real part of the dielectric function at 981 Hz/800 Hz and 5571 Hz/6000 Hz. The two sets of curves match perfectly from several kelvin down to temperatures below 15 mK. The very slight deviations most likely stem from the small difference in frequency and a possible small non linear drive in the dielectric measurements.

The comparison between elastic measurements of HY-1 and the dielectric ones show that the effects measured in this glass are not just caused by a dielectrically active subset of two-level systems. The nuclear quadrupole driven relaxation instead influences the whole set of two-level systems and responds in a very similar way to both electric and mechanic strain. The measurements also show that the nuclear

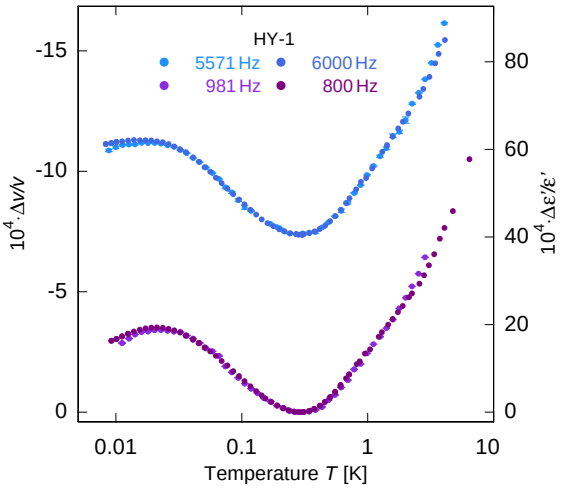

Figure 5.20: Change of the sound velocity $\Delta v/v$ and the real part of the dielectric function $\Delta\varepsilon'/\varepsilon'$ of HY-1 as a function of temperature between 10 mK and 5 K at frequencies between 800 Hz and 6000 Hz. The $y-$axis of the sound velocity measurements has been flipped for a better comparison of the data

subsystem of the sample is not accessed directly but via the tunneling two-level systems. As we only measure a subset of those systems with dielectric measurements, we would otherwise see a difference in the relative amplitude of the nuclear spin based relaxation in the total signal between the two measurement methods.

5.6 Comparison with elastic measurements of insulating spin glasses

Within this thesis, we have conducted dielectric measurements on HY-1, which contains about 0.5 % of holmium atoms. Acoustic measurements in the microwave range on holmium aluminosilicates with atomic holmium contents ranging from 1.5 % to 10 % were conducted in [Ler84, Ler87]. The results of these measurements, shown in this section, can be compared to the results obtained within this thesis. Here, we have changed the direction of the $y-$axis in the change of the sound velocity for a direct comparison between the dielectric and elastic measurements.

The relative change of the sound velocity between 100 mK and 6 K for three different alumosilicates is shown in figure 5.21. The measurements of the two glasses containing 10 % and 6.7 % of holmium both show a maximum at about 2 K, after which the curves first drop towards lower temperatures and then rise again below about 400 mK, the glass containing 3.4 % of holmium only shows a plateau region in the same temperature range. We also notice, that the low temperature slope is very flat in the 10 % sample and then becomes steeper with decreasing holmium content of the glasses.

The principal shape of the curves with an additional maximum is similar to the be-

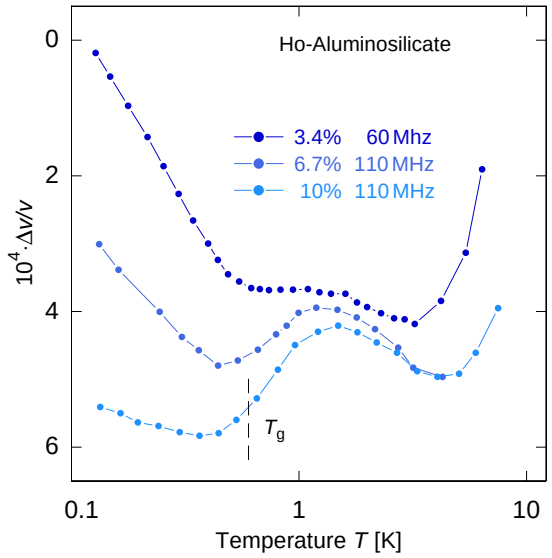

Figure 5.21: Change of the sound velocity $\Delta v/v$ of holmium aluminosilicates containing various holmium contents as a function of temperature between 100 mK and 10 K at frequencies between 60 MHz and 110 MHz. Data from [Ler84, Ler87].

havior found in HY-1 at low frequencies caused by a constant relaxation rate which dies out towards lowest temperatures. The rate found in the elastic measurements of the holmium aluminosilicates seems to increase with the holmium concentration, which explains the plateau in the 3.4 % curve compared to the pronounced maxima at higher concentrations. We therefore expect the rate in HY-1 to be smaller than in the three glasses shown here.
This is indeed the case, but while the rate in HY-1 is in the high kilohertz range and therefore no longer dominates in the megahertz regime (see figure 5.10), the rates found in the high concentration holmium aluminosilicates are in the high megahertz to gigahertz range. The rate also begins to die out at temperatures about two orders of magnitude higher than in HY-1 for all three glasses shown here. It can therefore be assumed, that the underlying process causing the relaxation is a different one in HY-1 than in the high concentration glasses, howbeit with a similar general temperature dependence.

As holmium not only carries a nuclear electric quadrupole moment but also magnetic moment, its spins can undergo a phase transition, which can then in turn influence the elastic properties of the glass. In magnetic measurements, a spin glass transition at $T_g \approx 600$ mK was detected in the glass containing 10 % of holmium [Cha79]. Such a transition could strongly change the coupling between the two-level systems and the magnetic moment of the sample. If the energy splittings of sublevels due to the magnetic moments are in the range of several hundred millikelvin to one kelvin, the rate would also die out in this temperature range. A coupling between the tunneling two-level systems and the magnetic moments of the holmium, causing a relaxation that is dominant at high temperatures and then decreases at lower temperatures due

to high energy splittings of the sublevels or an ordering of the spins, may well explain the observed data.

Indeed, the phenomenon described above has been observed in other insulating spin glasses [Dou87, Dou89]. Examples of elastic measurements in the microwave regime on glasses containing cobalt and nickel are shown in figure 5.22. The two glasses show spin glass transitions at $T_g(\mathrm{Co}) \approx 1.8\,\mathrm{K}$ and $T_g(\mathrm{Ni}) \approx 1.5\,\mathrm{K}$ respectively. In both materials, we see the influence of a constant relaxation in the gigahertz range, that shifts the minima of different measurement frequencies to a constant temperature. As the influence of the constant relaxation increases towards the lower frequencies, a plateau and later a maximum in the data develops. In both glasses the relaxation rate then begins to decrease at temperatures slightly above the spin glass transition and the magnetic moment driven relaxation dies out. As this happens at much higher temperatures than in HY-1, the recovery of a common resonant curve is in an temperature region that is easily achievable in experiments and nicely seen in both pictures.

The data shows, that magnetic moments can interact with the tunneling two-level systems in glasses, causing an additional relaxation rate that is constant at high temperatures and then dies out once the magnetic moments begin to order or their energy splitting is in the same range as the thermal energy.
Turning back to holmium aluminosilicates, we can investigate the relaxation processes in more detail by looking at the magnetic field dependence of the elastic

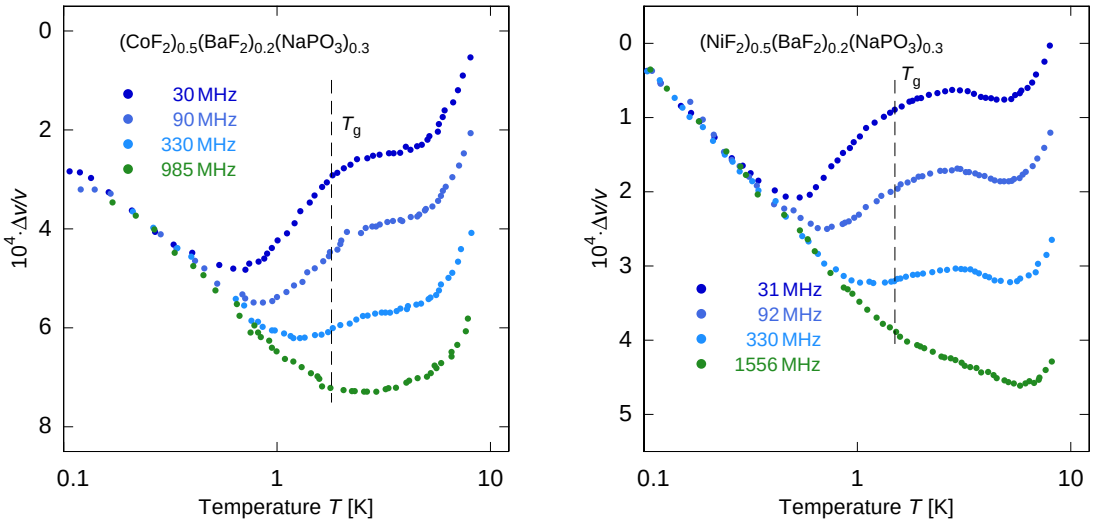

Figure 5.22: Change of the sound velocity $\Delta v/v$ of insulating spin glasses containing about ten atomic percent of cobalt (left) and nickel (right) as a function of temperature between 100 mK and 10 K at frequencies between 30 MHz and 1.6 GHz. Data from [Dou87, Dou89].

properties. Such measurements, performed on the glass containing 10 % of holmium in magnetic fields up to 6 T, are shown in figure 5.23, both for the relative change of sound velocity and the attenuation.
With increasing magnetic field, the relative change of sound velocity both loses the maximum at 2 K and shows a strongly increased slope at low temperatures. At 1 T, the additional relaxation rate causing the maximum has decreased so much, that we only see a minimum and no more maximum or plateau. The further increase of the slopes towards higher fields then causes the minimum to shift towards slightly higher temperatures again.
The system seems to saturate towards 6 T, where the low temperature slope is in fact that of the glass containing 3.4 % of holmium, indicating that the relaxational process causing the observed strong decrease of the low temperature slope is also strongly diminished by the magnetic field. At the same time, a new maximum appears around 250 mK, that becomes more pronounced with the increasing magnetic field.
The attenuation also shows a strong magnetic field dependence. A maximum in the data around 1 K present at zero field disappears with higher magnetic field, while a new maximum appears around 250 mK at the highest field.

The magnetic field dependence of the data is consistent with the idea that the additional relaxation at zero field is caused by the magnetic moments of the holmium in

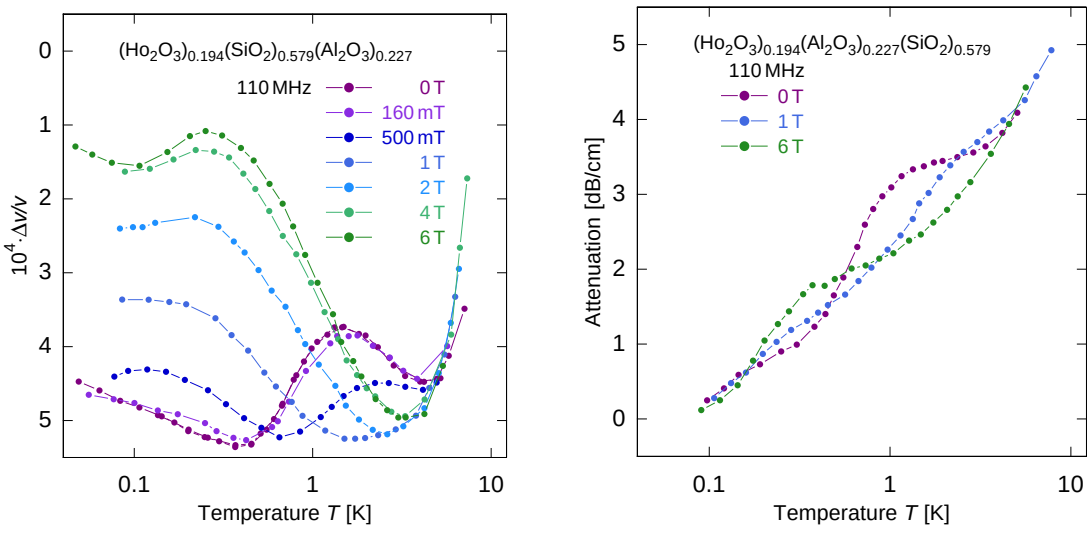

Figure 5.23: Change of the sound velocity $\Delta v/v$ (left) and attenuation (right) at a frequency of 110 MHz of a holmium aluminosilicate containing ten atomic percent of holmium as a function of temperature between 100 mK and 10 K in magnetic fields up to 6 T. Data from [Ler87].

the glass. Their influence disappears with increasing magnetic field, so the new features at high fields are most probably due to the nuclear properties of the holmium. They show up in the same temperature range, where many of the anomalies observed in HY-1 are observed.

Both the different temperature and frequency range of the additional relaxations observed in the high concentration holmium aluminosilicates and HY-1 point towards the fact, that the effects in the latter are more likely caused by the nuclear quadrupole moments than by the magnetic moments of holmium. At the same time, the coupling between tunneling two-level systems and magnetic moments can give us a hint as to why the nuclear spin based relaxation rate is so strong in this material. The temperature of the spin glass transition is strongly dependent on the concentration of magnetic moments, a simple linear dependence is sometimes assumed and observed at small concentrations [Mal79, Bin86]. This would place the spin glass transition temperature of HY-1 at temperatures of 30 mK or below, as very small concentrations can suppress the spin glass transition. In this case, the magnetic dipoles present in HY-1 could lead to a stronger coupling between the nuclear bath and the tunneling two-level systems, increasing the relaxation rate. Such an increase of a quadrupole relaxation rate due to the presence of paramagnetic moments has already been observed at high temperatures [Blo48].

5.7 Dielectric measurements of N-KZFS11

As we have just discussed, the holmium ions in HY-1 possess not only a nuclear quadrupole moment but also a magnetic moment. It is therefore useful to consider a material that contains similar amounts of large nuclear quadrupole moments as HY-1, but no magnetic moment. Similar dielectric measurements as on HY-1 have therefore been conducted on N-KZFS11, which contains about 1.5% of tantalum. We will again first focus on the low frequency measurements and then also consider the data taken in the megahertz and gigahertz regime.

Figure 5.24 shows data taken at multiple frequencies between 120 Hz and 16 kHz. We find both similar features and marked differences between the measurements of N-KZFS11 and of the other glasses both in the real part of the dielectric function and in the loss tangent.

Just like in HY-1, the minimum in $\Delta\varepsilon'/\varepsilon'$ does not shift at lowest frequencies, indicating a regime of constant relaxation. Its presence in both N-KZFS11 and HY-1 confirms the large nuclear quadrupole moments as its most likely source. The rate of the nuclear spin based relaxation must be lower in N-KZFS11 than in HY-1, however,

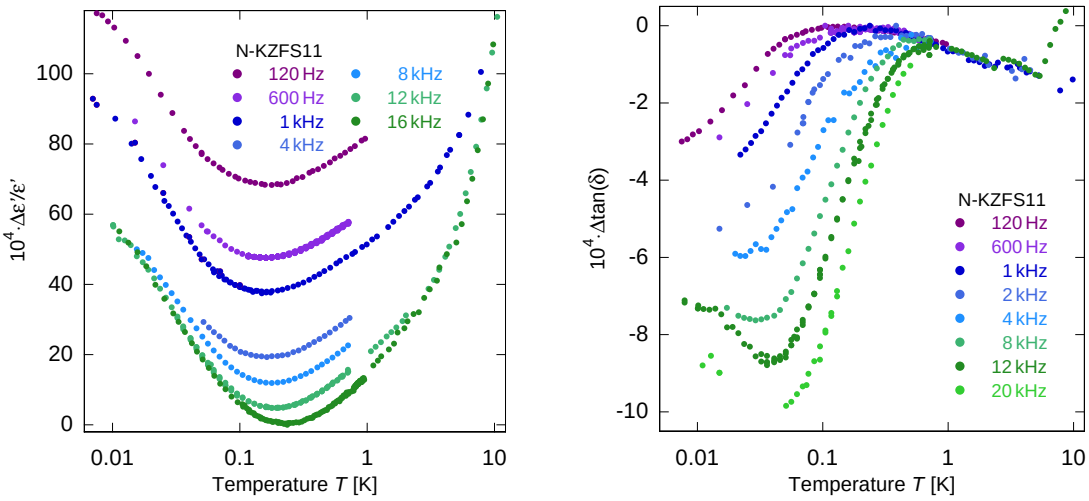

Figure 5.24: Change of the real part of the dielectric function $\Delta\varepsilon'/\varepsilon'$ (left) and the loss tangent $\Delta\tan(\delta)$ (right) of N-KZFS11 as a function of temperature between 7.5 mK and 10 K at frequencies between 120 Hz and 16 kHz.

as we already see a small frequency dependence of the minimum's temperature for frequencies above 6 kHz. The curves slightly flatten below 15 mK but the maximum observed in HY-1 can not be observed in N-KZFS11.
The loss tangent also looks notably different than those of the previously discussed samples. While it shows a slight slope at high temperatures, much like N-BK7, the behavior below 1 K differs from both the standard glasses and HY-1 for all frequencies. At lowest frequencies, the loss tangent again shows a large residual loss due to the constant nuclear spin based relaxation, confirmed in absolute measurements to be above 1.5×10^{-3}. We do not, however, observe the clear second maximum that is present in the loss tangent of HY-1 at low frequencies or the direct crossover from the two phonon to the nuclear spin based relaxation regime.
At frequencies above 5 kHz, where the effect of the nuclear spin based relaxation has become smaller, the loss tangent instead rises again for temperatures below 50 mK, a feature not observed in HY-1.

Again, a better insight into the nuclear spin based relaxation in the glass can be gained when measuring over a broader frequency range. An overview of the broadband dielectric behavior of N-KZFS11 at temperatures between 7.5 mK and 10 K is given by figure 5.25, where the temperature behavior of the dielectric function is shown for four frequencies ranging from 1 kHz to 895 MHz.
Along with the data of the real part of the dielectric function, we show numeric calculations of the standard tunneling model including a nuclear spin based relaxation rate of $\tau_{c,0}^{-1}/2\pi = 5.4\,\text{kHz}$. As the data shows no large effects of a decrease in the nuclear spin based rate, we have not included a decrease of the rate in the calcula-

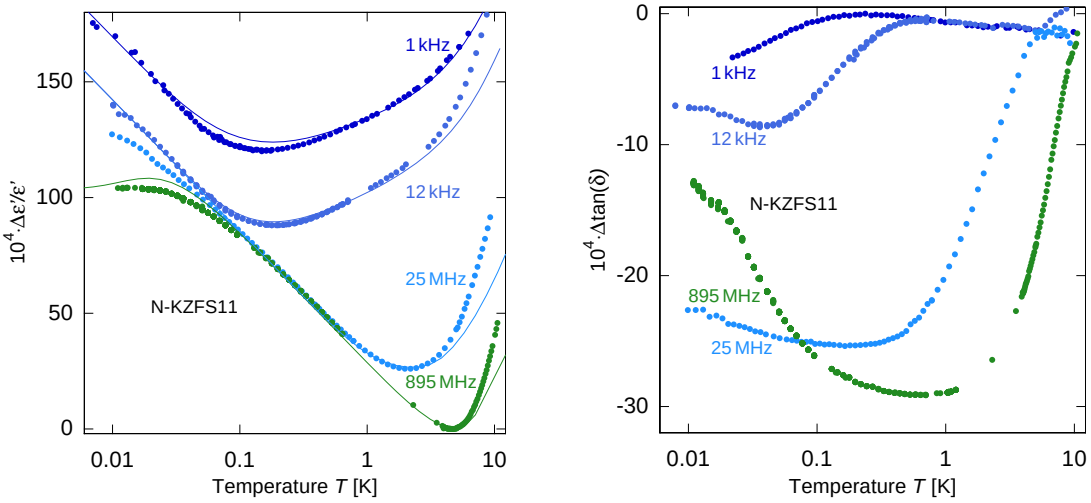

Figure 5.25: Change of the real part of the dielectric function $\Delta\varepsilon'/\varepsilon'$ (left) and the loss tangent $\Delta\tan(\delta)$ (right) of N-KZFS11 as a function of temperature between 7.5 mK and 10 K at frequencies between 1 kHz and 1 GHz. High frequency data at25 MHz from [Sch16], at 895 MHz from [Wes15].

tions. Neither were any modifications made to the distribution of the parameters of the standard tunneling model.

This very simple model fits the real part of the dielectric function surprisingly well below temperatures of about 5 K at all frequencies. Only inn the two phonon dominated regime does the model not rise quickly enough towards higher temperatures, as already observed in N-BK7, and we see small deviations in the 25 MHz curve towards low temperatures.

The crossover from the very high loss at low frequencies to more standard tunneling model like behavior at higher frequencies can be seen very clearly both in the change of the real part of the dielectric function and the loss tangent. We can see it even more easily, if we again plot the frequency dependence of the minimum in $\Delta\varepsilon'/\varepsilon'$.

The result is shown in figure 5.26 in dark blue. Both the regime of the constant relaxation and the crossover to the one phonon relaxation are well visible. The crossover frequency lies at about 6 kHz, in good agreement with the rate used in the numeric calculations to obtain the best fit.

The beginning shift of the the $T_{\min}$ around several kilohertz shows us that within less than one order of magnitude in frequency, the system turns from being phonon dominated to the regime of nuclear spin based constant relaxation. We can even see the onset of the $\nu^{1/3}$ behavior around 12 kHz. The 25 MHz measurement deviates from the value expected from the low frequency measurements, either due to the onset of the two phonon regime or due to a remnant of the nuclear spin based relaxation that still influences the lower frequencies more than expected from the observed shift.

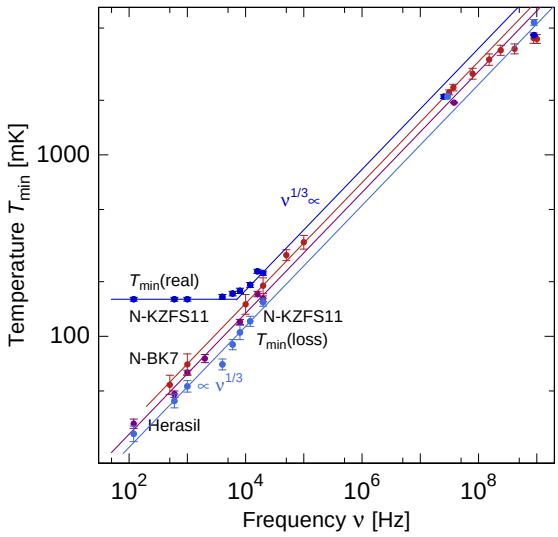

Figure 5.26: Temperature of the minimum in the real part of the dielectric function $T_{\min}$(real) (dark blue) of N-KZFS11 and of the nominal temperature $T_{\min}$(loss) obtained from the best fit in $\Delta\tan(\delta)$ (light blue) as a function of frequency. The expected $\nu^{1/3}$ behavior for one phonon relaxation and the constant value found in $\Delta\varepsilon'/\varepsilon'$ at low frequencies are shown as solid lines. The data of Herasil (dark red) and N-BK7 (red) are shown as reference.

The rate of nuclear spin based relaxation in N-KZFS11 is more than twenty times smaller, than the one observed in HY-1, while their nuclear quadrupole frequencies are very similar. This might be to an enhancement of the coupling strength through the magnetic moments in HY-1, that are not present in N-KZFS11. We also see a much bigger effect of the rate's reduction towards low temperatures in HY-1, especially in the loss tangent. Partially, this is due to the higher relaxation rate, but it may also partially be due to the different distribution of electric field gradients of tantalum ions in N-KZFS11 and holmium ions in HY-1. While the tantalum ions in N-KZFS11 are part of the glass matrix and therefore experience a broad distribution of electric field gradients leading to a broad distribution in sublevel energy splittings, the holmium ions of HY-1 are almost free ions. The distribution of their electric field gradients should be much narrower, leading to a well defined energy splitting and thus to a more rapid decrease of the nuclear spin based relaxation rate.

In order to closer investigate the influence of the nuclear spin based relaxation on the dielectric function of N-KZFS11, we again show measurements alongside numeric calculations for the two frequencies 1 kHz and 12 kHz. Additional figures of the two other frequencies in the phononic regime displayed in figure 5.25 are shown in A.2. Figure 5.27 shows the temperature dependence between 7.5 mK and 10 K of the dielectric function at a frequency of 1 kHz. Numeric calculations of the standard tunneling model that give the best fit in $\Delta\varepsilon'/\varepsilon'$ are shown with the data as red solid lines.
The change of the real part of the dielectric function $\Delta\varepsilon'/\varepsilon'$ is very well described by the model, far better than for example the data obtained on N-BK7 or Herasil. In fact, no other structural glass other than N-KZFS11 has shown the $-2:1$ slope ratio

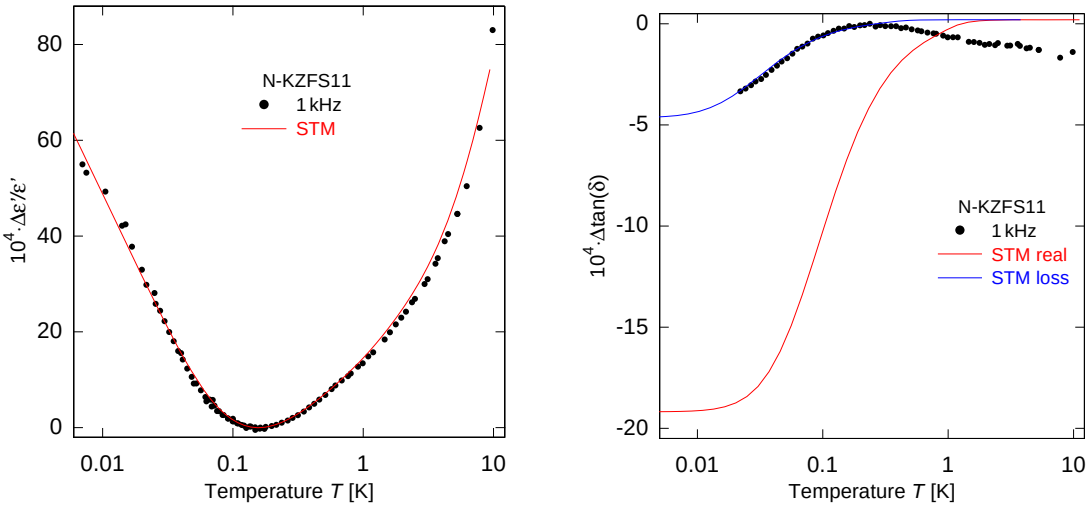

Figure 5.27: Change of the real part of the dielectric function $\Delta\varepsilon'/\varepsilon'$ (left) and the loss tangent $\Delta\tan(\delta)$ (right) of N-KZFS11 as a function of temperature between 7.5 mK and 10 K at a frequency of 1 kHz and calculations of the standard tunneling model using $\Delta\varepsilon'/\varepsilon'$ (red) and $\Delta\tan(\delta)$ (blue) for the best fit parameters.

in the region of one phonon relaxation. The data of N-KZFS11, however, only shows a very slight deviation at lowest temperatures, which might be due to the beginning reduction of the nuclear spin based relaxation.
The loss tangent shows the high residual loss expected from the nuclear spin based relaxation and the slope at high temperature due to a restricted distribution of parameters not considered for these calculations. The low temperature behavior of the loss tangent resembles the shape of the T^3 slope towards low temperatures expected in one phonon relaxation.
If we use the one phonon coupling strength as a free fitting parameter and allow for a constant residual loss, we can describe the slope very well, as is shown by the blue curve. We can then use the value for the one phonon coupling of the fit to calculate the position of the minimum in $\Delta\varepsilon'/\varepsilon'$ expected from the deduced coupling strength at this frequency, as was done for the values of $T_{\mathrm{min}}(\mathrm{loss})$ plotted in light blue in figure 5.26.

The shift of the nominal temperature of the minimum calculated from the loss shows a $\nu^{1/3}$ behavior down to lowest frequencies Unlike in HY-1, we seem to see a clear influence of the one phonon relaxation in the loss tangent of N-KZFS11. The coupling strength deduced from the loss is larger than the one expected from the real part, the discrepancy is most likely due to a small distortion of the curves caused by a modified distribution or not entirely temperature independent nuclear spin based relaxation.

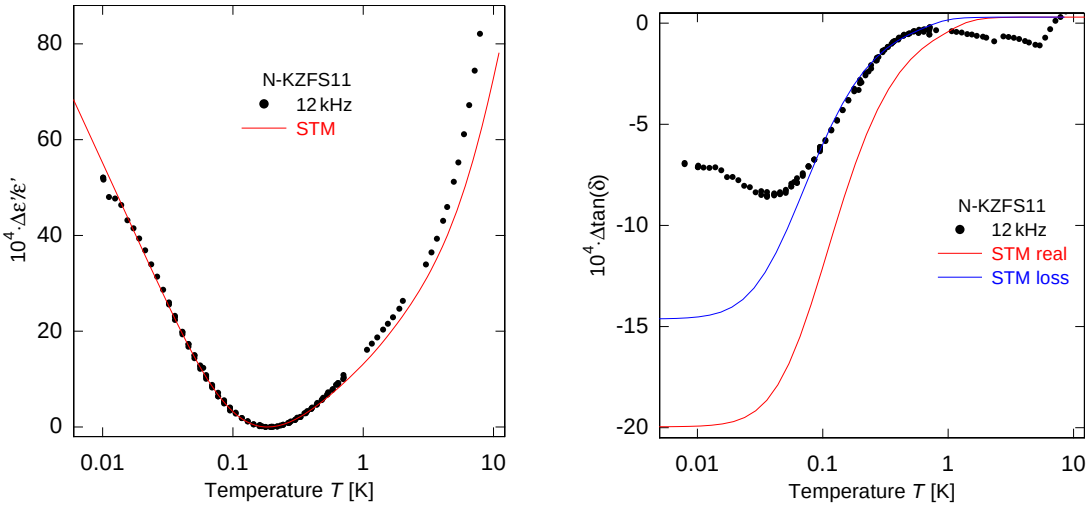

Figure 5.28: Change of the real part of the dielectric function $\Delta\varepsilon'/\varepsilon'$ (left) and the loss tangent $\Delta\tan(\delta)$ (right) of N-KZFS11 as a function of temperature between 7.5 mK and 10 K at a frequency of 12 kHz and calculations of the standard tunneling model with the best fit to $\Delta\varepsilon'/\varepsilon'$ (red) and to $\Delta\tan(\delta)$ (blue).

While the assumption of a temperature independent residual loss leads to good agreements both at low frequencies and in the two high frequency measurements (see figures A.2 and A.3 in the appendix), the measurements between 6 kHz and 20 kHz show an additional feature in their loss tangent. As an example, we have plotted the 12 kHz data in figure 5.28 along with numeric calculations of the standard tunneling model. The frequency lies in the crossover regime from the nuclear spin based to the phonon relaxation regime. This leads to a low temperature slope of the loss tangent, that has the much reduced residual loss of a frequency in the crossover regime between nuclear spin based and phononic relaxation. Its T^3 slope therefore also lies at temperatures much closer to those expected from the fit of the real part of the dielectric function.
We also see, however, an increase of the loss towards low temperatures beginning at 50 mK. The cause of this increase is yet to be determined, measurements towards lower temperatures and in the high kilohertz regime would help shed more light on this intriguing behavior.

The measurements discussed in this section show, that the dielectric behavior of N-KZFS11 like that of HY-1 is dominated by a nuclear spin based relaxation process at low temperatures. The measurements also show, that the additional relaxation observed in HY-1 and N-KZFS11 is indeed most likely due to the large nuclear quadrupole moments in the two samples, the magnetic moments only make the cou-

pling stronger but do not seem to fundamentally change the coupling mechanism. The nuclear spin based relaxation in N-KZFS11 is therefore smaller than in HY-1, but much larger than in the standard glasses, where it can not be directly observed in the temperature T_{min} down to frequencies as low as 60 Hz. Its temperature dependence down to 10 mK is also smaller than the one observed in HY-1. The exact temperature dependence of the nuclear spin based relaxation depends on the sample's chemistry, it therefore differs slightly between N-KZFS11 and HY-1.

5.8 Field dependent measurements of the dielectric function

In addition to measurements in the linear response limit of the glasses, measurements were also performed at higher electric fields.With these experiments we can address the question whether the nuclear quadrupole enabled relaxation depends on the field strength.
Again, we will first show measurements performed on Herasil and N-BK7 and then discuss the differences observed in HY-1 and N-KZFS11.

5.8.1 Herasil and N-BK7

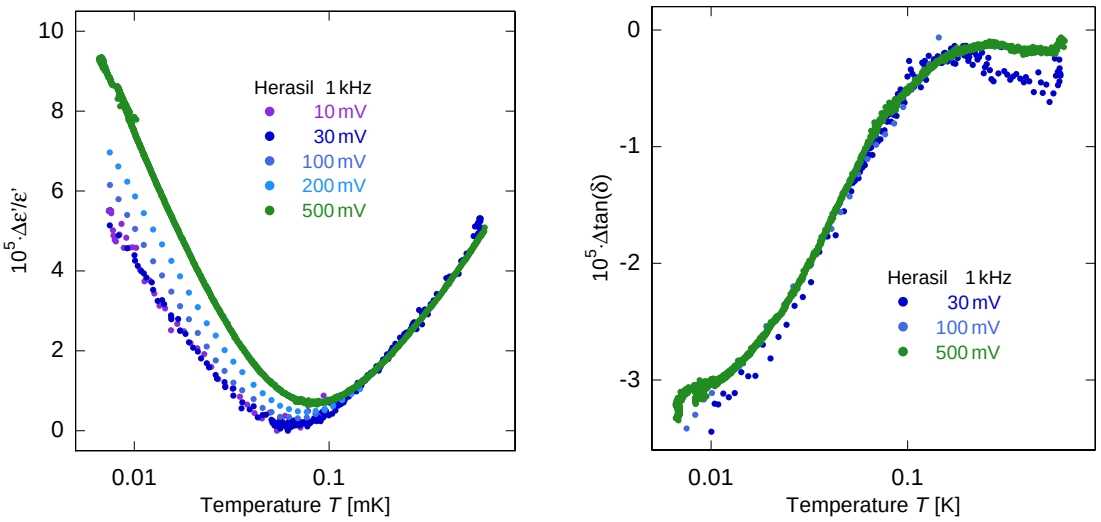

Figure 5.29: Change of the real part of the dielectric function $\Delta\varepsilon'/\varepsilon'$ (left) and the loss tangent $\Delta\tan(\delta)$ (right) of Herasil as a function of temperature between 10 mK and 1 K at a frequency of 1 kHz and excitation voltages between 10 mV and 500 mV.

The dielectric properties of both Herasil an N-BK7 have been measured at different excitation voltages and thus electric fields at 1 kHz. The Herasil data was obtained

in [Luc11], that of N-BK7 in [Woh01a]. As the microstructured interdigital capacitor used for the measurements on Herasil does not allow for a direct conversion of excitation voltages into strengths in the sample, only excitation voltages are given.
Figure 5.29 shows the temperature dependent change of the dielectric function at a frequency of 1 kHz and excitation voltages between 10 mV and 500 mV. As the high temperature relaxational slope should be insensitive to high electric fields at low frequencies according to the model by Stockburger et al. given in section 2.4.1, the data is arranged to match at high temperatures.
One can clearly see, that the data follows the predictions of the model very well. While there is no change in $\Delta\varepsilon'/\varepsilon'$ in the relaxational part of the curve, the resonant slope steepens more and more with increasing electric fields higher than 30 mV. At the highest applied fields this even leads to a shift of the temperature of the minimum $T_{\min}$.
The model also predicts a saturation at very high fields and very low temperatures. This can not be observed here, but might be reached at even higher fields. As the two curves measured at 10 mV and 30 mV are identical over the whole temperature region, we can safely assume, that we can well reach the linear response regime with our setup at these excitation voltages.
The loss tangent hardly changes with the applied electric field over the whole measured temperature range. As the signal is solely caused by relaxational processes, no large change is expected to happen by the model.

A similar behavior is observed in the nonlinear measurements of N-BK7, as shown

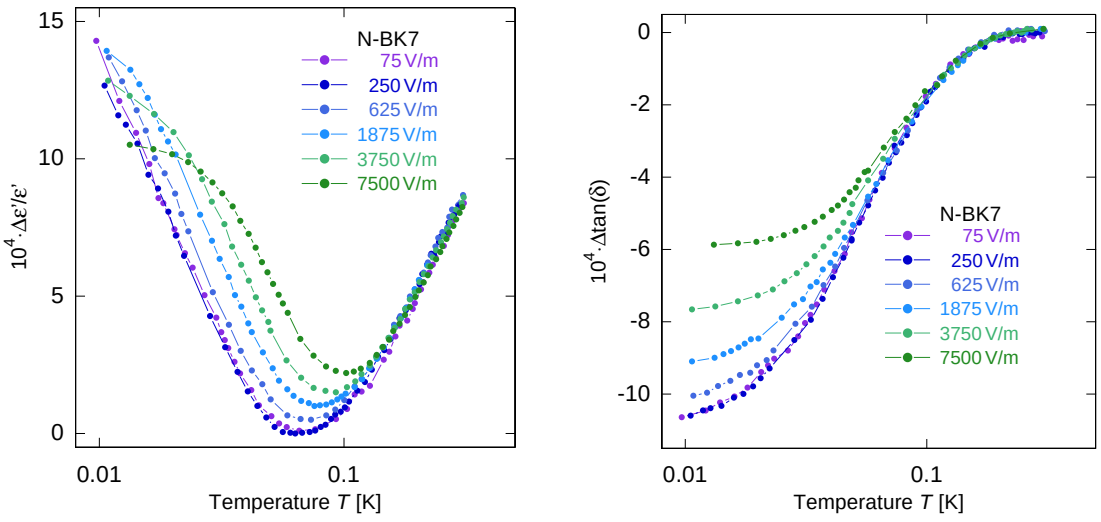

Figure 5.30: Change of the real part of the dielectric function $\Delta\varepsilon'/\varepsilon'$ (left) and the loss tangent $\Delta\tan(\delta)$ (right) of N-BK7 as a function of temperature between 10 mK and 250 mK at a frequency of 1 kHz and electric fields between 75 V/m and 6 kV/m. The lines only join the data points. Data from [Woh01a].

in figure 5.30. As the sample was measured in a parallel plate capacitor, we can here convert the applied excitation voltages to electric field strengths. The relaxational flank of the change of the real part of the dielectric function $\Delta\varepsilon'/\varepsilon'$ is not changed, even up to the highest electric fields applied here. Both the curves of the linear response regime and the effects at the onset of the nonlinear regime are well visible and match the curves of Herasil, while the flattening off towards lowest temperatures at highest fields is most likely due to thermal decoupling due to insufficient thermalization of the sample. This thermal decoupling also masks the expected steepening of the resonant slopes at high electric field

The loss tangent again remains identical for all electric fields at high temperatures and then shows a flattening off towards lower temperatures at high electric fields. The onset of this behavior is moved to higher temperatures with larger fields, thus confirming the thermal decoupling due to larger input powers.

As the setup used for these measurements is a parallel plate capacitor, the critical electric field where nonlinear effects begin to show can be estimated to about 500 V/m. Assuming a dipole moment p of about 3 Debye, that has been measured in silicon nitride [Sar16], we find $pF \approx 5 \times 10^{-27}$ J. The onset of field dependent effects thus already lies about two order of magnitude below the estimation of $pF \approx k_\mathrm{B}T$ even at at 10 mK, where $k_\mathrm{B}T = 1.4 \times 10^{-25}$ J.

5.8.2 HY-1 and N-KZFS11

Measurements performed at different field strengths on HY-1 at both 800 Hz and 16 kHz allow us to further investigate the nuclear quadrupole driven relaxation. Figure 5.31 shows the temperature dependence of the dielectric function of HY-1 at 800 Hz measured at excitation voltages between 4 mV and 2000 mV. Again, we can assume the measurements performed with 10 mV and below to be in the linear regime, as they show no change due to the different electric fields both in the real part and the loss tangent of the dielectric function.

Unlike Herasil an N-BK7, HY-1 shows a large electric field dependence in the loss tangent. With increasing voltage, the contribution of the relaxation is gradually decreased. The onset of this decrease happens at about 350 mK for all voltages applied, directly below the maximum in the plateau of the loss tangent. As we have attributed the maximum to a two phonon relaxation process, we expect it to remain unchanged, just like the loss tangent of Herasil and N-BK7.

At lower temperatures the loss tangent decreases, resulting in a narrowing of the plateau region at temperatures below the maximum. Its strong sensitivity do electric fields shows once again, that the dominant relaxation process can not be phononic for all temperatures below the maximum of the loss tangent caused by two phonon

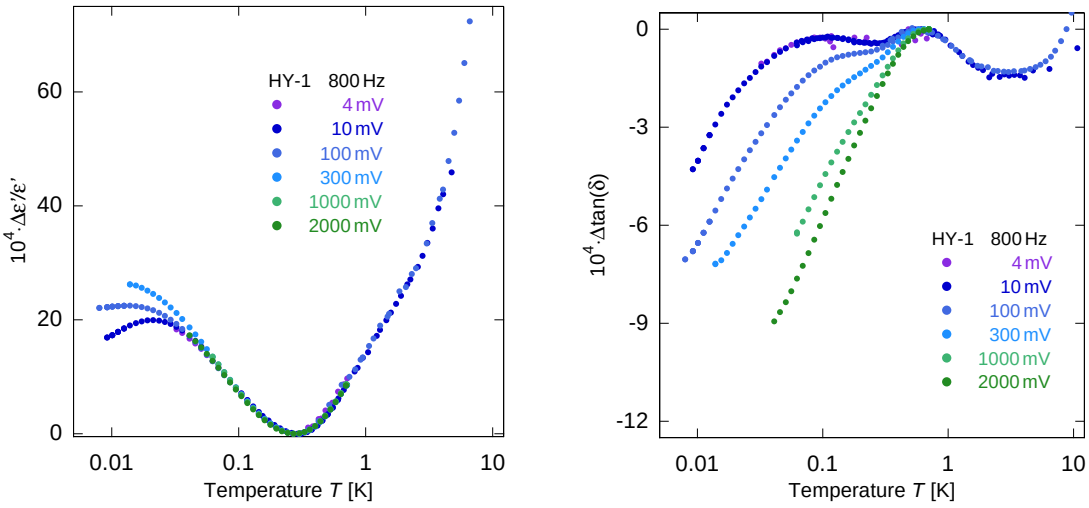

Figure 5.31: Change of the real part of the dielectric function $\Delta\varepsilon'/\varepsilon'$ (left) and the loss tangent $\Delta\tan(\delta)$ (right) of HY-1 as a function of temperature between 10 mK and 10 K at a frequency of 800 Hz and excitation voltages between 4 mV and 2000 mV.

relaxation .

The real part of the dielectric function remains unchanged with higher electric fields, except for the temperatures below 80 mK. With increasing electric field, the maximum becomes less pronounced and finally vanishes due to the increased slope in this temperature region. The effect seems similar to that of an increase in the measurement frequency, but the temperature of the minimum T_{min} is not shifted and the low temperature slope neither flattened nor steepened.

At first glance, this seems like a contradiction. As the maximum is defined by decrease of the nuclear spin based relaxation at low temperatures, its disappearance seems to show that the nuclear relaxation becomes constant even at low temperatures. On the other hand, the behavior of the loss tangent indicates that the nuclear spin based relaxation vanishes with high electric field. This should then in turn allow the minimum in the real part to shift to lower temperatures, or, if the process is temperature depended, decrease the low temperature slope. As the usual nonlinear sensitivity of the resonant process should not be changed by additional relaxational processes, one would also assume a steepening of the low temperature slope.

If, however, the two processes at low temperatures show a similar but opposite reaction to high electric fields, this would explain the data very well. An increase of the resonant process would steepen the curve, while a reduced relaxational process would flatten it. If the two effects were of equal magnitude, their effects then would cancel out, except for the region of the maximum of $\Delta\varepsilon'/\varepsilon'$, where the relaxational process no longer gives a constant contribution. Once the relaxational process is completely switched off by the electric field, the low temperature slope of $\Delta\varepsilon'/\varepsilon'$ should show

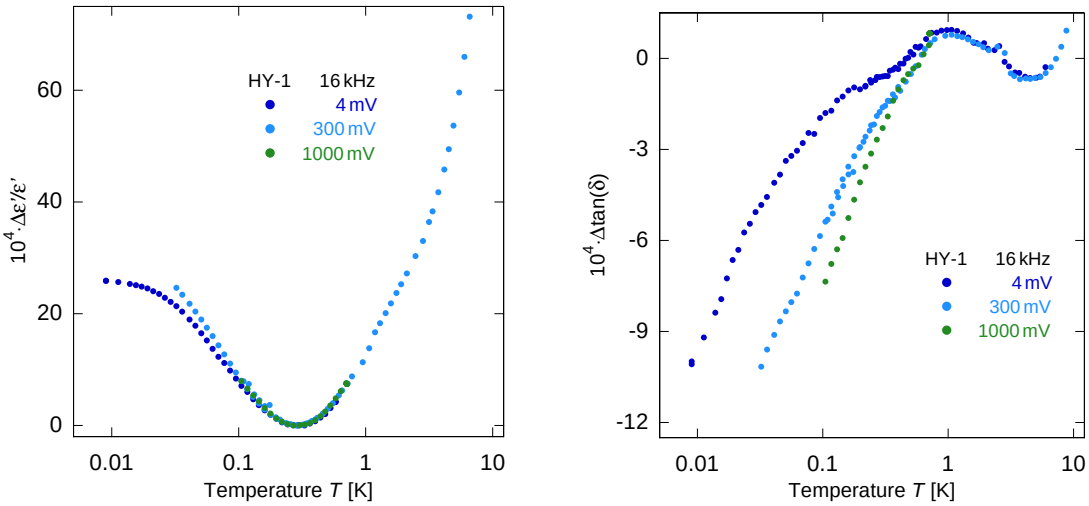

Figure 5.32: Change of the real part of the dielectric function $\Delta\varepsilon'/\varepsilon'$ (left) and the loss tangent $\Delta\tan(\delta)$ (right) of HY-1 as a function of temperature between 10 mK and 10 K at a frequency of 16 kHz and excitation voltages between 4 mV and 1000 mV.

an increased slope.
This is indeed the case, as can be seen in figure 5.32, where nonlinear measurements taken at 16 kHz are shown. As the contribution of the nuclear relaxation is less than at 800 Hz to start with, it already vanishes at lower excitation voltages. We thus see an increased low temperature slope at 300 mV, below about 100 mK.
The difference in the loss angle is also smaller than at lower frequencies, but very similar in its effects. The data again shows an electric field dependence only below the maximum, where it decreases faster with higher electric fields.

As mentioned before, no effect of strong electric fields on the relaxational processes is expected by the model of Stockburger et al. developed for low frequencies. A theoretical treatment of the nonlinear relaxational response of dielectric glasses at low temperatures does, however, exist for the microwave regime [Lai84, Kir97]. In both cases, a linear decrease of the relaxational response with increasing strong electric field is predicted. The effect should most strongly affect two-level systems with small energy splittings $E \leq pF$.
We can roughly estimate the relevant energy splitting here, by taking into account, that the onset of the nonlinearities lies between 10 mV and 100 mV in HY-1. They are similar in relative magnitude to those found in Herasil at temperatures of about 10 mK with the same measurement.
Using the approximation that the dipole moments in both glasses should have roughly the same value, we can conclude that the relevant relaxational process corresponds to energy splittings of $k_\mathrm{B}T \approx 10\,\mathrm{mK}$. They dominate the nuclear spin based re-

laxational contribution even up to temperatures of 350 mK. While the two-level systems have a flat distribution and the phononic relaxation covers a broad energy range at a given temperature, the energy splitting of the systems contributing to the constant relaxation seem to have a much smaller distribution. The temperature corresponding to the largest nuclear quadrupole frequency of ^{165}Ho is about 7.5 mK, again confirming that the nuclei carrying large nuclear quadrupole moments are the best candidates for the cause of the low temperature relaxation in HY-1.

On N-KZFS11, no systematic measurements of the electric field dependence were

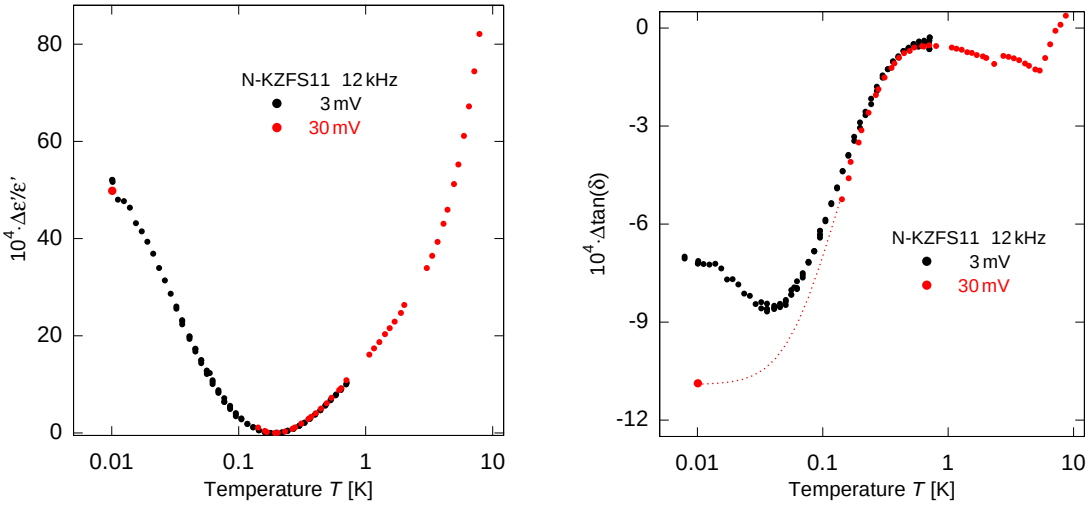

Figure 5.33: Change of the real part of the dielectric function $\Delta\varepsilon'/\varepsilon'$ (left) and the loss tangent $\Delta\tan(\delta)$ (right) of N-KZFS11 as a function of temperature between 10 mK and 10 K at a frequency of 12 kHz and excitation voltages of 3 mV and 30 mV.

conducted, but we can get a rough estimate of the glasses sensitivity to electric fields. As is shown in figure 5.33, at 12 kHz measurements both with an excitation voltage of 3 mV and of 30 mV have been performed. No data exists between 11 mK and 100 mK for the higher voltage, as the sample was only thermalized at low temperatures and then heated up without long thermalization steps. The fine dotted line therefore only serves as a guide to the eye.

Even in these first measurements, a similar behavior to that of HY-1 can again be observed in N-KZFS11. The real part of the dielectric function appears to be unchanged by the stronger electric field, just like the high temperature part of the loss tangent. Its rise towards low temperatures is strongly suppressed by the electric field, however, and seems to have vanished even at 30 mV. We can thus assume, that the rise of the loss tangent at intermediate frequencies is caused by a relaxational process involving systems with energy splittings below 10 mK. Further measurements in the nonlinear regime both at 12 kHz and at a lower frequency should therefore bring a deeper insight into the underlying processes of the nuclear relaxation in N-KZFS11.

5.9 A new picture of nuclear spin based relaxation

The measurements performed within this thesis on glasses both with and without large nuclear electric quadrupoles have given new insights into the role of the nuclear moments on the properties of glasses at low temperatures. While the influence of nuclear quadrupoles on the dielectric constant of glasses at low temperatures has been considered before, only possible influences on the resonant regime were regarded, as described in section 3.4. The only direct observations of a coupling between tunneling systems and the nuclear bath before this thesis were made in magnetic fields.
Our measurements have, however, revealed a non phononic relaxation mechanism at zero field that can be attributed to the interaction between tunneling two-level systems and the nuclei that carry electric quadrupole moments and which must become the dominant relaxation process in glasses at low temperatures.

An overview of the different relaxational regimes for all four glasses measured

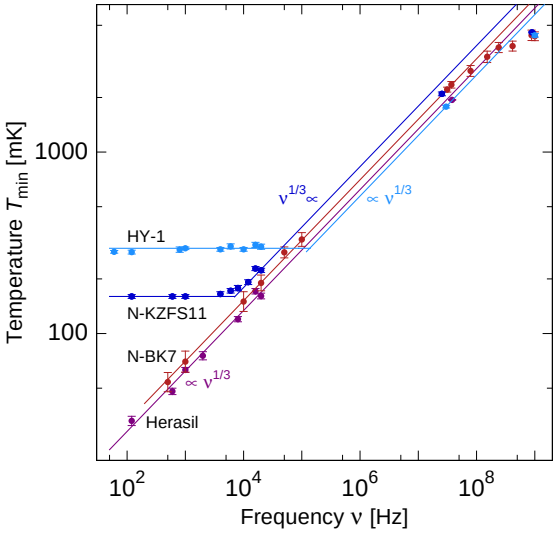

Figure 5.34: Temperature of the minimum in the real part of the dielectric function $T_{\min}$ of Herasil (dark red), N-BK7 (red), N-KZFS11 (blue) and HY-1 (light blue) as a function of frequency. The expected $\nu^{1/3}$ behavior for one phonon relaxation and the constant value found in $\Delta\varepsilon'/\varepsilon'$ at low frequencies are shown as solid lines.

within this thesis is shown in figure 5.34. The crossover between the one phonon relaxation and the regime of constant relaxation in N-KZFS11 and HY-1 is clearly visible, the different relaxation rates found in the two glasses cause the difference in the constant temperature $T_{\min}$ at low frequencies.
We have found that the effect of the nuclear spin based relaxation on the dielectric function is of the same order of magnitude as that caused by the interaction of the two-level systems with phonons in both glasses. If the interaction of the electric field were with the nuclear moments directly, we would expect a larger change of both $\Delta\varepsilon'/\varepsilon'$ and $\tan(\delta)$, as their concentration is around one percent, while that of

the tunneling systems is only a few ppm and even less for dipole carrying tunneling systems.
As was shown for HY-1, the relaxational contribution caused by the nuclear moments is of the same in dielectric and elastic measurements, the different concentration of accessible tunneling systems does not influence the relative strength of the nuclear spin based relaxation. This again points towards a coupling between the tunneling two-level systems and the nuclei.

Around temperatures where the quadrupole splitting becomes comparable to the thermal energy, the contribution of the nuclear heat capacity to the total heat capacity of a glass becomes dominant by several orders of magnitude. As the rough approximation in section 5.1 has shown, the heat capacity can be of the order of 1 J/mol K. The large contribution of the nuclear heat capacity to the specific heat shows, that energy can be effectively transferred to this subsystem once the quadrupole energy splitting becomes comparable to the thermal energy.
Measurements of nuclear magnetic resonances in crystalline and amorphous materials show a significantly larger relaxation rate in the amorphous state [Sze75], indicating a good coupling of the nuclear quadrupole moments to local defects. This coupling of two-level systems in an amorphous material to external strain, that causes a thermally activated process at high temperatures and a tunneling process below a few kelvin, leading to a deformation of the lattice. As the energy splittings caused by nuclear electric quadrupoles are extremely sensitive to local field gradients, such a deformation can help access the nuclei very effectively.

At low enough temperatures, the constant nuclear spin based relaxation should

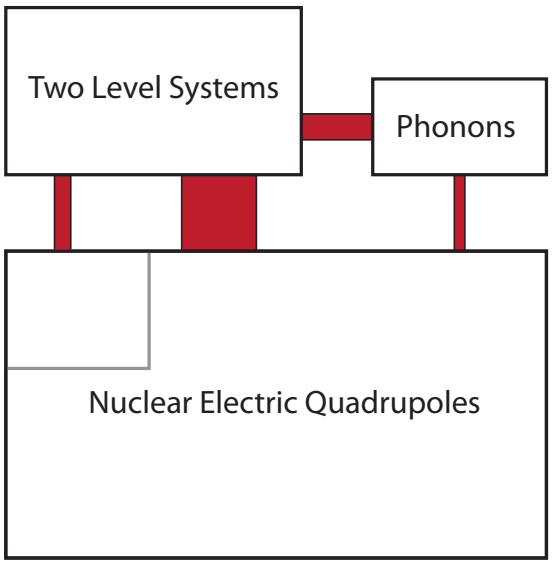

Figure 5.35: Schematic picture of the different subsystems present in a glass at low temperatures. The size of the connecting bars indicates the coupling strength between the different systems. The nuclear quadrupoles of different isotopes present in the glass form separate subsystems with varying coupling strengths.

become dominant in all glasses containing nuclei that carry nuclear quadrupole moments. A schematic picture of the different subsystems and their coupling is shown in figure 5.35: The two-level systems can couple to both the phonons and the nuclear moments with different coupling strengths. These couplings, leading to different relaxation rates, depend on both the temperature and the chemical composition of the glass.
At high temperatures, the phononic coupling will always dominate. Due to its T^3 dependence at low temperatures, it will then become irrelevant in comparison to a constant relaxation rate caused by the coupling between the two-level systems and the nuclear moments. The coupling strength here can depend on the quadrupole energy splitting, the possible presence of paramagnetic moments in the glass and the concentration of the quadrupole carrying nuclei. Thus, several isotopes can cause nuclear spin based relaxations of different rates in the same glass.
Once the temperature becomes comparable to the quadrupole splitting, the relaxation rate will diminish notably, as is the case in HY-1 around 15 mK. The exact temperature dependence of this process must depend on the electric field gradient distribution of the relevant isotopes. It must therefore be different in the case of glass formers like tantalum, built into the silicate matrix, and in the case of almost free ions of network modifiers like holmium. The nuclear spin based relaxation thus depends strongly on the chemical environment, leading to a strong material dependence of the effect. This material dependence is a stark contrast to the universal behavior predicted by the purely phononic standard tunneling model.
Once the relaxation rate's contribution to the loss tangent diminishes notably towards lower frequency, we expect the loss tangent to be dominated again by phononic relaxation at low frequencies, until the frequency one again becomes comparable to a smaller relaxation rates due to other isotopes in the glass.
With the very small splitting caused by ^{11}B, present in almost all multicomponent glasses, we would expect a significant contribution of a nuclear spin based relaxation at lowest temperatures to the dielectric function, only visible at very small frequencies in dielectric or elastic measurements.

Knowing about the possible influence of nuclear quadrupole moments on glasses in the tunneling regime, we can find other traces of the relaxation in different types of measurements as well: The nuclear moments can cause a magnetic field dependence, that is indeed found in multicomponent glasses, even when the dielectric measurements in zero field show no direct evidence of the relaxation [Woh01b, Pol09]. Polarization echo experiments also show a magnetic field dependence [Lud02, Lud03] of the echo amplitude.
Since with echo experiments, either with polarization or phonon echoes, we can determine both the magnitude and the temperature of both τ_1 and τ_2 by choosing the

appropriate echo sequence, they are an appropriate instrument for further investigations of the nuclear spin based relaxation. Phonon echo experiments on the high concentration holmium aluminosilicate discussed in section 5.6 have already shown, that the spin lattice relaxation time τ_1 in this material becomes much larger with an applied magnetic field, while the dephasing time τ_2 remains almost unchanged.
Two pulse polarization echo experiments on N-KZFS11 and HY-1 show not only a sizable magnetic field dependence but also much smaller echo amplitudes in zero field than other multicomponent glasses in the experimentally accessible decay times [Wol14, Tsu16]. As the two glasses both have a large dielectric susceptibility, this means that the echo must decay very rapidly within less than 2 µs. As the presence of nuclear spin based relaxation causes a much smaller τ_1 at low temperatures than phononic relaxation, τ_2 is limited as well, causing the rapid decay. The flattening off towards lowest temperatures observed in the high frequency measurements of N-KZFS11 and HY-1 may be caused by such a very small τ_2.

The large range in possible nuclear spin based relaxation rates and their temperature dependence effectively breaks the long proclaimed universal behavior of glasses at low temperatures. Instead, we have found effects in a range of physical properties, such as the heat capacity and the dielectric and elastic properties of glasses, that can change over several orders of magnitude depending on the chemical composition of a glass.

6. Summary and Conclusions

Within this thesis, we have performed measurements of the dielectric function of four different glasses down to 7.5 mK and over a frequency range spanning almost eight orders of magnitude between 60 Hz and 1 GHz. Three distinct setups were used in order to cover this large frequency range, all of them optimized fore the precise measurements of both the real part of the dielectric function and the loss tangent.
The focus was hereby put on the low frequency measurements of the two glasses N-KZFS11 and HY-1 at temperatures below 10 K, where the glasses are in the tunneling regime and their behavior should be described by the standard tunneling model.
Both N-KZFS11 and HY-1 contain a sizeable amount of nuclei carrying very large nuclear quadrupole moments. Any influence of nuclear moments on glassy properties, already observed in the case of polarization echoes, was therefore expected to be most prominent in these two glasses. The two other glasses, Herasil and N-BK7, measured within this thesis contain no large nuclear quadrupole moments but have been previously measured. They have therefore served as a comparison and used to test the validity of possible extensions of the standard tunneling model.

Several modifications of the standard tunneling model have previously been suggested in order to explain the deviations between the predictions of the model and dielectric and elastic measurements. We have conducted numeric simulations using the most prominent of these modifications, including different variations of the parameter distribution, the effects of long range interaction and additional relaxation mechanisms such as thermally activated relaxation. Comparisons of measured data to different combinations of the extensions have allowed us to explain certain deviations from the predictions of the standard tunneling model found in the dielectric properties of N-BK7.

Unlike predicted by theory [Bur06a, Bur06b, Bur06c], we have not found a notable influence of the nuclear quadrupole moments on the resonant part of the dielectric function. Instead, both N-KZFS11 and HY-1 show an additional, non phononic relaxation rate in the medium to high kilohertz range. Its influence can be observed both in the shift – or lack thereof – of the minimum of the real part of the dielectric function and a very large residual loss even at lowest temperatures. This relaxation rate becomes dominant in the low frequency regime below several hundred millikelvin, as the phononic relaxation dies out towards lower temperatures.
Such a relaxation has never before been observed in glasses at low temperatures and

is most likely due to a coupling of the tunneling two-level systems to the nuclear heat bath of the glasses.
Measurements of the thermalization times and an estimation of the specific heat at lowest temperatures have shown a very large specific heat, which implies that the whole set of nuclei carrying large quadrupole moments in the glasses must contribute to the nuclear heat bath at temperatures around 10 mK. A strong coupling between the nuclear heat bath and the two-level systems of the glass is thus very likely.
The crossover from the nuclear driven relaxation to the phonon dominated regime could be observed in N-KZFS11, where it lies within the range of the low frequency measurement setup. Measurements of the two glasses at much higher frequencies than the relaxation rate show only marginal influences due to the additional relaxation but instead can be well described using the phononic relaxations and the same extensions of the standard tunneling model applied to N-BK7.
In glasses containing elements with smaller nuclear quadrupole moments, the nuclear driven relaxation rates must be much lower than in the two glasses containing tantalum and holmium. Although the relaxation in these glasses is dominated by phonons over a wide range of temperatures, the nuclear spin based relaxation becomes apparent when applying a magnetic field even at relatively high temperatures [Woh01a].

Additional elastic measurements on HY-1 show the same influence of the additional relaxation as dielectric measurements, confirming the coupling between the tunneling systems and the nuclei as the cause for the additional relaxation. Field strength dependent measurements have lead to a better discrimination between the different relaxational processes in the glasses via their response to large electric fields.

A first phenomenological model of the relaxation rate, that has been developed within this thesis, is able to reproduce the main effects found in measured data of both N-KZFS11 and HY-1. Both the large residual loss and the constant minimum and ensuing maximum in the real part of the dielectric functions are reproduced qualitatively by our model. As the temperature dependence of the loss directly shows the temperature dependence of the dominant relaxational process, the low temperature loss behavior of HY-1 can be used to learn more about the decrease of the nuclear driven relaxation. Further, more detailed and microscopically motivated models of nuclear driven relaxation can now be developed using the results obtained within this thesis.

The discovery of the nuclear driven relaxation in glasses at low temperatures has lead to a new understanding of many phenomena in the low temperature properties of glasses and confirmed the large influence of the nuclear moments via their coupling

to tunneling two-level systems, that has thus far only been observed in the magnetic field dependence of non magnetic glasses.
The relaxation rates caused by the nuclear driven relaxation vary over several orders of magnitude, from below one kilohertz in N-BK7 to more than 100 kHz in HY-1. Even larger differences can be found in the thermal properties of the glasses, where the estimated heat capacity of HY-1 and N-KZFS11 at 10 mK is more than than six orders of magnitude larger than that of N-BK7. The long proclaimed universality of glasses at low temperature that is caused by their disordered state is thus effectively lifted by the influence of nuclear quadrupoles.

We can learn more about the influence of nuclear quadrupoles and the mechanisms of the nuclear driven relaxation by performing dielectric measurements in magnetic fields. In very large fields, the nuclear moments should be aligned and thus no longer be sensitive to a change of magnetic field gradients. These measurements should therefore recover a phonon dominated behavior, even in glasses containing a sizeable amount of very large quadrupole moments. Polarization echo experiments, that allow a direct determination of relaxation rates, both in zero and a large magnetic field can give a more detailed insight into the nuclear driven relaxation process.

This thesis has shown, that the relevant interaction strengths in amorphous solids can vary over far larger ranges than previously expected at lowest temperatures. Measurements of polymer systems, whose composition can easily be varied are under way. They allow us to set the interaction strengths between tunneling systems and the concentration of nuclear quadrupole carrying elements, thereby facilitating a more detailed study of the newly found nuclear driven effects and possible microscopic descriptions.

Finally, dielectric measurements at very low temperatures and frequencies on glasses containing only small nuclear quadrupole moments, like N-BK7, should reveal the presence of a nuclear driven relaxation, that is hidden at higher frequencies due to the dominating phononic relaxation.

A. Appendix

A.1 Parameters for numeric calculations

Material	Fit	One phonon $T_{\min}(1\,\mathrm{kHz})$	Two phonon K_2	Gaussian λ $\delta\lambda$	Dipole gap P_0U_0
Default	STM+X	60 mK	25	8	1.5×10^{-3}
N-BK7	STM	70 mK	25	–	–
	STM+λ	70 mK	25	8	–
	STM+λ+D. g.	80 mK	5	7.5	1.5×10^{-3}
HY-1	STM	60 mK	25	–	–
	STM+D.g.	67 mK	15	–	1.5×10^{-3}
N-KZFS11	STM	80 mK	5	–	–
	STM (1 kHz)	160 mK	5	–	–

Table A.1: Fitting parameters used for the numeric calculations of the standard tunneling model with a flat distribution of parameters (STM), a Gaussian distribution of the tunneling parameter λ (λ) and the dipole gap (D.g.). The default parameters are those used in the numeric calculations performed for the theoretical description of extensions of the STM.

The parameters given in the table are those used for the numeric simulations of the different extensions of the standard in section 2.4 unless otherwise specified and of the fits to the measured data in chapter 5. Additionally, the minimal tunneling splitting was set to $\Delta_{0,\min}/k_\mathrm{B} = 2 \times 10^{-8}\,\mathrm{K}$ for all calculations, the maximum energy $E_{max}/k_\mathrm{B} = 1 \times 10^5\,\mathrm{K}$ in order to avoid an influence of these parameters on the calculations. For the dipole gap, we have always set the crossover energy to $W/k_\mathrm{B} = 1\,\mathrm{K}$. All the other parameters are specified for the given calculations when needed.

A.2 Additional figures

HY-1

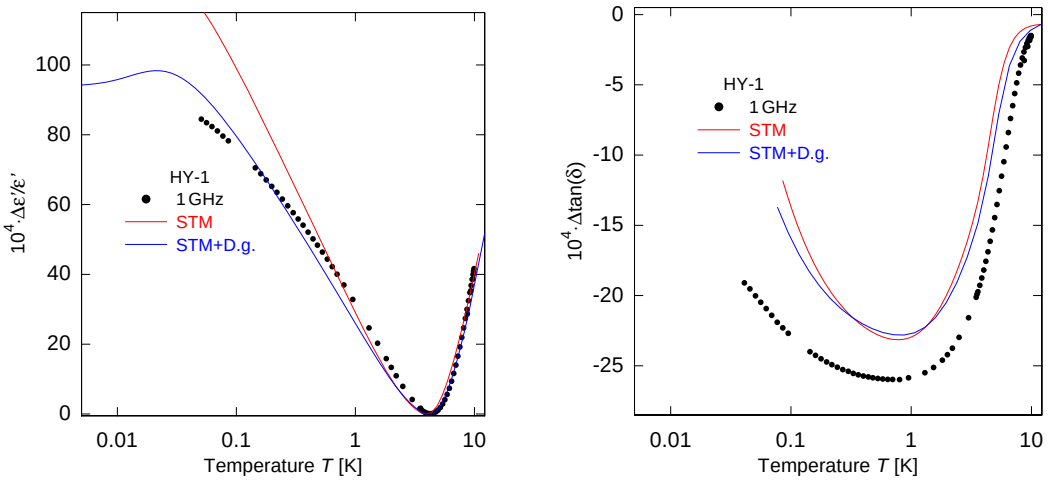

Figure A.1: Change of the real part of the dielectric function $\Delta\varepsilon'/\varepsilon'$ (left) and the loss tangent $\Delta\tan(\delta)$ (right) of HY-1 as a function of temperature between 50 mK and 10 K at a frequency of 1 GHz and numeric calculations of the unmodified standard tunneling model (red) and including the dipole gap (blue). Data from [Hau15].

N-KZFS11

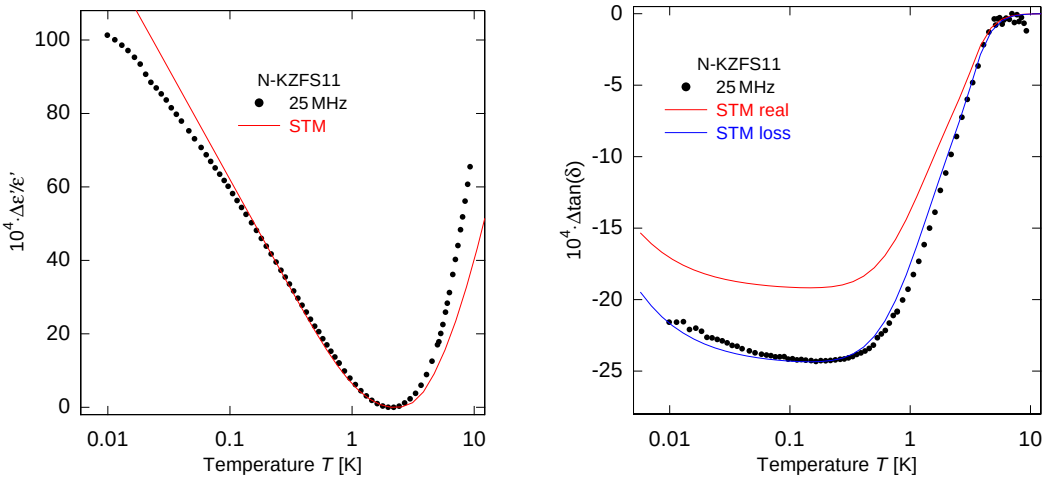

Figure A.2: Change of the real part of the dielectric function $\Delta\varepsilon'/\varepsilon'$ (left) and the loss tangent $\Delta\tan(\delta)$ (right) of N-KZFS11 as a function of temperature between 7.5 mK and 10 K at a frequency of 25 MHz and numeric calculations of the standard tunneling model with the best fit to $\Delta\varepsilon'/\varepsilon'$ (red) and to $\Delta\tan(\delta)$ (blue). Data from [Sch16].

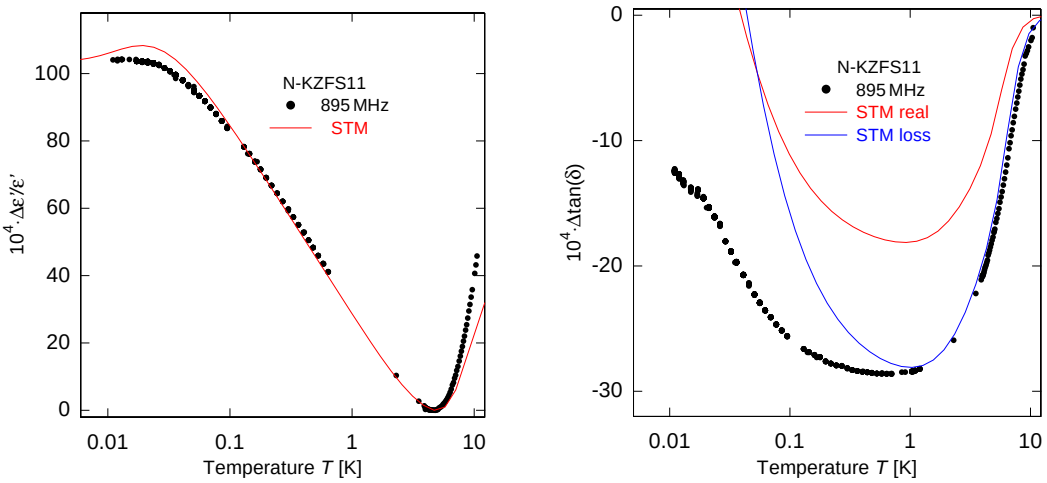

Figure A.3: Change of the real part of the dielectric function $\Delta\varepsilon'/\varepsilon'$ (left) and the loss tangent $\Delta\tan(\delta)$ (right) of N-KZFS11 as a function of temperature between 7.5 mK and 10 K at a frequency of 895 MHz and numeric calculations of the standard tunneling model with the best fit to $\Delta\varepsilon'/\varepsilon'$ (red) and to $\Delta\tan(\delta)$ (blue). Data from [Wes15].

Bibliography

[AH04] Andeen-Hagerling, AH 2700A 50 Hz – 20 kHz Ultra-Precision Capacitance Bridge – Operation and Maintenance Manual, Andeen-Hagerling Inc., Cleveland, Ohio, USA, 2004.

[All07] D. W. Allen, Holmium Oxide Glass Wavelength Standards, *J. Res. Natl. Inst. Stand. Technol.*, **112**(6), 303–306, 2007.

[And59] O. Anderson, The Debye temperature of vitreous silica, *J. Phys. Chem. Solids*, **12**(1), 41–52, 1959.

[And72] P. W. Anderson, B. I. Halperin, and C. M. Varma, Anomalous Low-temperature Thermal Properties of Glasses and Spin Glasses, *Philos. Mag.*, **25**(1), 1–9, 1972.

[Arn75] W. Arnold and S. Hunklinger, Experimental evidence for the direct interaction between two-level systems in glasses at very low temperatures, *Solid State Commun.*, **17**(7), 883–886, 1975.

[Bar80] S. D. Baranovskii, B. I. Shklovskii, and A. L. Efros, Elementary excitations in disordered systems with localized electrons, *JETP*, **51**(1), 199–207, 1980.

[Bar13] M. Bartkowiak, M. Bazrafshan, C. Fischer, A. Fleischmann, and C. Enss, Nuclear Quadrupole Moments as a Microscopic Probe to Study the Motion of Atomic Tunneling Systems in Amorphous Solids, *Phys. Rev. Lett.*, **110**(20), 205502, 2013.

[Bas90] T. J. Bastow, ^{91}Zr nuclear quadrupole coupling in zircon ($ZrSiO_4$), *J. Phys. Condens. Matter*, **2**, 6327–6330, 1990.

[Bas91] T. J. Bastow, Powder Determination of ^{39}K Nuclear Quadrupole Coupling, *J. Chem. Soc. Faraday Trans.*, **87**(15), 2453–2455, 1991.

[Baz08] M. Bazrafshan, Investigation of the microscopic nature of tunnelling systems in amorphous glycerol by two-pulse polarisation echo experiments, PhD thesis, Heidelberg University, 2008.

[Bec90] C. Bechinger, Dielektrische Messungen an Silikatgläsern bei Temperaturen unter 1 K, Diploma thesis, Heidelberg University, 1990.

[Bin86] K. Binder and A. P. Young, Spin glasses: Experimental facts, theoretical concepts, and open questions, *Rev. Mod. Phys.*, **58**(4), 801–976, 1986.

[Blo46] F. Bloch, Nuclear Induction, *Phys. Rev.*, **70**(7), 460–474, 1946.

[Blo48] N. Bloembergen, E. M. Purcell, and R. V. Pound, Relaxation Effects in Nuclear Magnetic Resonance Absorption, *Phys. Rev.*, **73**(7), 679–712, 1948.

[Bod06] D. Bodea and A. Würger, Interaction-Driven Relaxation of Two-Level Systems in Glasses, *Phys. Rev. Lett.*, **97**(16), 165505, 2006.

[Bra99] P. J. Bray, NMR and NQR studies of boron in vitreous and crystalline borates, *Inorg. Chim. Acta*, **289**(1-2), 158–173, 1999.

[Buc84] U. Buchenau, N. Nücker, and A. J. Dianoux, Neutron Scattering Study of the Low-Frequency Vibrations in Vitreous Silica, *Phys. Rev. Lett.*, **53**(24), 2316–2319, 1984.

[Buc92] U. Buchenau, Y. M. Galperin, V. L. Gurevich, D. A. Parshin, M. A. Ramos, and H. R. Schober, Interaction of soft modes and sound waves in glasses, *Phys. Rev. B*, **46**(5), 2798–2808, 1992.

[Bun85] D. S. P. Bunbury, C. Carboni, and M. A. H. McCausland, NMR of ^{165}Ho in the Ising ferromagnet $Ho(OH)_3$, *J. Phys. C Solid State Phys.*, **18**, 1151–1155, 1985.

[Bur95] A. L. Burin, Dipole Gap Effects in Low Energy Excitation Spectrum of Amorphous Solids. Theory for Dielectric Relaxation, *J. Low Temp. Phys.*, **100**(3/4), 309–337, 1995.

[Bur06a] A. L. Burin, S. Hunklinger, C. Enss, and A. Fleischmann, Magnetic Field Dependence of the Low-Temperature Dielectric Constant in Glasses, *AIP Conf. Proc.*, **850**(1), 1573–1574, 2006.

[Bur06b] A. L. Burin, I. Y. Polishchuk, P. Fulde, and Y. Sereda, Effect of Nuclear Quadrupole Interactions on the Dynamics of Two-Level Systems in Glasses, *Phys. Rev. Lett.*, **96**, 025505, 2006.

[Bur06c] A. L. Burin, I. Y. Polishchuk, P. Fulde, and Y. Sereda, Low-temperature breakdown of coherent tunneling in amorphous solids induced by the nuclear quadrupole interaction, *Phys. Rev. B*, **73**(1), 14205, 2006.

[Bur13] A. L. Burin, J. M. Leveritt, G. Ruyters, C. Schötz, M. Bazrafshan, P. Fassl, M. von Schickfus, A. Fleischmann, and C. Enss, Low-temperature dipolar

echoes in amorphous dielectrics: Significance of relaxation and decoherence free two-level systems, *EPL (Europhys. Lett.)*, **104**(5), 57006, 2013.

[Bur14] J. Burnett, L. Faoro, I. Wisby, V. L. Gurtovoi, A. V. Chernykh, G. M. Mikhailov, V. A. Tulin, R. Shaikhaidarov, V. Antonov, P. J. Meeson, A. Y. Tzalenchuk, and T. Lindström, Evidence for interacting two-level systems from the 1/f noise of a superconducting resonator., *Nat. Commun.*, **5**(May), 4119, 2014.

[Cah88] D. G. Cahill and R. O. Pohl, Lattice vibrations and heat transport in crystals and glasses, *Annu. Rev. Phys. Chem.*, **39**(1), 93–121, 1988.

[Car94] H. M. Carruzzo, E. R. Grannan, and C. C. Yu, Nonequilibrium dielectric behavior in glasses at low temperatures: Evidence for interacting defects, *Phys. Rev. B*, **50**(10), 6685–6695, 1994.

[Cha79] C. Chappert, P. Beauvillain, J. P. Renard, and K. Knorr, Low Temperature ac Susceptibility of amorphous Holmium Aluminosilicate $(Al_2O_3)_{0.2}(Ho_2O_3)_{0.2}(SiO_2)_{0.6}$. Frequency dependence of the spin freezing temperature, *Solid State Commun.*, **31**, 213–218, 1979.

[Cha80] C. Chappert, P. Beauvillain, J. P. Renard, and K. Knorr, Low temperature magnetic properties of amorphous holmium aluminosilicate: A new insulating spin glass, *J. Magn. Magn. Mater.*, **15-18**, 117–118, 1980.

[Che76] J. D. N. Cheeke, H. Ettinger, and B. Hebral, Analysis of heat transfer between solids at low temperatures, *Can. J. Phys.*, **54**(17), 1749–1771, 1976.

[Che78] Chemical Rubber Company, CRC handbook of chemistry and physics, 1978.

[Cla94] J. Classen, C. Enss, C. Bechinger, G. Weiss, and S. Hunklinger, Low frequency acoustic and dielectric measurements on glasses, *Ann. Phys.*, **506**(5), 315–335, 1994.

[Cla00] J. Classen, T. Burkert, C. Enss, and S. Hunklinger, Anomalous frequency dependence of the internal friction of vitreous silica, *Phys. Rev. Lett.*, **84**(10), 2176–2179, 2000.

[Con06] S. D. Conzone and J. E. Shelby, Formation and properties of sodium tantalum silicate glasses, *Phys. Chem. Glas. - Eur. J. Glas. Sci. Technol. Part B*, **47**(3), 283–287, 2006.

[Cul99] E. Culea, T. Ristoiu, and I. Bratu, Structural and magnetic behavior of some borate glasses containing holmium ions, *Mater. Sci. Eng. B*, **57**, 259–261, 1999.

[Däh10] D. Dähn, Messung der dielektrischen Funktion des Tantal-Oxid-Glases N-KZFS11 bei sehr tiefen Temperaturen, Diploma thesis, Heidelberg University, 2010.

[Deb12] P. Debye, Zur Theorie der spezifischen Wärmen, *Ann. Phys.*, **344**, 789–839, 1912.

[Deb13] P. Debye, The theory of anomalous dispersion in the region of long-wave electromagnetic radiation, *Ber. Dtsch. Phys. Ges.*, **15**(16), 777–793, 1913.

[Dou80] P. Doussineau, C. Frénois, R. G. Leisure, A. Levelut, and J.-Y. Prieur, Amorphous-like acoustical properties of Na doped β-Al_2O_3, *J. Phys.*, **41**(10), 1193–1211, 1980.

[Dou87] P. Doussineau, A. Levelut, M. Matecki, J. P. Renard, and W. Schön, Acoustic and Magnetic Studies of an Insulating Spin Glass, *EPL (Europhys. Lett.)*, **3**(2), 251–258, 1987.

[Dou89] P. Doussineau, A. Levelut, M. Matecki, and W. Schön, Acoustic susceptibility of some insulating spin-glasses, *J. Phys.*, **50**(6), 659–674, 1989.

[Efr75] A. L. Efros and B. I. Shklovskii, Coulomb gap and low temperature conductivity of disordered systems, *J. Phys. C Solid State Phys.*, **8**(4), L49–L51, 1975.

[Eli12] M. Elisa, B. A. Sava, I. C. Vasiliu, E. M. Carstea, I. Feraru, C. Tanaselia, M. Senila, and B. Abraham, Optical and structural characterization of Eu^{3+}, Dy^{3+}, Ho^{3+} and Tm^{3+}-doped phosphate glasses, *Phys. Chem. Glas. - Eur. J. Glas. Sci. Technol. Part B*, **53**(5), 219–224, 2012.

[Ens89] C. Enss, C. Bechinger, and M. von Schickfus, Dynamics of Tunneling States in Borosilicate Glass, *Phonons 89, World Sci. Singapore*, 474–479, 1989.

[Ens91] C. Enss, Untersuchung der Dynamik von Tunnelzuständen in Gläsern und kristallinen Defektsystemen, PhD thesis, Heidelberg University, 1991.

[Ens97] C. Enss and S. Hunklinger, Incoherent Tunneling in Glasses at Very Low Temperatures, *Phys. Rev. Lett.*, **79**(15), 2831–2834, 1997.

[Ens05] C. Enss and S. Hunklinger, Low temperature physics, Springer, Heidelberg, 2005.

[Ere11] I. Y. Eremchev, Y. G. Vainer, A. V. Naumov, and L. Kador, Low-temperature dynamics in amorphous polymers and low-molecular-weight glasses — what is the difference?, *Phys. Chem. Chem. Phys.*, **13**, 1843–1848, 2011.

[Esq92] P. Esquinazi, R. König, and F. Pobell, Acoustic Properties of Amorphous SiO_2 and PdSiCu, and of Crystalline Ag, NbTi and Ta at Very Low Temperatures, *Z. Phys. B*, **87**(3), 305–321, 1992.

[Esq98] P. Esquinazi (Ed.), Tunneling systems in amorphous and crystalline solids, Springer, Heidelberg, 1998.

[Fic12] G. Fickenscher, Phasenkohärenz und Energierelaxation von Tunnelsystemen in Gläsern – Messung und Analyse von Polarisationsechos an BK7, PhD thesis, Heidelberg University, 2012.

[Fre16] B. Frey, To be published, Master's thesis, Heidelberg University, 2016.

[Fro77] G. Frossati, J. l. G. Gilchrist, J. C. Lasjaunias, and W. Meyer, Spectrum of low-energy dipolar states in hydrated vitreous silica, *J. Phys. C Solid State Phys.*, **10**(18), L515–L519, 1977.

[Gra12] G. J. Grabovskij, T. Peichl, J. Lisenfeld, G. Weiss, and A. V. Ustinov, Strain Tuning of Individual Atomic Tunneling Systems Detected by a Superconducting Qubit, *Science*, **338**(6104), 232–234, 2012.

[Hal12] A. Halfar, Entwicklung einer neuen kontaktfreien Messmethode zur Bestimmung der spezifischen Wärme von amorphen Festkörpern bei ultratiefen Temperaturen, PhD thesis, Heidelberg University, 2012.

[Ham10] H. Hamaed, E. Ye, K. Udachin, and R. W. Schurko, Solid-State ^{137}Ba NMR Spectroscopy: An Experimental and Theoretical Investigation of ^{137}Ba Electric Field Gradient Tensors and Their Relation to Structure and Symmetry, *J. Phys. Chem. B*, **114**(18), 6014–6022, 2010.

[Hau02] R. Haueisen and G. Weiss, Non-linearities and magnetic field dependencies of the dielectric constant of $BaO{\cdot}Al_2O_3{\cdot}SiO_2$, *Physica B*, **316-317**, 555–557, 2002.

[Hau15] N. Hauff, Dielektrische Permittivität von HY-1 Glas bei hohen Frequenzen und tiefen Temperaturen, Bachelor's thesis, Heidelberg University, 2015.

[Hem14] M. Hempel, Unpublished Data, 2014.

[Hem15] M. Hempel, Elastische Eigenschaften von supraleitenden massiven metallischen Gläsern, PhD thesis, Heidelberg University, 2015.

[Her10] Heraeus Quarzglas, Quarzglas für die Optik Daten und Eigenschaften, Heraeus Quarzglas GmbH & Co. KG, 2010.

[Hom15] G. Homann, Dielektrische Permittivität des Glases N-BK7 zwischen 8 mK und 300 K im MHz-Bereich, Bachelor's thesis, Heidelberg University, 2015.

[Hoy16a] Hoya Corporation, Data Sheet HY-1, 2016.

[Hoy16b] Hoya Corporation, Material Safety Data Sheet HY-1 Glass, 2016.

[Hun76] S. Hunklinger and W. Arnold, Ultrasonic Properties of Glasses at Low Temperatures, in W. P. Mason and R. N. Thurston (Ed.), *Phys. Acoust.*, Volume 12, Chapter 3, 155–216, Academ. Press, New York, 1976.

[Jäc72] J. Jäckle, On the Ultrasonic Attenuation in Glasses at Low Temperatures, *Z. Phys.*, **257**, 212–223, 1972.

[Kar83] V. G. Karpov, M. I. Klinger, and F. N. Ignat'ev, Theory of the low-temperature anomalies in the thermal properties of amorphous structures, *Sov. Phys. JETP*, **57**(2), 439–448, 1983.

[Ket99] S. Kettemann, P. Fulde, and P. Strehlow, Correlated Persistent Tunneling Currents in Glasses, *Phys. Rev. Lett.*, **83**(21), 4325–4328, 1999.

[Kin08] M. Kinzer, Untersuchung der dielektrischen Funktion von Gläsern bei sehr tiefen Temperaturen, Diploma thesis, Heidelberg University, 2008.

[Kir97] M. Kirkengen and Y. M. Galperin, Nonlinear acoustic and microwave absorption in glasses, *Phys. Rev. B*, **56**(21), 615–618, 1997.

[Koh05] S. Kohara and K. Suzuya, Intermediate-range order in vitreous SiO_2 and GeO_2, *J. Phys. Condens. Matter*, **17**(5), S77–S86, 2005.

[Lai84] B. D. Laikhtman, Theory of electromagnetic and ultrasonic nonlinear absorption in dielectric glasses, *Phys. Rev. B*, **29**(6), 3601–3606, 1984.

[Las75] J. C. Lasjaunias, A. Ravex, M. Vandorpe, and S. Hunklinger, The Density of Low Energy States in vitreous silica: Specific heat and thermal conductivity down to 25 mK, *Solid State Commun.*, **17**, 1045–1049, 1975.

[Las78] J. Lasjaunias, R. Maynard, and M. Vandorpe, Existence of a Gap in the Low Energy Density of States of Vitreous Silica, *J. Phys. Colloq.*, **39**(C6), 973–975, 1978.

[Leg13] A. J. Leggett and D. C. Vural, "Tunneling two-level systems" model of the low-temperature properties of glasses: are "smoking-gun" tests possible?, *J. Phys. Chem. B*, **117**(42), 12966–71, 2013.

[Ler84] F. Lerbet and G. Bellessa, Acoustic propagation at low temperature in an amorphous rare-earth alloy : single-ion activation process, *J. Phys. Lett.*, **45**(21), 1045–1052, 1984.

[Ler87] F. Lerbet and G. Bellessa, Acoustic study of low-energy activation processes in magnetic rare-earth glasses: amorphous holmium aluminosilicates, *J. Phys.*, **48**(12), 2111–2118, 1987.

[Lis15] J. Lisenfeld, G. J. Grabovskij, C. Müller, J. H. Cole, G. Weiss, and A. V. Ustinov, Observation of directly interacting coherent two-level systems in an amorphous material., *Nat. Commun.*, **6**, 6182, 2015.

[Luc11] A. Luck, Untersuchung dielektrischer Eigenschaften zweier Gläser bei sehr tiefen Temperaturen, Diploma thesis, Heidelberg University, 2011.

[Lud02] S. Ludwig, C. Enss, P. Strehlow, and S. Hunklinger, Direct Coupling of Magnetic Fields to Tunneling Systems in Glasses, *Phys. Rev. Lett.*, **88**(7), 75501, 2002.

[Lud03] S. Ludwig, P. Nagel, S. Hunklinger, and C. Enss, Magnetic Field Dependent Coherent Polarization Echoes in Glasses, *J. Low Temp. Phys.*, **131**(April), 89–111, 2003.

[Mae96] H. Maekawa, P. Florian, D. Massiot, H. Kiyono, and M. Nakamura, Effect of Alkali Metal Oxide on Disilicate Glasses ^{17}O NMR Parameters and Si–O–Si Angles of Alkali Metal Disilicate Glasses, *J. Phys. Chem.*, **100**, 5525–5532, 1996.

[Mal79] H. Maletta and W. Felsch, Insulating spin-glass system $Eu_xSr_{1-x}S$, *Phys. Rev. B*, **20**(3), 1245–1260, 1979.

[Mar03] R. A. Martin, P. S. Salmon, H. E. Fischer, and G. J. Cuello, Identification of the relative distribution of rare-earth ions in phosphate glasses., *Phys. Rev. Lett.*, **90**(18), 185501, 2003.

[Mei96] M. Meissner and P. Strehlow, Specific heat of vitreous silica at temperatures below 100 mK, *Czechoslov. J. Phys.*, **46**(4), 2233–2234, 1996.

[Nag01] S. Nagata, H. Sasaki, K. Suzuki, J. Kiuchi, and N. Wada, Specific heat anomaly of the holmium garnet $Ho_3Al_5O_{12}$ at low temperature, *J. Phys Chem. Sol*, **62**, 1123–1130, 2001.

[Nag04] P. Nagel, A. Fleischmann, S. Hunklinger, and C. Enss, Novel Isotope Effects Observed in Polarization Echo Experiments in Glasses, *Phys. Rev. Lett.*, **92**(24), 245511, 2004.

[Nal04] P. Nalbach, D. D. Osheroff, and S. Ludwig, Non–equilibrium dynamics of interacting tunneling states in glasses, *J. Low Temp. Phys.*, **137**(3-4), 395–452, 2004.

[Nat98] D. Natelson, D. Rosenberg, and D. D. Osheroff, Evidence for Growth of Collective Excitations in Glasses at Low Temperatures, *Phys. Rev. Lett.*, **80**(21), 4689–4692, 1998.

[Ovi98] J. Oviedo and J. Fernandez Sanz, Molecular-dynamics simulations of $(NaO_2)_x(SiO_2)_{1-x}$ glasses: Relation between distribution and diffusive behavior of Na atoms, *Phys. Rev. B*, **58**(14), 9047–9053, 1998.

[Par93] D. A. Parshin, Soft potential model and universal properties of glasses, *Phys. Scr.*, **1993**(T49A), 180, 1993.

[PC14] T. Pérez-Castañeda, C. Rodríguez-Tinoco, J. Rodríguez-Viejo, and M. A. Ramos, Suppression of tunneling two-level systems in ultrastable glasses of indomethacin., *Proc. Natl. Acad. Sci. USA*, **111**(31), 11275–80, 2014.

[Pei83] R. Peichl, A. Weidinger, and E. Recknagel, PAC study of O–H and O–D in Ta, *Hyperfine Interact.*, **16**, 463–466, 1983.

[Pen95] F. Penning, M. Maior, P. Strehlow, S. Wiegers, H. van Kempen, and J. Maan, Magnetic field independent capacitance thermometers at very low temperatures, *Physica B*, **211**(1-4), 363–365, 1995.

[Phi72] W. A. Phillips, Tunneling states in amorphous solids, *J. Low Temp. Phys.*, **7**(3-4), 351–360, 1972.

[Phi87] W. A. Phillips, Two-level states in glasses, *Rep. Prog. Phys.*, **50**, 1657–1708, 1987.

[Pic74] L. Piché, R. Maynard, S. Hunklinger, and J. Jäckle, Anomalous Sound Velocity in Vitreous Silica at Very Low Temperatures, *Phys. Rev. Lett.*, **32**(25), 1426–1429, 1974.

[Pis05] W. A. Pisarski, T. Goryczka, B. Wodecka-Dus, M. Plonska, and J. Pisarska, Structure and properties of rare earth-doped lead borate glasses, *Mater. Sci. Eng. B Solid-State Mater. Adv. Technol.*, **122**(2), 94–99, 2005.

[Pob07] F. Pobell, Matter and methods at low temperatures, Springer, Berlin Heidelberg, 2007.

[Pol05] I. Y. Polishchuk, P. Fulde, A. L. Burin, Y. Sereda, and D. Balamurugan, Effect of Nuclear Quadrupole Interaction on the Relaxation in Amorphous Solids, *J. Low Temp. Phys.*, **140**(5-6), 355–376, 2005.

[Pol09] L. V. Polukinha, Influence of magnetic field on dielectric susceptibility of amorphous soldids at ultra low temperature, PhD thesis, Stanford University, 2009.

[Pra06] S. Prasad, T. M. Clark, T. H. Sefzik, H. T. Kwak, Z. Gan, and P. J. Grandinetti, Solid-state multinuclear magnetic resonance investigation of Pyrex®, *J. Non. Cryst. Solids*, **352**(26-27), 2834–2840, 2006.

[Rau95] S. Rau, C. Enss, S. Hunklinger, P. Neu, A. Würger, and S. Hunklinger, Acoustic properties of oxide glasses at low temperatures, *Phys. Rev. B*, **52**(10), 7179–7194, 1995.

[Rog97a] S. Rogge, D. Natelson, and D. D. Osheroff, Nonequilibrium and hysteretic low temperature dielectric response to strain in glasses, *J. Low Temp. Phys.*, **106**(5-6), 717–725, 1997.

[Rog97b] S. Rogge, D. Natelson, B. Tigner, and D. D. Osheroff, Nonlinear dielectric response of glasses at low temperature, *Phys. Rev. B*, **55**(17), 11256–11262, 1997.

[Sar16] B. Sarabi, A. N. Ramanayaka, A. L. Burin, F. C. Wellstood, and K. D. Osborn, Projected Dipole Moments of Individual Two-Level Defects Extracted Using Circuit Quantum Electrodynamics, *Phys. Rev. Lett.*, **116**(16), 1–5, 2016.

[Sch92] W. Schnauss, F. Fujara, and H. Sillescu, The molecular dynamics around the glass transition and in the glassy state of molecular organic systems: A ^{2}H–nuclear magnetic resonance (NMR) study, *J. Chem. Phys.*, **97**(2), 1378–1389, 1992.

[Sch07] Schott AG, Data Sheet N-BK7, 2007.

[Sch14] Schott AG, Data Sheet N-KZFS11, 2014.

[Sch15] Schott AG, N-KZFS11 Technical Safety Information, 2015.

[Sch16] C. W. Scholz, Untersuchung der dielektrischen Eigenschaften von N-KZFS11 zwischen 300 K und 10 mK bei 25 MHz, Bachelor's thesis, Heidelberg University, 2016.

[Ser07] Y. Sereda, I. Y. Polishchuk, and A. L. Burin, Resonant susceptibility of dielectric glasses in magnetic field, *Phys. Rev. B*, **75**(2), 24207, 2007.

[Sha76] R. D. Shannon, Revised effective ionic radii and systematic studies of interatomic distances in halides and chalcogenides, *Acta Crystallogr. Sect. A*, **32**(5), 751–767, 1976.

[Smi71] J. A. S. Smith, Nuclear quadrupole resonance spectroscopy. General principles, *J. Chem. Educ.*, **48**(1), 39–48, 1971.

[Ste76] R. B. Stephens, Intrinsic low-temperature thermal properties of glasses, *Phys. Rev. B*, **13**(2), 852–865, 1976.

[Sto95] J. T. Stockburger, M. Grifoni, and M. Sassetti, Nonlinear acoustic response of glasses in the tunneling model, *Phys. Rev. B*, **51**(5), 2835–2843, 1995.

[Sto05] N. Stone, Table of nuclear magnetic dipole and electric quadrupole moments, *At. Data Nucl. Data Tables*, **90**(1), 75–176, 2005.

[Str94] P. Strehlow and W. Dreyer, Heat Propagation in Glasses, *Physica B*, **194-196**, 485–486, 1994.

[Str98] P. Strehlow, C. Enss, and S. Hunklinger, Evidence for a Phase Transition in Glasses at Very Low Temperature: A Macroscopic Quantum State of Tunneling Systems?, *Phys. Rev. Lett.*, **80**(24), 5361–5364, 1998.

[Str00] P. Strehlow, M. Wohlfahrt, A. G. M. Jansen, R. Haueisen, G. Weiss, C. Enss, and S. Hunklinger, Magnetic Field Dependent Tunneling in Glasses, *Phys. Rev. Lett.*, **84**(9), 1938–1941, 2000.

[Sui06] B. H. Suits, Nuclear Quadrupole Resonance Spectroscopy, in D. R. Vij (Ed.), *Handb. Appl. Solid State Spectrosc.*, Chapter 2, 65–96, Springer US, 1st edition, 2006.

[Sun40] K.-H. Sun and A. Silverman, Tantalum Glass: K_2O-Ta_2O_5-SiO_2 Series, *J. Am. Ceram. Soc.*, **24**(5), 160–167, 1940.

[Swa89] E. T. Swartz and R. O. Pohl, Thermal boundary resistance, *Rev. Mod. Phys.*, **61**(3), 605–668, 1989.

[Sze75] J. Szeftel and H. Alloul, Nuclear Spin-Lattice Relaxation Associated with Low-Energy Excitations in Glasses, *Phys. Rev. Lett.*, **34**(11), 657–660, 1975.

[Tal02] C. Talon, M. A. Ramos, and S. Vieira, Low-temperature specific heat of amorphous, orientational glass, and crystal phases of ethanol, *Phys. Rev. B*, **66**, 012201, 2002.

[Tie92] D. Tielbürger, R. Merz, R. Ehrenfels, and S. Hunklinger, Thermally activated relaxation processes in vitreous silica: An investigation by Brillouin scattering at high pressures, *Phys. Rev. B*, **45**(6), 2750–2760, 1992.

[Tsu16] S. Tsurkan, To be published, Master's thesis, Heidelberg University, 2016.

[Ver94] D. E. Vernacotola, Alkali Niobium and Tantalum Silicate Glasses and Ferroelectric Glass-Ceramics, *Key Eng. Mater.*, **94-95**, 379, 1994.

[Vog92] W. Vogel, Glaschemie, Springer-Verlag Berlin Heidelberg, 3rd edition, 1992.

[vR98] R. van Rooijen, A. Marchenkov, H. Akimoto, R. Jochemsen, and G. Frossati, Dielectric Properties of Vitreous Silica with Various Hydroxyl Concentrations, *J. Low Temp. Phys.*, **110**(1), 269–274, 1998.

[vS76] M. von Schickfus and S. Hunklinger, The dielectric coupling of low-energy excitations in vitreous silica to electromagnetic waves, *J. Phys. C Solid State Phys.*, **9**, 439– 442, 1976.

[Wei85] V. Weidner, R. Mavrodineanu, K. D. Mielenz, R. A. Velapoldi, K. L. Eckerle, and B. Adams, Spectral Transmittance Characteristics of Holmium Oxide in Perchloric Acid Solution, *J. Res. Natl. Bur. Stand. (1934).*, **90**(2), 115–125, 1985.

[Wei95] R. Weis, Messung der dielektrischen Eigenschaften wechselwirkender Tunnelsysteme bei tiefen Temperaturen am Beispiel von KCl:Li, PhD thesis, Heidelberg University, 1995.

[Wes15] P. Wesp, Dielektrische Permittivität von N-KZFS11 Glas bei hoher Frequenz und tiefen Temperaturen, Bachelor's thesis, Heidelberg University, 2015.

[Wie87] S. A. J. Wiegers, R. Jochemsen, C. C. Kranenburg, and G. Frossati, Comparison of some glass thermometers at low temperatures in a high magnetic field, *Rev. Sci. Instrum.*, **58**(12), 2274, 1987.

[Woh01a] M. Wohlfahrt, Untersuchung der dielektrischen Tieftemperaturanomalien von Mehrkomponentengläsern in Magnetfeldern, PhD thesis, Heidelberg University, 2001.

[Woh01b] M. Wohlfahrt, P. Strehlow, C. Enss, and S. Hunklinger, Magnetic-field effects in non-magnetic glasses, *EPL (Europhys. Lett.)*, **56**(5), 690–694, 2001.

[Wol14] M. Wolter, Two-pulse dielectric polarisation echo experiments on the multicomponent glasses BK7 and HY-1, Master's thesis, Heidelberg University, 2014.

[Wür95] A. Würger, Collective low-energy excitations of two-level tunneling defects in mixed crystals, *Z. Phys. B*, **98**, 561–573, 1995.

[Wür97] A. Würger, From Coherent Tunneling to Relaxation – Dissipative Quantum Dynamics of Interacting Defect, Springer-Verlag Berlin Heidelberg, 1st edition, 1997.

[Wür02] A. Würger, A. Fleischmann, and C. Enss, Dephasing of Atomic Tunneling by Nuclear Quadrupoles, *Phys. Rev. Lett.*, **89**(23), 237601, 2002.

[Xue93] X. Xue and J. F. Stebbins, ^{23}Na NMR chemical shifts and local Na coordination environments in silicate crystals, melts and glasses, *Phys. Chem. Miner.*, **20**(5), 297–307, 1993.

[Zac32] W. H. Zachariasen, The Atomic Arrangement in Glass, *J. Am. Chem. Soc.*, **54**(10), 3841–3851, 1932.

[Zei15] A. Zeißner, Dielektrische Messungen im MHz-Bereich an HY-1 und Herasil zwischen 7 mK und 10 K, State examination thesis, Heidelberg University, 2015.

[Zel71] R. C. Zeller and R. O. Pohl, Thermal Conductivity and Specific Heat of Noncrystalline Solids, *Phys. Rev. B*, **4**(6), 2029–2041, 1971.

Acknowledgments

Ohne die Unterstützung durch die unterschiedlichsten Personen wäre weder diese Dissertation entstanden, noch hätten die letzten fünf Jahre so unglaublich viel Spaß gemacht. Ich danke deshalb hiermit von Herzen

Prof. Christian Enss für sein unermüdliches Interesse an dieser Arbeit, für die großen Freiheit beim Ausprobieren neuer Messungen, für die vielen Diskussionen bis zur letzten Minute, und das große Vertrauen in die Quadrupole,

Prof. Heinz Horner für das große Interesse an dieser Arbeit und das Übernehmen des Zweitgutachtens,

Andreas Reiser, dessen unglaublich ansteckende Begeisterung für Physik im Allgemeinen und neue Aufbauten für dielektrische Tieftemperaturmessungen und NQR im Besonderen die Arbeit vor allem in den letzten beiden Jahren sehr geprägt und ein gemeinsames Betreuen der vielen Bachelorarbeiten zum Vergnügen gemacht hat,

Andreas Fleischmann für seine immer neuen Ideen, wenn Messungen oder deren Interpretation wieder einmal aussichtslos erschienen und für die wunderbar anschauliche Darstellung von Tunnelsystemen,

Loredana Gastaldo für die Aufmunterungen zur rechten Zeit und die geteilte Liebe für Holmium und natürlich
Philipp und Lorenz, die sich nicht von Banalitäten wie Physik und zu schreibenden Doktorarbeiten vom Einfordern von Zeit und Spaß abhalten lassen,

Sebastian Kempf, der die Herstellung der neuen Proben immer spontan in den Reinraumplan eingebaut hat,

der HGSFP, deren großzügige Unterstützung mir den Besuch zweier Konferenzen in Argentinien und Israel, sowie den Besuch einer Winterschool ermöglicht hat,

Siegfried Hunklinger und Gernot Kasper für die historisch kritische Einordnung von alten und neuen Messungen,

Rudi Eitel, nicht nur für das unermüdliche Verflüssigen von Helium, sondern auch das verdreifachen meines Wissens über Motoren und große Maschinen aller Art,

Herrn Wolf für die schnelle Herstellung einer weiteren mikrostrukturierten Probe und der Metallisierung weiterer geschlagener zwölf Proben für die neuen Aufbauten, Herrn Stadler für das Ultraschallschneiden der Proben und die Nachhilfe im Glasschmelzen, Herrn Azeroth für die Hilfe bei sämtlichen Problemen mit der Messelektronik, der mechanischen Werkstatt für die Herstellung der neuen Aufbauten und der EDV, allen voran Herrn Kattinger für schnelle Hilfe bei Problemen mit AFS etc.,

meinen Bürokollegen Andreas Reifenberger und Marius Hempel für das Betreuen der Messungen im Nachbarlabor, Anregungen zu neuen Auswertungen und Darstellungen von Messergebnissen, die Mithilfe bei LabVIEW und den Genplot Befehl des Tages, außerdem dafür, dass sie mein aktives und passives Sarkasmuslevel über die Jahre unglaublich gesteigert haben,

„meinen“ BachelorInnen Nils, Philipp, Guido, Dominic, Edin, Marcus, Marcel H., Lennart, Mathias und Wiebke und MasterInnen Max, Andreas, Sergey, Anna, Benedikt und Marcel S. sowie der Staatsexamenskandidatin Anne, deren Daten direkt oder indirekt in diese Arbeit eingeflossen sind und deren kritische Nachfragen sehr zu meinem eigenen Verständnis beigetragen haben,

den weiteren aktuellen und ehemaligen F3lern für die unkomplizierte Arbeitsteilung und die gute Stimmung im Labor,

den F4lern, allen voran Daniel Hengstler, für wunderbare Kaffeerunden, Konferenzbesuche und Spätschichten auf dem Laborflur,

meinen Freundinnen, den PhysikerInnen, VilligsterInnen und Medis, für Ablenkungen von und ihr Interesse an der Arbeit, für ihr Offenes Ohr und das Ertragen einer Physikerin beim Zusammenschreiben,

Kai, für einfach Alles! Hier aber insbesondere Danke für die ungezählten Runden im Botanischen Garten, für das Mitempfinden aller Hochs und Tiefs auf der Achterbahn einer experimentellen Doktorarbeit, für seinen steten Ansporn, die Schulter zum Anlehnen und die grenzenlose Unterstützung, nicht zuletzt bei abstürzenden Servern eine Stunde vor Ende der Arbeit.

Und schließlich gilt mein Dank meiner wunderbaren Familie, vor allem natürlich meinen beiden Brüdern und meinen Eltern, für ihre große Unterstützung während der gesamten Doktorarbeitszeit, ihre immerwährende Anteilnahme auch aus der Ferne und für ihr unerschütterliches Vertrauen in mich.